



HAL
open science

Advanced neutronics-thermohydraulics studies for MSRs (Molten Salt Reactors)

François Martin

► **To cite this version:**

François Martin. Advanced neutronics-thermohydraulics studies for MSRs (Molten Salt Reactors). Nuclear Experiment [nucl-ex]. Université Grenoble Alpes [2020-..], 2024. English. NNT : 2024GRALI004 . tel-04559033

HAL Id: tel-04559033

<https://theses.hal.science/tel-04559033>

Submitted on 25 Apr 2024

HAL is a multi-disciplinary open access archive for the deposit and dissemination of scientific research documents, whether they are published or not. The documents may come from teaching and research institutions in France or abroad, or from public or private research centers.

L'archive ouverte pluridisciplinaire **HAL**, est destinée au dépôt et à la diffusion de documents scientifiques de niveau recherche, publiés ou non, émanant des établissements d'enseignement et de recherche français ou étrangers, des laboratoires publics ou privés.

THÈSE

Pour obtenir le grade de

DOCTEUR DE L'UNIVERSITÉ GRENOBLE ALPES

École doctorale : I-MEP2 - Ingénierie - Matériaux, Mécanique, Environnement, Energétique, Procédés, Production

Spécialité : MEP - Mécanique des fluides Energétique, Procédés

Unité de recherche : Laboratoire de Physique Subatomique et Cosmologie

Modélisation avancée neutronique-thermohydraulique pour les MSR (Réacteurs à Sels Fondus) de type RNR à combustible liquide

Advanced neutronics-thermohydraulics studies for MSRs (Molten Salt Reactors)

Présentée par :

François MARTIN

Direction de thèse :

Elsa MERLE

PROFESSEURE DES UNIVERSITES, Université Grenoble Alpes

Directrice de thèse

Guillaume CAMPIONI

Co-encadrant de thèse

Yannick GORSSE

INGENIEUR CHERCHEUR, CEA Saclay

Co-encadrant de thèse

André BERGERON

INGENIEUR CHERCHEUR, CEA

Co-encadrant de thèse

Rapporteurs :

Jean C. RAGUSA

FULL PROFESSOR, Texas A&M University

Adrien TOUTANT

MAITRE DE CONFERENCES HDR, Université de Perpignan

Thèse soutenue publiquement le **11 janvier 2024**, devant le jury composé de :

Elsa MERLE

PROFESSEURE DES UNIVERSITES, Grenoble INP

Directrice de thèse

Jean C. RAGUSA

FULL PROFESSOR, Texas A&M University

Rapporteur

Adrien TOUTANT

MAITRE DE CONFERENCES HDR, Université de Perpignan

Rapporteur

Frédéric BERTRAND

DIRECTEUR DE RECHERCHE, CEA centre de Cadarache

Examineur

Axel LAUREAU

CHARGE DE RECHERCHE, CNRS délégation Bretagne et Pays de la Loire

Examineur

Yves DELANNOY

PROFESSEUR DES UNIVERSITES, Grenoble INP

Président

Iztok TISELJ

CHARGE DE RECHERCHE, Joef Stefan Institute

Examineur

Invités :

André BERGERON

CHARGE DE RECHERCHE, CEA Saclay

Yannick GORSSE

CHARGE DE RECHERCHE, CEA Saclay



Coupled Neutronics – Thermal-hydraulics Modelling of Molten Salt Reactors for Turbulent Fluctuations Analysis

PhD thesis

François MARTIN

Université Paris-Saclay, CEA, Service d'Études des Réacteurs et de Mathématiques
Appliquées, 91191, Gif-sur-Yvette, France

2023

Contents

List of Figures	6
List of Tables	6
Acknowledgements – Remerciements	13
Introduction	17
I Reminders on nuclear reactor physics	22
I.1 Neutronics	23
I.1.a The fission process and the chain reaction	23
I.1.b Cross sections and neutronic feedbacks	25
I.1.c Fast and thermal neutrons	27
I.1.d Delayed neutrons and effective delayed neutron fraction	28
I.1.e The Boltzmann equation	29
I.1.f The steady-state Boltzmann equation	32
I.1.g The adjoint problem and adjoint flux	33
I.2 Thermal-hydraulics	33
I.2.a Eulerian specification and Navier-Stokes equations	33
I.2.b The pressure equation	34
I.2.c Turbulent flows	35
I.2.d Turbulent transport of energy and concentration	37

I.2.e	Buoyancy: the Boussinesq approximation	38
I.2.f	Wall flows	39
I.3	Molten salt reactors physics	41
I.3.a	The coupled neutronic–thermal-hydraulic problem	41
I.3.b	Transport of the delayed neutrons precursors	42
I.3.c	Wall laws for MSRs	43
II	Numerical resolution of the coupled problem	44
II.1	Numerical resolution of the Boltzmann equation	45
II.1.a	Discretisation of the steady-state Boltzmann equation	45
II.1.b	Lattice calculation and self-shielding	46
II.1.c	Core calculation	48
II.1.d	Discretisation of the time-dependant Boltzmann equation	49
II.1.e	Critical calculation for transient simulations	49
II.2	Numerical resolution of the Navier-Stokes equations	50
II.2.a	Time discretisation of the Navier-Stokes equations	50
II.2.b	Laminar flows	51
II.2.c	Direct Numerical Simulation (DNS)	51
II.2.d	Reynolds-Averaged Navier-Stokes (RANS) approach	52
II.2.e	Large Eddy Simulation (LES) approach	54
II.2.f	Flow near the wall	57
II.3	Multiphysics codes for MSRs simulations	57
II.3.a	The need for specific codes	57
II.3.b	Existing multiphysics codes adapted for MSRs	58
II.4	The APOLL03 [®] – TrioCFD multiphysics code	59
II.4.a	Presentation	59

II.4.b	Field exchanges	61
II.4.c	Steady-state calculation strategy	61
II.4.d	Transient calculation strategy	61
II.4.e	V&V roadmap of the APOLL03 [®] – TrioCFD code	62
III	Validation of the APOLL03[®] – TrioCFD code on a historical MSR: the Aircraft Reactor Experiment	64
III.1	The Aircraft Reactor Experiment	65
III.2	Thermal-hydraulic model of the ARE	68
III.2.a	Geometries and meshing	68
III.2.b	Resolved equations	69
III.2.c	Physical properties	70
III.2.d	Boundary conditions	72
III.2.e	Source terms	72
III.3	Neutronic model of the ARE	72
III.3.a	Lattice calculation	72
III.3.b	Determining the materials' compositions	74
III.3.c	Core calculation	75
III.4	Steady-state simulation: the ARE nominal state	77
III.5	Variation of β_{eff} with the fuel flow rate	79
III.6	Transient simulation: insertion of a dollar of reactivity	81
III.6.a	The actual experiment	81
III.6.b	First test run: instantaneous reactivity insertion	81
III.6.c	Progressive reactivity insertion by diluting the rod	83
III.6.d	Progressive reactivity insertion with a varying inlet temperature	86
III.7	Transient simulation: variation of extracted power	87

III.7.a	The actual experiment	87
III.7.b	The simulated experiment	89
IV	Modelling of turbulent fluctuations in the Molten Salt Fast Reactor	91
IV.1	The Molten Salt Fast Reactor	93
IV.1.a	Fuel cycle and salt composition	94
IV.1.b	Core geometry and materials	94
IV.1.c	Bubble injection	94
IV.1.d	Pumps and heat exchangers	95
IV.1.e	Free volume and draining tanks	95
IV.2	Thermal-hydraulic model of the MSFR	95
IV.2.a	Resolved equations	95
IV.2.b	Physical properties	96
IV.2.c	Geometries and meshing	96
IV.2.d	Turbulence models	99
IV.2.e	Boundary conditions	99
IV.2.f	Source terms	100
IV.3	RANS simulations on the MSFR	101
IV.3.a	Impact of the geometry	101
IV.3.b	Impact of the heat exchanger modelling	105
IV.3.c	Mesh convergence on the open sector geometry	106
IV.3.d	Impact of the spatial scheme	106
IV.3.e	Impact of the RANS model	107
IV.4	Numerical benchmark on the open sector	108
IV.5	LES simulations on the MSFR	111
IV.5.a	Impact of the geometry	112

IV.5.b	Comparison with RANS simulations	115
IV.5.c	Turbulent fluctuations in the MSFR core	115
IV.6	Neutronic model of the MSFR	120
IV.6.a	Lattice calculation	120
IV.6.b	Core calculation	121
IV.6.c	Neutronic simulation: power distribution	121
IV.7	Coupled simulations on the MSFR	122
IV.7.a	Delayed neutrons precursors modelling	122
IV.7.b	Coupled steady-state of the MSFR	124
IV.7.c	Coupled transient simulations on the MSFR	125
Conclusion		128
Appendices		
A	Nomenclature	132
B	Development of a toy model for turbulent fluctuations analysis	139
B.1	Thermal-hydraulic model	139
B.2	Neutronic model	146
B.3	Coupled calculations	147
References		149
Summary - Résumé des travaux		157

List of Figures

1	Global electricity mix in 2019 (data from IEA [1]).	18
I.1	Schematic view of the neutron-induced fission of ^{235}U	24
I.2	Microscopic cross sections of the neutron-induced fission (blue) and the radiative capture (green) for a "fissile" nucleus (^{235}U , top), and a "non-fissile" nucleus (^{238}U , bottom). Data from JEFF-3.3 [36], visualisation from IAEA Nuclear Data Services [37].	26
I.3	Doppler broadening of the ^{238}U neutron capture resonance at 6.67 eV [38].	27
I.4	Typical delayed and prompt neutrons spectrum for ^{235}U and ^{239}Pu [39].	29
I.5	Schematic view of the turbulent energy cascade.	36
I.6	A typical turbulent energy spectrum.	37
I.7	The wall law (straight, dot-dashed line) plotted against DNS data (curved lines) at two different Reynolds numbers, taken from Pope [26].	40
I.8	The log law (line) plotted against different developed turbulent channel flow measures, taken from Pope [26].	41
II.1	Absorption cross section and neutron spectrum at the 6.67eV resonance of ^{235}U	48
II.2	The APOLL03 [®] – TrioCFD coupling strategy.	60
II.3	Transient calculation numerical scheme.	62
III.1	Schematic diagram of the ARE [4].	66

III.2	Elevation section of the ARE core [4].	67
III.3	Plan section of the ARE core [4].	68
III.4	Elevation section and top view of the ARE meshing in TrioCFD.	69
III.5	Geometry used for the lattice calculation.	73
III.6	Estimated concentrations for different impurities in the inconel and BeO [4].	74
III.7	Equatorial section of the homogenised geometry used for core calculations.	76
III.8	Elevation and equatorial sections of the non-homogenised geometry used for core calculations.	76
III.9	Variations of reactivity with fuel flow rate: experimental values (blue circles) and simulated values(yellow triangles).	80
III.10	Experiment H-8, reactivity insertion: time is read from right to left (in minutes). The first half of the experiment (in the red square) is described and reproduced.	82
III.11	Transient simulation H8: instantaneous reactivity insertion of +400 pcm.	84
III.12	Transient simulation H8: progressive dilution of the regulating rod. The experimental data were digitalized using WebPlotDigitizer [83].	85
III.13	Transient simulation H8: progressive dilution of the regulating rod with a varying inlet temperature. The experimental data were digitalized using WebPlotDigitizer [83].	87
III.14	Experiment H-14, extracted power increase: time is read from right to left (in minutes). The first part of the experiment (in the red square) is described and reproduced.	88
III.15	Simulated experiment H-14: inlet fuel temperature ramp. The experimental data were digitalized using WebPlotDigitizer [83] and corrected for the time lags.	90

IV.1	Schematic layout of the MSFR.	93
IV.2	CAD of the MSFR for the thermalhydraulics modelling.	97
IV.3	Meshes used for the RANS (left) and the LES (right) simulations.	97
IV.4	Parameters for the fine mesh quality assessment.	98
IV.5	Power field used for pure thermal-hydraulic calculations.	100
IV.6	RANS steady-state fields of the MSFR (full core).	102
IV.7	RANS steady-state fields of the MSFR (one sector). The equatorial line used for plots is shown in red.	103
IV.8	Compared equatorial plots of the full core (solid green line) against one sector (dashed blue line) for the RANS model.	104
IV.9	Velocity field for the "open" sector geometry.	105
IV.10	Velocity equatorial plots for the "standard" sector geometry (dashed blue line) and the "open" sector geometry (solid red line) with a coarse 25 mm mesh.	106
IV.11	Mesh convergence study for the open sector geometry: 25 mm mesh (dotted red line), 10 mm mesh (dashed black line), and 7 mm mesh (solid orange line).	107
IV.12	Velocity equatorial plots for a second-order scheme for the convection operator (solid black line) and a first-order one (dashed purple line).	108
IV.13	Velocity equatorial plots for the standard $k - \epsilon$ model (solid black line) and the realisable $k - \epsilon$ model (dashed brown line).	109
IV.14	Velocity equatorial plots for the different codes (each using its own mesh) on the MSFR benchmark, for a classical $k - \epsilon$ model.	110
IV.15	Velocity equatorial plots for the different codes (each using its own mesh) on the MSFR benchmark, for a realisable $k - \epsilon$ model.	111
IV.16	LES mean and instantaneous fields of the MSFR (full core).	112

IV.17	LES mean and instantaneous fields of the MSFR (one sector).	113
IV.18	Compared equatorial plots between the full core geometry (dashed blue line) and the sector geometry (solid green line).	114
IV.19	Compared equatorial plots between the LES calculation (dashed blue line) and the RANS calculation (solid green line).	116
IV.20	Spatial fluctuations in the MSFR: equatorial plots of the LES instantaneous fields (full core simulation).	117
IV.21	Time fluctuations in the MSFR: temperature evolution in the center of the core; times before 2 s are removed because the flow is not developed.	118
IV.22	Temperature spectrum in the center of the core of the MSFR.	118
IV.23	Time fluctuations in the MSFR: temperature evolution in the center of the core (high frequencies filtered out).	119
IV.24	Mesh used for the MSFR lattice calculation.	120
IV.25	Mesh used for the MSFR core calculation (500 000 tetrahedras).	121
IV.26	Power density field for a uniform 700 °C temperature.	122
IV.27	Compared equatorial (top) and vertical (bottom) plots of the power density between the neutronic pre-calculation and the correlation used for thermal-hydraulic calculation.	123
IV.28	Compared equatorial (top) and vertical (bottom) plots of the power distribution between the neutronic pre-calculation (dotted blue line) and the coupled calculation (solid green line).	125
IV.29	Compared equatorial plots of the temperature field, on the thermal-hydraulic mesh (dotted blue line) and the neutronic mesh (solid green mesh).	126
B.1	Elevation section of the thermal-hydraulic mesh used for the toy model (3 millions tetrahedra).	140

B.2	Thermal-hydraulic mesh assessment parameters for the toy model. . . .	141
B.3	Boundary conditions for the toy model.	142
B.4	LES pre-calculation of the toy model: elevation sections of the mean and instantaneous fields.	143
B.5	Spatial fluctuations in the toy model: equatorial plots of the instantaneous fields.	144
B.6	Time fluctuations in the toy model: temperature evolution in the center of the core.	145
B.7	Time fluctuations in the toy model: temperature evolution near the wall.	145
B.8	Neutronic mesh used for the toy model.	146
B.9	Initial power density field of the toy model.	147
B.10	Compared equatorial (top) and vertical (bottom) plots of the power distribution between the neutronic pre-calculation (blues dashed lines) and the coupled calculation (solid green lines).	148

List of Tables

III.1	Properties of the different materials in the ARE thermal-hydraulic model, at the reference temperature of 1100 K for the salt, and 950 K for the sodium and the solid.	71
III.2	BeO density, impurities concentrations, and rods values in the ARE and two different MPOs.	75
III.3	Compared values for nominal operating conditions.	78
IV.1	Properties of the MSFR salt used in the simulations.	96
IV.2	RANS numerical scheme.	99
IV.3	LES numerical scheme.	99
A.1	Neutronics nomenclature.	132
A.2	Thermal-hydraulics nomenclature.	134
A.3	Abbreviations used.	137

Acknowledgements – Remerciements

Ce travail de thèse a été l’occasion d’échanger, interagir, et sympathiser avec de nombreuses personnes, que je souhaiterais remercier ici. Il est malheureusement couru d’avance que j’oublie certaines personnes, pardon d’avance !

Tout d’abord, je remercie grandement les membres de mon jury, d’avoir pris le temps de lire ce manuscrit et d’assister à la soutenance. Merci donc à Yves Delannoy, Frédéric Bertrand, Axel Laureau, et Iztok Tiselj pour leurs questions, remarques et suggestions, qui ont contribué à améliorer et enrichir ce manuscrit. Je remercie particulièrement mes deux rapporteurs, Jean Ragusa et Adrien Toutant, pour leurs rapports et commentaires qui ont également contribué à améliorer ce mémoire de doctorat.

Je redouble mes remerciements à Frédéric Bertrand et Axel Laureau, membres du Comité de Suivi Individuel, qui ont suivi pendant trois ans l’avancement de cette thèse et m’ont prodigué de nombreux conseils, que ce soit lors des réunions du CSI ou lors de nos rencontres en conférences. J’en profite pour tripler mes remerciements à Axel Laureau, qui a suivi avec un intérêt tout particulier mon travail pendant trois ans, et m’a à plusieurs reprises dispensé des conseils et explications plus que bienvenus, soit directement, soit par l’intermédiaire de ma directrice de thèse.

Je remercie évidemment toute mon équipe encadrante, et en premier lieu ma directrice de thèse Elsa Merle : je ne saurais imaginer une meilleure combinaison d’expertise, aussi bien technique qu’administrative, de bienveillance, de pédagogie et de bonne humeur, pour encadrer une thèse. Un très grand merci également à Nathan Greiner, pour ta connaissance profonde (et forte utile !) de la neutronique des MSR, ta rigueur, parfois intransigeante mais nécessaire et salutaire, ainsi que ta patience infinie pour lire des sources et déboguer des seg faults. Merci ! Côté thermohydraulique, un grand merci à André Bergeron, pour ton intérêt évident pour les problématiques de turbulences dans les MSR, et ton suivi très attentif de tous les travaux entrepris lors de ces trois ans. Un très grand merci également à Yannick Gorsse, pour tes connaissances et conseils en thermo-hydraulique, en TRUST, et en multiphysique, qui se révélèrent bien plus d’une fois essentiels au bon fonctionnement des codes et au bon déroulé de la thèse. Je tiens également à remercier chaleureusement Guillaume Campioni, certes parti en cours de thèse (mais pour une bonne cause !), mais qui m’a permis de travailler sur ce sujet passionnant des MSR dès 2018, et sans qui ni cette thèse, ni la plupart des études menées sur les MSR au CEA n’auraient vu le jour; Guillaume, je te souhaite le

meilleur dans tes nouvelles aventures startup-esques !

Je remercie également toutes les personnes, au CEA ou ailleurs, qui m'ont apporté une aide scientifique lors de mes travaux (en craignant évidemment d'en oublier) : François Madiot pour tous les développements réalisés dans Apollo pour les MSRs ; Karim Ammar pour l'aide au déchiffrement des jeux de données coeur et réseau ; Ulrich Bieder pour son expertise inégalée en écoulements monophasiques turbulents ; Elie Saikali pour ses conseils TRUST et multiphysiques ; Christophe Bourcier pour ses conseils sur les géométries et maillages SALOME ; Antoine Gerschenfeld pour ses nombreux conseils TRUST, notamment sur l'orientation correcte des polyèdres.

Je remercie grandement Loïc De Carlan, chef du Service d'Etudes des Réacteurs et de Mathématiques Appliquées, qui m'a accueilli pendant ces trois ans, ainsi que Céline Guénaut et Amélie Rouchon, cheffes successives du Laboratoire de Physique et d'Etude des Coeurs. Je les remercie également de m'avoir permis de rester travailler dans ce service et ce laboratoire, certes sur d'autres sujets, mais dans une ambiance toute aussi agréable. Je remercie également Carole Mariaud et Brigitte Mariani pour leur aide administrative sans pareils.

Un grand merci à tous les thésards et thésardes dont j'ai croisé la route, pour ces déjeuners animés et ces discussions passionnantes et passionnées (le plus souvent) : celles et ceux qui ont soutenu, Robin, Nicolas (co-fondu des sels fondus), Rodrigue, l'autre Nicolas, Kenneth, Emeline, Romain, Hunter, Téophile, Camilo, Francesco ; et ceux qui vont soutenir, Baptiste, Arthur, Olivier, Mathis (nouveau co-fondu des sels fondus mais seulement dans une direction), Gabriel, Kacim, Ruggero et Ayoub (toujours plus de co-fondus !), à qui je souhaite le meilleur pour leur suite et fin de thèse. Merci également aux thésards et ex-thésards côté CNRS, Thibault, Hugo et Thomas, pour ces bons moments passés en conférence.

D'un point de vue plus personnel, je remercie grandement mes amis, des plus anciens aux plus récents, pour ces moments passés ensemble et sans avoir à penser à des bugs de codes : toute la tribu LNA élargie (sans aller jusqu'à l'élargir à une batucada attention) pour ces voyages autour du monde, ces pouets et ces doots, ces festivals et concerts de qualité variable mais de fun assuré ; mes très chers Smoothies Loulou, Camille et Colin, ainsi que les Smooth élargis, qui seront, j'en suis sûr, ravis de se savoir cités dans un pavé de 150 pages de physique nucléaire, en attendant de finaliser cet opéra-boogie magistral qui sera assurément notre chef-d'oeuvre. Je remercie évidemment grandement Papa, Maman, et Mado pour leur soutien indéfectible et

inébranlable. Enfin, le plus grand des merci se doit d'aller à Cécile, sans qui tout serait à la fois beaucoup plus compliqué et beaucoup moins rigolo, ce qui n'est pas une perspective très réjouissante. Merci de m'accompagner depuis si longtemps, et pour encore un bout de chemin j'espère.

Faire de la recherche [...] ce n'est pas se parer (à tous les sens du terme), c'est s'exposer avec ses points faibles, ses faiblesses, une définition du progrès scientifique étant précisément qu'on baisse la garde, qu'on peut recevoir des coups.

Doing research [...] is not about shielding yourself (in every sense of the word), it's about exposing yourself with your weak points, your weaknesses, one definition of scientific progress being precisely that you let your guard down, that you can get hit.

Pierre Bourdieu, lesson at Collège de France, 1982

Introduction

Energy production and nuclear power

In 2019, the global energy consumption reached 116 000 terawatts hour (TWh) [1]. The global electricity consumption in 2019 reached 23 000 TWh, nearly 20% of the energy consumption [1].

The global electricity mix relies heavily on fossil fuels — 63% of the total in 2019 (Figure 1). Energy and heat production thus accounted for 30% of global greenhouse gas emissions in 2019. In order to limit global warming, the use of fossil fuels must be drastically reduced within the next years. This requires both an increased electricity share in the global energy mix — through the electrification of transportation and heating for exemple — and the decarbonisation of the global electricity mix.

Nuclear power is a controllable, low-carbon electricity source. It is thus one of the main tools at our disposal to decarbonise electricity production. Nuclear power yet suffers from some problems that hinder its global development:

- The complexity of the technology, associated with the risk of nuclear proliferation, hinders its implementation in developing countries.
- In developed countries, a significant proportion of the public opinion is opposed to nuclear power, mainly due to the risk of nuclear accidents and the difficulty to manage nuclear wastes.

The Generation IV International Forum (GIF [2]) is an international organisation that promotes the development of so-called fourth generation nuclear reactors. Generation IV designs must be efficient in fuel consumption and waste production, meet strict safety and non-proliferation standards, while being economically competitive. Six designs among around 120 have been selected by GIF, including the Molten Salt Reactor (MSR).

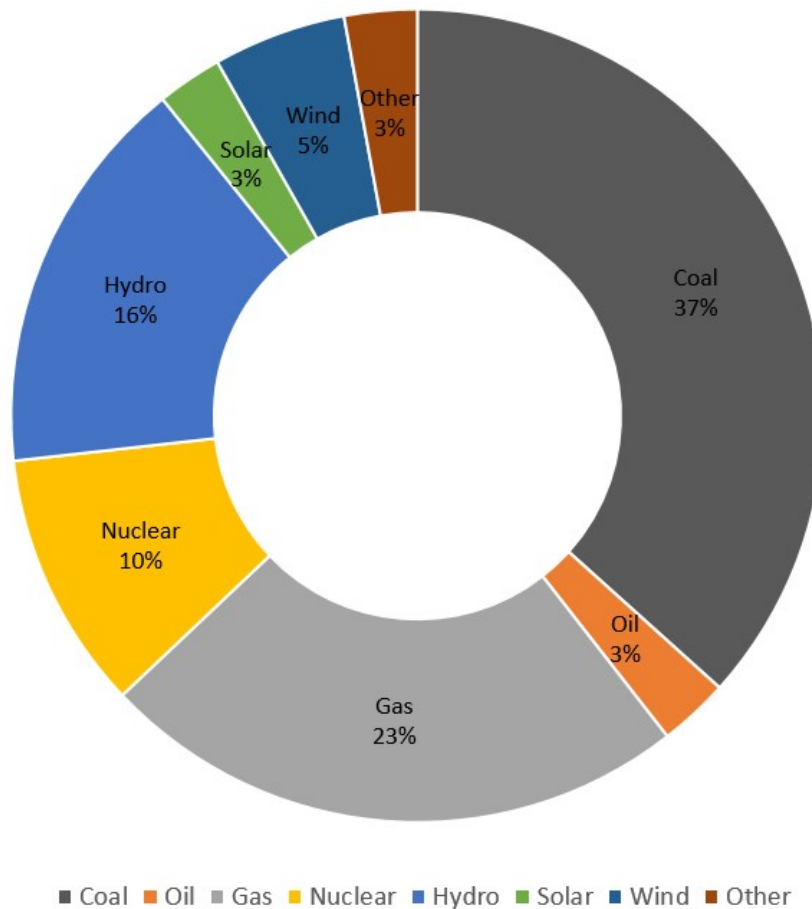


Figure 1: Global electricity mix in 2019 (data from IEA [1]).

Molten salt reactors from the past and present

In a circulating-fuel molten salt reactor, the nuclear fuel is liquid, in the form of a high-temperature salt, which acts both as the fuel and the primary coolant. This design has many advantages:

- The salt is at high temperature, which improves the thermodynamic efficiency of the reactor.
- The system operates at ambient pressure, which simplifies the reactor vessel design and reduces the risk of explosion.
- The system operates without water, sodium, or any flammable substance.
- In case of a breach, the liquid fuel will naturally flow into a collector beneath the core. It will cool and solidify in this collector, trapping radioactive species.

- The reactor has a strong negative temperature feedback coefficient, thanks to the fuel density feedback. This greatly improves the passive stability of the system, as well as its load-following capability.
- The fuel composition can be adjusted during operation, by batch or continuously. This limits the need for excess reactivity, and improves the reactor overall availability.
- The fuel being also the coolant, an MSR is a good fast-spectrum reactor candidate. A fast reactor can be used as a breeder to consume fertile matter — natural or depleted uranium, thorium — which would greatly increase the available fuel inventory. A fast reactor can also be used as a burner to consume actinides, which would reduce the nuclear fleet waste production.

The main drawback regarding the development of MSRs is their low Technology Readiness Level (TRL): few reactors have been built in the world, and many questions remain unanswered regarding the behaviour of such reactors, especially regarding the complex chemistry of the fuel salt. Despite their low TRL, MSRs are actually quite an "old" reactor concept.

The MSR concept was first studied in the 1950s at Oak Ridge National Laboratory (ORNL) [3]. The U.S. army at the time wanted to create a nuclear-propelled aircraft, and the compactness and load-following capability of an MSR made it a natural candidate. This Aircraft Nuclear Propulsion Project (ANP) led to the construction of the first-ever MSR, the Aircraft Reactor Experiment (ARE), at ORNL [4]. The ARE went critical in November 1954, and functioned for 221 hours before final shutdown.

Ten years later, ORNL started the construction of a bigger experiment, the Molten Salt Reactor Experiment (MSRE [5]). The MSRE went critical in 1965, and operated until 1969. The goal of the MSRE was to demonstrate the safety and reliability of a molten salt power reactor. ORNL started to develop such a reactor, through the Molten Salt Breeder Reactor Project (MSBR [6]). However, the funding for the project stopped in 1976 and the MSBR was never built.

The research on MSRs nonetheless subsisted. In France, studies and evaluations of the MSBR were performed by the Commissariat à l'Énergie Atomique (CEA) and Électricité de France (EDF) [7]. The TASSE concept [8] in CEA, as well as the AMSTER and REBUS concepts [9, 10] in EDF, were studied in the 1990s and 2000s.

In 1998, the Centre National de la Recherche Scientifique (CNRS) began working on MSR, and developed the Molten Salt Fast Reactor (MSFR) concept [11]. In 2001, the GIF was created and selected the MSR as a fourth generation reactor [2].

Since the 2010s, many MSR concepts are studied throughout national projects — MSFR in Europe [12], MOSART in Russia [13], TMSR in China [14] — and numerous startups [15–20].

The development of these different designs is mostly based on numerical simulations. These simulations in turn require the development of specific codes, adapted to the particular physics of MSRs — the strong temperature feedbacks, the transport of delayed neutron precursors with the flow, and the turbulent fluctuations in the core.

Turbulence and fluctuations in MSRs

In the ARE and the MSRE, the fuel salt flowed in the core through a lattice of pipes or channels surrounded by a moderator material — BeO or graphite. In more recent, fast-spectrum designs, like in the MSFR, the fuel salt flows freely through a toroidal-shaped core cavity.

This flow is usually highly turbulent. The velocity and temperature fields in the core thus fluctuate, which in turn causes the neutron flux and the power density distribution to fluctuate through the neutronic feedbacks. These turbulent fluctuations, depending on their amplitudes and frequencies, could disturb the reactor control and accelerate the ageing of the reactor vessel.

In order to model these fluctuations, simulations combining Computational Fluid Dynamics (CFD) and neutronics are necessary to correctly model the velocity, temperature, neutron flux and power density distributions. In CEA, a high-fidelity multiphysics calculation tool for MSR analysis has been developed, which couples existing calculation codes: the deterministic neutron transport code APOLL03[®] [21] — and notably its S_N -transport solver MINARET — and the CFD calculation platform TRUST/TrioCFD [22].

Objectives of this thesis

The goal of this PhD thesis is to model and analyse turbulent fluctuations in MSR cores, using CEA’s multiphysics tool.

In the first two chapters, we introduce the equations that describe the neutronic

and thermal-hydraulic behaviour of a nuclear reactor, and how they are coupled in an MSR. We then present how these equations can be discretised and numerically solved. Finally, we present some multiphysics codes developed for MSR simulations, and more specifically the CEA code **APOLL03[®] – TrioCFD**.

The objective of the third chapter is to validate the **APOLL03[®] – TrioCFD** code by developing a numerical model of the historical Aircraft Reactor Experiment (ARE). To achieve this, the first step is to create a thermal-hydraulic numerical model of the ARE in **TrioCFD**, a neutronic numerical model of the ARE in **APOLL03[®]**, and to couple both models. The second step is to reproduce selected experiments performed on the ARE using our numerical model, in order to validate the multiphysics code on experimental data.

In the fourth chapter, the objective is to use the **APOLL03[®] – TrioCFD** code to model the turbulent fluctuations in the Molten Salt Fast Reactor (MSFR) design. To achieve this, the first step is to create a thermal-hydraulic numerical model of the MSFR in **TrioCFD**, and to perform CFD-only simulations of the core in order to assess the sensitivity of our model to different parameters, and compare our simulations with other CFD codes. The second step is to create a neutronic numerical model of the MSFR in **APOLL03[®]**, and to couple it with our thermal-hydraulic model. The last step is to couple both models and to perform steady-state and transient simulations.

Chapter I

Reminders on nuclear reactor physics

The purpose of this chapter is to present elements of neutronics (Section I.1) and thermal-hydraulics (Section I.2) that are involved in nuclear reactor physics, as well as the equations governing both physics. We then show how these equations are modified and coupled in the specific case of molten salt reactor physics (Section I.3).

The material reported here is mostly taken from [23–25] for neutronics, and [26–28] for thermal-hydraulics.

I.1	Neutronics	23
	I.1.a The fission process and the chain reaction	23
	I.1.b Cross sections and neutronic feedbacks	25
	I.1.c Fast and thermal neutrons	27
	I.1.d Delayed neutrons and effective delayed neutron fraction	28
	I.1.e The Boltzmann equation	29
	I.1.f The steady-state Boltzmann equation	32
	I.1.g The adjoint problem and adjoint flux	33
I.2	Thermal-hydraulics	33

I.2.a	Eulerian specification and Navier-Stokes equations	33
I.2.b	The pressure equation	34
I.2.c	Turbulent flows	35
I.2.d	Turbulent transport of energy and concentration	37
I.2.e	Buoyancy: the Boussinesq approximation	38
I.2.f	Wall flows	39
I.3	Molten salt reactors physics	41
I.3.a	The coupled neutronic–thermal-hydraulic problem	41
I.3.b	Transport of the delayed neutrons precursors	42
I.3.c	Wall laws for MSRs	43

I.1 Neutronics

I.1.a The fission process and the chain reaction

In a nuclear reactor, the energy comes mainly from fission processes. Following the discovery of the atomic nucleus by Rutherford in 1911 [29] and the discovery of the neutron by Chadwick in 1932 [30], Hahn and Strassmann bombarded uranium nuclei with neutrons in 1938 [31, 32] in order to obtain elements heavier than uranium, but instead observed the formation of light elements — around half the atomic number of uranium. Meitner and Frisch explained this phenomenon in February 1939 by theorizing nuclear fission [33]. They also estimated the released energy of fission at about 200 mega-electronvolts (MeV). In March of the same year, Von Halban and al. discovered that the fission reaction generated new neutrons [34], which led to the possibility of a chain reaction [35].

In a neutron-induced fission, a target nucleus — for example ^{235}U — absorbs a neutron. The new nucleus is highly unstable and may emit neutrons and photons, before breaking into two (or more) fragments, called the primary fragments. The time between the neutron absorption and the scission is around 10^{-20} s. A schematic view of the neutron-induced fission of ^{235}U is presented in Figure I.1.

The primary fragments very rapidly emit new neutrons, called prompt neutrons, and become secondary fragments (around 10^{-16} s after neutron absorption); these secondary fragments can in turn β -decay into more stable nuclei — called the fission products — releasing photons and neutrons through (β, n) reactions, called the delayed neutrons, emitted between 10^{-3} and 10 s after fission.

The mass energy of the fragments is lower than the mass energy of the initial nucleus, so the reaction is exothermal — about 200 MeV are released during the fission of ^{235}U . The released energy is spread between the kinetic energy of the fission products ($\sim 85\%$), the energy of prompt neutrons and photons ($\sim 6\%$), the energy of β -decay neutrons and photons ($\sim 6\%$), and the energy of β -decay neutrinos ($\sim 3\%$).

The average number of neutrons (prompt and delayed) emitted per fission, called the neutron multiplicity and noted ν , is about 2.4 for ^{235}U . These emitted neutrons can in turn provoke new fissions, causing a chain reaction. In a nuclear reactor, the chain reaction must be controlled in order to ensure that one fission causes exactly one new fission. We define the effective neutron multiplication factor, noted k_{eff} , as the ratio of neutrons in generation $(n+1)$ to the number of neutrons in generation n ; the reactivity is in turn defined as $\rho = (k_{eff} - 1)/k_{eff}$. The chain reaction is exactly self-sustained for $k_{eff} = 1$, or $\rho = 0$.

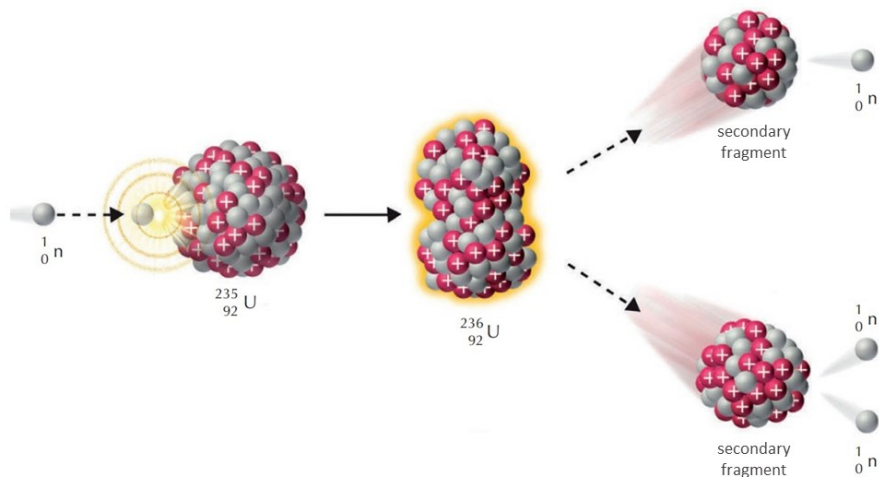


Figure I.1: Schematic view of the neutron-induced fission of ^{235}U .

I.1.b Cross sections and neutronic feedbacks

A neutron-nucleus interaction does not necessarily result in a fission. The neutron can also be absorbed by the nucleus without causing a fission (this is called a capture), or be scattered by the nucleus. The probabilities for these different interactions are linked to the microscopic cross sections for these interactions, noted σ , and usually expressed in barns ($1 \text{ b} = 10^{-24} \text{ cm}^2$). The microscopic cross sections are determined both by measurements and quantum mechanics calculations. They depend on the nucleus and the incident energy, and present many resonances (see Figure I.2). Nuclei that present a higher fission cross section than their capture cross section are considered "fissile", while the other nuclei are considered "non-fissile" — such "non-fissile" nuclei can still undergo a fission, but it is less likely than for "fissile" nuclei.

The microscopic cross section describes the interaction probability for one nucleus. A more useful parameter for nuclear reactor physics is the macroscopic cross section, which is the product of the microscopic cross section by the nuclei density in matter:

$$\Sigma = \sigma N \tag{I.1}$$

The macroscopic cross sections depend on the matter temperature through two phenomena. The first, most intuitive one is the so-called density feedback: when the matter heats up, its volume increases and its density decreases, which lowers the macroscopic cross sections.

The other major temperature feedback is known as the Doppler feedback: when the matter heats up, the increased thermal motion of the nuclei in matter enables more neutron energy values to cause an interaction. This causes the microscopic cross sections resonances to widen, increasing the mean number of interactions. The Doppler feedback is illustrated in Figure I.3.

For nuclear reactor applications, it is important to ensure that these temperature feedbacks are negative, i.e that a temperature increase of the reactor causes the reactor reactivity to decrease — which will in turn lowers the generated power and the temperature. For the density feedback, a temperature increase causes a decrease of all neutron-matters interactions and more neutron leakage, which lowers the reactivity. For the Doppler feedback however, a temperature increase causes an increase of all interactions, including fissions and captures; ensuring that the mean number of captures increases more than the mean number of fissions will result in an overall negative

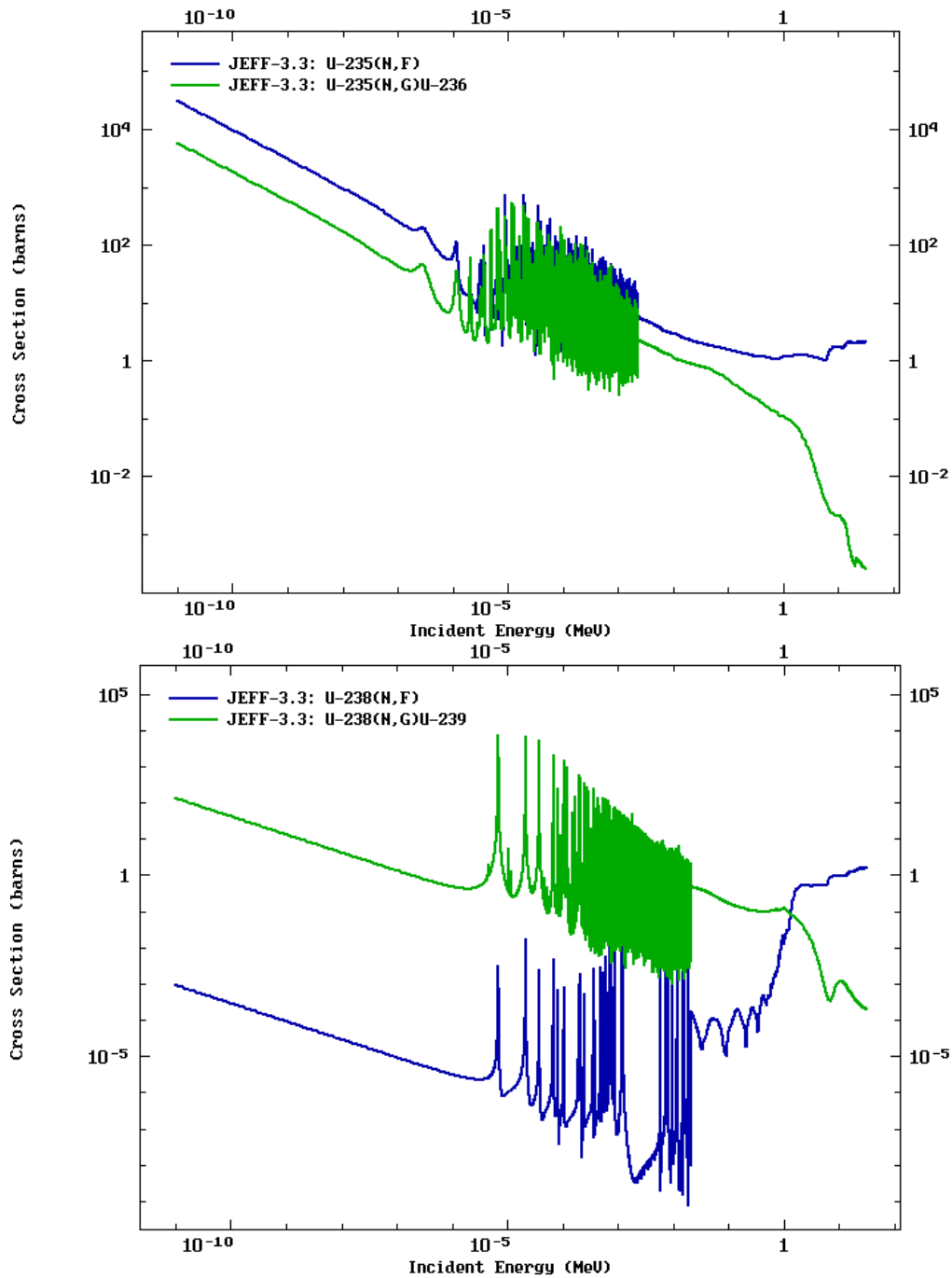


Figure I.2: Microscopic cross sections of the neutron-induced fission (blue) and the radiative capture (green) for a "fissile" nucleus (^{235}U , top), and a "non-fissile" nucleus (^{238}U , bottom). Data from JEFF-3.3 [36], visualisation from IAEA Nuclear Data Services [37].

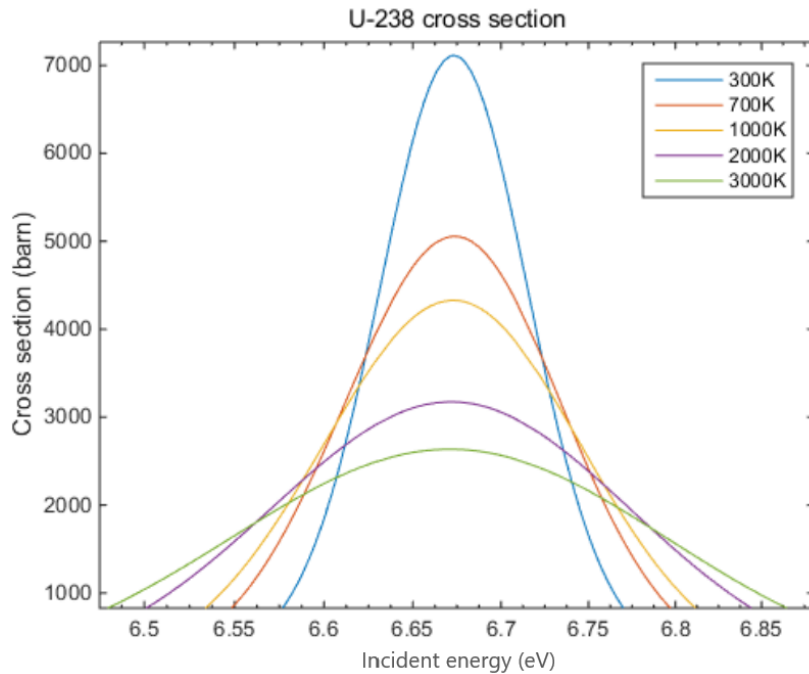


Figure I.3: Doppler broadening of the ^{238}U neutron capture resonance at 6.67 eV [38].

Doppler feedback.

Both these temperature feedbacks are usually combined in a global reactor temperature feedback, expressed as a reactivity variation (usually expressed in per cent mille, $1 \text{ pcm} = 10^{-5}$) per degree. In solid-fuel reactors, the Doppler feedback is usually the predominant feedback. In MSRs however, because the fuel is liquid, the density feedback is much larger than the Doppler feedback, and the global temperature feedback is quite larger than in solid-fuel reactors. The density feedback in MSRs is also improved by the fact that fissile matter can actually leave the critical region of the core with a sufficient volume increase. This large temperature feedback coefficient is the main reason for the increased, passive stability of MSRs.

I.1.c Fast and thermal neutrons

The prompt neutrons emitted during the fission have a high kinetic energy (between 10^{-1} and 10 MeV with a mean value at 2 MeV), and are thus called fast neutrons. For this energy range, the fission cross section is very low (see Figure I.2).

In most nuclear reactors, called thermal-spectrum reactors, the neutrons are slowed through collisions in a moderator material, in order to reach the thermal energy

range (between 10^{-8} and 10^{-7} MeV) where the cross sections are much higher. This moderator is usually composed of light nuclei in order to maximize the energy transfer through scattering. It must also have a low capture cross section. Typical moderators include water, heavy water, graphite, and beryllium.

In some reactors, called fast-spectrum reactors, there is no moderator. These reactors use a combination of a "fissile" material and a "fertile" material (typically ^{233}U / ^{232}Th or ^{239}Pu / ^{238}U). The neutrons are not slowed down, which reduces the fissions in the fissile material, but increases the absorptions in the fertile material, which can transmute into the fissile material. If the creation of fissile material is higher than its consumption (positive breeding ratio), the reactor is a breeder reactor, and can operate with fertile materials only, which are much more abundant than fissile materials — fissile material is still required for the breeder start-up.

I.1.d Delayed neutrons and effective delayed neutron fraction

Not all the neutrons in a reactor are prompt neutrons. Some secondary fragments can undergo a β -decay and emit delayed neutrons through a (β, n) reaction. These fragments are called delayed neutron precursors, and are usually regrouped in different families based on their mean decay time λ — typically between 4 and 8 precursors groups.

The delayed neutrons are essential for reactor operation: their generation time being more than a thousand times higher than the prompt neutron generation time, we must ensure that the reactor is sub-critical with prompt neutrons only, and that criticality comes from the delayed neutrons. We note β the delayed neutron fraction, which is usually around several 100 pcm.

Delayed neutrons are emitted with a lower energy than prompt neutrons (around ten times lower, see Figure I.4), which has an impact on the interaction cross sections. The delayed neutron spatial distribution is also different from the prompt neutron distribution, especially in an MSR where the precursors are transported by the fuel. This spatial distribution has an impact on the probability of interactions: depending on where the neutron is emitted, its probability to react with matter or to escape the core without interacting will vary.

These energetic and spatial discrepancies between the prompt and delayed neutrons must be taken into account when comparing the prompt and delayed neutron fractions. This is why we define an effective delayed neutron fraction β_{eff} :

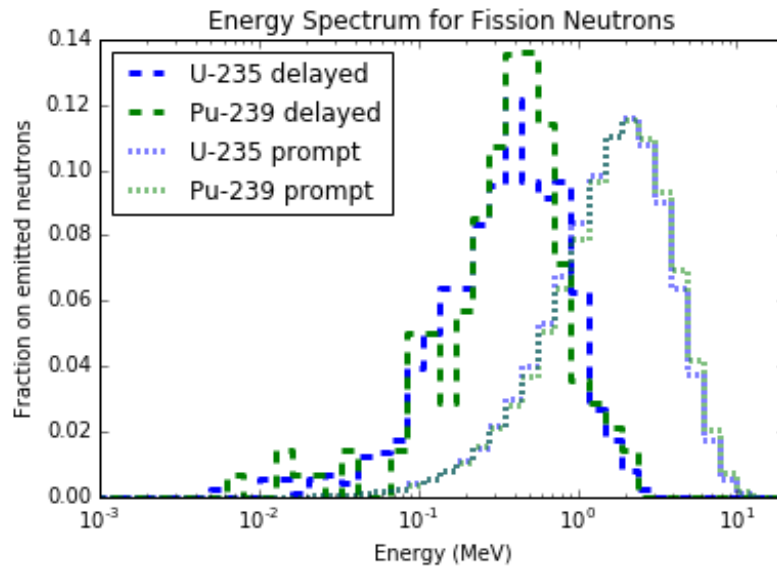


Figure I.4: Typical delayed and prompt neutrons spectrum for ^{235}U and ^{239}Pu [39].

$$\beta_{eff} = \beta I \quad (\text{I.2})$$

With I an importance factor (usually computed through the adjoint neutron flux calculation, see Section I.1.g). The condition for a critical, prompt sub-critical reactor can thus be written as:

$$\begin{cases} k_{eff} = k_{p,eff} + \beta_{eff} k_{eff} = 1 \\ k_{p,eff} < 1 \end{cases} \quad (\text{I.3})$$

With $k_{p,eff}$ the prompt neutrons multiplication factor.

I.1.e The Boltzmann equation

Neutronics is the study of the neutron transport in a nuclear reactor. There are two main ways to determine the evolution of the neutron population:

- To simulate a great number of neutrons in the reactor, and to reproduce their interactions with matter by random draws. This is known as the Monte-Carlo method, which is used in stochastic neutronic codes. This method was not used in this thesis, therefore it will not be presented here.

- To obtain a balance equation for the evolution of the neutron flux, and to solve it numerically. This method is used by deterministic neutronic codes — like APOLL03[®], which was used in this thesis.

In order to obtain the neutron balance equation, hypotheses are made:

- We assume there are enough neutrons in the reactor to define a neutron density at any point in the phase space — this hypothesis is similar to the continuum hypothesis in thermal-hydraulics. In a nuclear reactor, the neutron density is about 10^8 cm^{-3} , which justifies this hypothesis.
- We assume that the neutrons only react via neutron-matter interactions, the neutron-neutron interactions as well as the neutron decays are neglected. In a nuclear reactor, the ratio of neutron density to matter density is about 10^{-15} and the ratio of the mean neutron lifetime in a reactor to the mean neutron decay time is about 10^{-7} , which justifies this hypothesis.
- We assume that the neutrons are non-relativistic particles. In a nuclear reactor, the maximum kinetic neutron energy is about 15 MeV, which is about 1.5% of its mass energy.
- We assume that the fission reactions are isotropic — so the fission cross section does not depend on the angle of the incident neutron.

The balance equation for the neutron population with these hypotheses is called the neutron transport equation, or Boltzmann equation. It is written as:

$$\frac{1}{|\mathbf{v}|} \frac{\partial \psi(t, \mathbf{r}, \boldsymbol{\omega}, E)}{\partial t} = (-\mathcal{L} + \mathcal{S} + \mathcal{F} + \mathcal{D}) \psi(t, \mathbf{r}, \boldsymbol{\omega}, E) + S(t, \mathbf{r}, \boldsymbol{\omega}, E) \quad (\text{I.4})$$

With ψ the neutron flux, depending on time t , position \mathbf{r} , direction or angle $\boldsymbol{\omega}$ and energy E ; \mathbf{v} the neutron velocity; S a source term; $\mathcal{L}, \mathcal{S}, \mathcal{F}, \mathcal{D}$ are the loss, scattering, prompt fission and delayed fission operators, defined as follows:

$$\begin{aligned}
 \mathcal{L} \psi(t, \mathbf{r}, \boldsymbol{\omega}, E) &= (\boldsymbol{\omega} \cdot \nabla + \Sigma_t(t, \mathbf{r}, E)) \psi(t, \mathbf{r}, \boldsymbol{\omega}, E) \\
 \mathcal{S} \psi(t, \mathbf{r}, \boldsymbol{\omega}, E) &= \int_{E_{min}}^{E_{max}} \int_{\mathbb{S}_2} \Sigma_s(t, \mathbf{r}, \boldsymbol{\omega}' \rightarrow \boldsymbol{\omega}, E' \rightarrow E) \psi(t, \mathbf{r}, \boldsymbol{\omega}', E') dE' d\boldsymbol{\omega}' \\
 \mathcal{F} \psi(t, \mathbf{r}, \boldsymbol{\omega}, E) &= \frac{\chi_p(E)}{4\pi} \int_{E_{min}}^{E_{max}} (1 - \beta) \nu(E') \Sigma_f(t, \mathbf{r}, E') \phi(t, \mathbf{r}, E') dE' \\
 \mathcal{D} \psi(t, \mathbf{r}, \boldsymbol{\omega}, E) &= \sum_{i=1}^N \frac{\chi_{d,i}(E)}{4\pi} \lambda_i C_i(t, \mathbf{r})
 \end{aligned} \tag{I.5}$$

With χ_p the prompt neutrons energy spectrum, β the delayed neutron fraction, ν the total neutron multiplicity, ϕ the scalar neutron flux, which is the neutron flux integrated over all angles; $\chi_{d,i}$ the delayed neutrons energy spectrum for the i -th precursor group, λ_i the decay constant for this group, and C_i the concentration of this group. Σ_t , Σ_s and Σ_f are the total, scattering, and fission macroscopic cross sections. It is important to note that these cross sections depend on the matter temperature through both the Doppler effect and the matter density.

The precursor concentration equations for a solid-fuel reactor are as follows:

$$\begin{aligned}
 \frac{\partial C_i(t, \mathbf{r})}{\partial t} &= -\lambda_i C_i(t, \mathbf{r}) + S_{C_i}(t, \mathbf{r}) \\
 S_{C_i}(t, \mathbf{r}) &= \beta_i \int_{E_{min}}^{E_{max}} \nu(E') \Sigma_f(t, \mathbf{r}, E') \phi(t, \mathbf{r}, E') dE'
 \end{aligned} \tag{I.6}$$

With S_{C_i} the production of precursors through fission reactions, which depends on β_i the delayed neutron fraction of the i -th group. One precursor is assumed to create exactly one delayed neutron.

A transport equation for the photons in the reactor should also be solved, as photons contain a non-negligible fraction of the fission energy (between 3 and 4 %). However, it is common not to model the photons in a reactor, and to "redirect" the photons energy into the neutrons. Photons were not modelled in this thesis.

Equations I.4 and I.6 do not take into account the evolution of the different materials in the reactor — fuel consumption, fission products creation, activation of materials. The fuel composition evolution in a reactor is described by the Bateman equations [40]. They will not be presented here, as they were not used in this thesis — all the neutronic calculations were performed with fixed compositions.

I.1.f The steady-state Boltzmann equation

For a solid-fuel reactor, the steady-state precursor concentrations can be expressed as:

$$\lambda_i C_i = \beta_i \int_{E_{min}}^{E_{max}} \nu \Sigma_f \phi \, dE' \quad (I.7)$$

Equation I.7 can be used in the expression of the delayed fission operator \mathcal{D} to obtain the steady-state transport equation — we assume there is no source term:

$$(-\mathcal{L} + \mathcal{S} + \mathcal{F}_\infty) \psi = 0 \quad (I.8)$$

With \mathcal{F}_∞ the steady-state fission operator combining the prompt and delayed operators:

$$\mathcal{F}_\infty \psi = \left(\frac{\chi_p}{4\pi} (1 - \beta) + \sum_{i=1}^N \frac{\chi_{d,i}}{4\pi} \beta_i \right) \int_{E_{min}}^{E_{max}} \nu \Sigma_f \phi \, dE' \quad (I.9)$$

Unfortunately, for a real-life system, the steady-state Equation I.8 does not have a non-trivial solution. This is because a real-life reactor is never perfectly critical, so it is never at steady-state, but rather evolves slowly. In order to obtain a non-trivial solution of the steady-state problem, we force the criticality of the system by introducing a multiplication factor in the fission term:

$$\left(-\mathcal{L} + \mathcal{S} + \frac{1}{k_{eff}} \mathcal{F}_\infty \right) \psi = 0 \quad (I.10)$$

Equation I.10 is an eigenvalue problem, with k_{eff} the highest eigenvalue of the equation, and ψ its corresponding eigenvector. This eigenvalue corresponds to the physical k_{eff} described above (Section I.1.a): dividing the fission operator by the k_{eff} ensures that one fission causes exactly one fission, making the system critical.

I.1.g The adjoint problem and adjoint flux

A useful parameter for neutronics is the adjoint neutron flux ψ^* , which is the solution of the steady-state adjoint Boltzmann equation, which describes the *reverse* path of the neutrons:

$$(\mathcal{F} + \mathcal{D})\psi^* = (-\boldsymbol{\omega} \cdot \nabla + \Sigma_t - \mathcal{S})\psi^* \quad (\text{I.11})$$

The adjoint equation is similar to the direct equation, with the source and sink terms inversed. The scalar adjoint neutron flux ϕ^* is usually used to compute the effective delayed neutron fraction β_{eff} [41]:

$$\beta_{eff} = \frac{\int \phi^*(\mathbf{r}, E') \chi_d(\mathbf{r}, E') \nu_d(\mathbf{r}, E) \Sigma_f(\mathbf{r}, E) \phi(\mathbf{r}, E) dE dE' d\mathbf{r}}{\int \phi^*(\mathbf{r}, E') \chi(\mathbf{r}, E') \nu(\mathbf{r}, E) \Sigma_f(\mathbf{r}, E) \phi(\mathbf{r}, E) dE dE' d\mathbf{r}} \quad (\text{I.12})$$

I.2 Thermal-hydraulics

I.2.a Eulerian specification and Navier-Stokes equations

The usual way to model fluid dynamics is to consider not the liquid molecules moving, but rather the flow fields — such as velocity and density — as continuous functions of space and time. This is known as the Eulerian specification of the flow field. It relies on the continuum hypothesis that assumes that the length and time scales of the molecular motions are very small compared to the flow length and time scales. This hypothesis is verified by computing the Knudsen number K_N , defined as:

$$K_N = \frac{\lambda}{L} \quad (\text{I.13})$$

With λ the mean free path of the particles considered, and L the typical length of the domain considered. The continuum hypothesis holds for $K_N \ll 1$, which is the case for most thermal-hydraulic applications.

To describe a continuum flow, we only need to obtain a balance equation for the density and velocity fields. The mass-conservation equation is written as:

$$\frac{\partial \rho(\mathbf{r}, t)}{\partial t} + \nabla \cdot (\rho(\mathbf{r}, t) \mathbf{u}) = 0 \quad (\text{I.14})$$

With ρ the density field and \mathbf{u} the velocity field — it is actually $\mathbf{u}(\mathbf{r}, t)$, condensed into \mathbf{u} for clarity. In the case of incompressible fluids, the density is assumed constant: $\rho(\mathbf{r}, t) = \rho$. The equation can thus be simplified:

$$\nabla \cdot \mathbf{u} = 0 \quad (\text{I.15})$$

The momentum equation is written as:

$$\frac{\partial \mathbf{u}}{\partial t} + \mathbf{u} \cdot \nabla \mathbf{u} = \frac{1}{\rho} \nabla \cdot \boldsymbol{\sigma} + \mathbf{g} \quad (\text{I.16})$$

With $\boldsymbol{\sigma}$ the Cauchy stress tensor, and \mathbf{g} the body forces — typically gravity. For constant-properties, Newtonian fluids, the stress tensor can be separated into a symmetric tensor and a pressure term:

$$\sigma_{i,j} = -P \delta_{i,j} + \mu \left(\frac{\partial u_i}{\partial x_j} + \frac{\partial u_j}{\partial x_i} \right) \quad (\text{I.17})$$

With P the pressure and μ the assumed constant dynamic viscosity. By combining Equations I.15, I.16 and I.17, we obtain the Navier-Stokes equations for an incompressible, Newtonian, constant-properties fluid:

$$\frac{\partial \mathbf{u}}{\partial t} + \mathbf{u} \cdot \nabla \mathbf{u} = -\frac{1}{\rho} \nabla P + \nu \nabla^2 \mathbf{u} + \mathbf{g} \quad (\text{I.18})$$

With $\nu = \mu/\rho$ the kinematic viscosity.

I.2.b The pressure equation

An equation for the pressure is required to solve the above Navier-Stokes equations. Firstly, if the body forces are conservative, they derive from a potential Ψ :

$$\mathbf{g} = -\nabla \Psi \quad (\text{I.19})$$

These conservative body forces can thus be grouped with the pressure term into a modified pressure p . The Navier-Stokes equations are then written:

$$\frac{\partial \mathbf{u}}{\partial t} + \mathbf{u} \cdot \nabla \mathbf{u} = -\frac{1}{\rho} \nabla p + \nu \nabla^2 \mathbf{u} + S_m \quad (\text{I.20})$$

$$p = P + \rho \Psi$$

With S_m a source term that contains the non-conservative body forces. The equation for the modified pressure is obtained by taking the divergence of the Navier-Stokes equations (I.20):

$$\nabla^2 p = -\rho \frac{\partial u_i}{\partial x_j} \frac{\partial u_j}{\partial x_i} \quad (\text{I.21})$$

The Einstein notation is used for simplicity. For an incompressible fluid, the pressure field can thus be written as a function of the velocity field.

I.2.c Turbulent flows

The Navier-Stokes equations are non-linear, and fall under the chaos theory. A useful parameter to characterize flows is the Reynolds number, defined as the ratio of the inertial forces $\mathbf{u} \cdot \nabla \mathbf{u}$ to the viscous forces $\nu \nabla^2 \mathbf{u}$:

$$Re \sim \frac{\mathbf{u} \cdot \nabla \mathbf{u}}{\nu \nabla^2 \mathbf{u}} \sim \frac{U * U/D}{\nu U/D^2} \sim \frac{UD}{\nu} \quad (\text{I.22})$$

With U and D the typical velocity and width of the flow. The Reynolds number value is used to define the type of flow: laminar for low Re , turbulent for high Re , transitional in-between. The threshold values depend on the geometry and type of flow considered; for a flow in a smooth, circular pipe, the flow is laminar for $Re < 2300$ and turbulent for $Re > 2900$.

In laminar flows, the fluid follows a smooth path. Turbulent flows on the other hand are characterised by the presence of eddies and a very high sensitivity to initial conditions that results in an apparent random behaviour. For turbulent flows, the Navier-Stokes equations must be solved numerically, using different methods (see Section II.2).

Fully developed turbulence nonetheless presents a structure that can be described as an energy cascade [42]: large eddies are created, that break into smaller eddies, that break into even smaller eddies, and so on until the smallest eddies dissipate their energy through viscous dissipation (Figure I.5).

For locally homogeneous, isotropic turbulence, Kolmogorov studied the energy cascade and obtained length, time and velocity scales for the dissipation range [43–45]. These microscales are defined as:

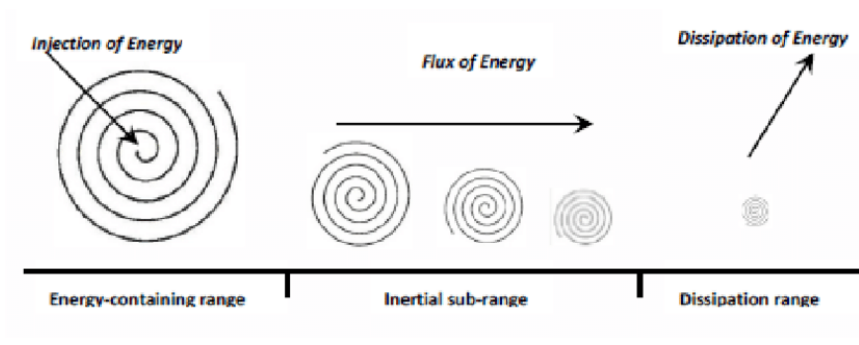


Figure I.5: Schematic view of the turbulent energy cascade.

$$\text{Kolmogorov length scale: } \eta = \left(\frac{\nu^3}{\epsilon} \right)^{1/4}$$

$$\text{Kolmogorov time scale: } \tau_\eta = \sqrt{\frac{\nu}{\epsilon}} \quad (\text{I.23})$$

$$\text{Kolmogorov velocity scale: } u_\eta = (\nu\epsilon)^{1/4}$$

With ν the kinematic viscosity and ϵ the average rate of dissipation of turbulent kinetic energy per unit mass (see Section II.2.d). On the turbulent energy spectrum — the plot of turbulent energy E over all the eddies wavenumbers κ — three ranges can be defined: the energy-containing range for the large eddies, the inertial sub-range for intermediate eddies, and the dissipation range for the small eddies (Figure I.6). Kolmogorov predicted the shape of the turbulent energy spectrum in the inertial sub-range, assumed to be flow-independent:

$$E = C \epsilon^{2/3} \kappa^{-5/3} \quad (\text{I.24})$$

With κ the wavenumber and C a constant, experimentally determined around 1.5. The total turbulent energy k and the dissipation rate ϵ can be computed from the energy spectrum:

$$k = \int_0^{\infty} E(\kappa) d\kappa \quad (I.25)$$

$$\epsilon = \int_0^{\infty} 2\nu\kappa^2 E(\kappa) d\kappa$$

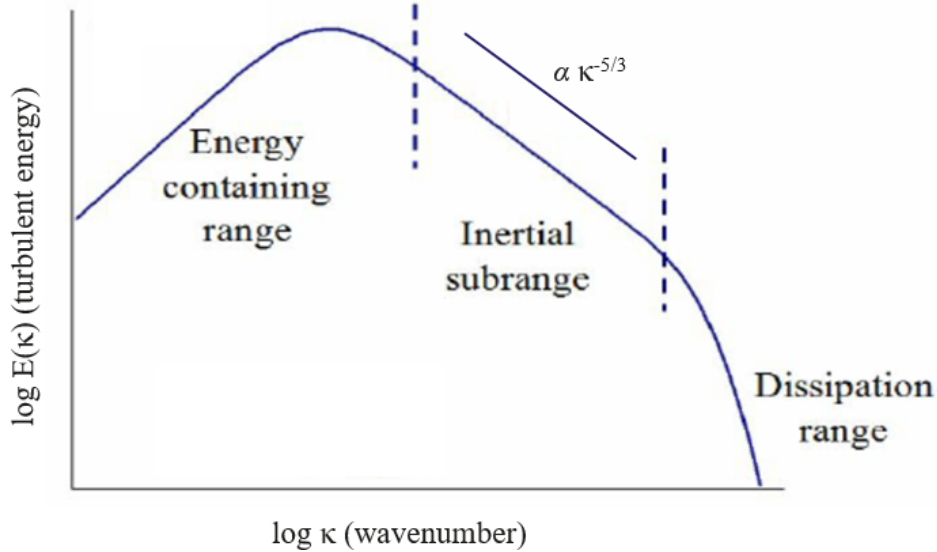


Figure I.6: A typical turbulent energy spectrum.

The turbulent energy spectrum is an important concept for defining Direct Numerical Simulations (DNS) and Large Eddy Simulations (LES) (see Section II.2).

I.2.d Turbulent transport of energy and concentration

In thermal-hydraulics, the velocity, density and pressure fields are not the only unknowns. We also need to determine the temperature field, which is given by the energy balance equation for a constant-properties, incompressible fluid:

$$\frac{\partial T}{\partial t} + \mathbf{u} \cdot \nabla T = \alpha \nabla^2 T + S_{th} \quad (I.26)$$

$$\alpha = \frac{\lambda}{\rho c_p}$$

With α the thermal diffusivity, λ the thermal conductivity, c_p the specific heat capacity, and S_{th} a source term. Radiation is not modelled here. As the temperature

field depends on the velocity through the advection term, in the case of a turbulent flow, the temperature field is also turbulent. Concentrations of chemical species — for example the delayed neutron precursors in an MSR — follow a very similar transport equation for a constant-properties, incompressible fluid:

$$\frac{\partial C}{\partial t} + \mathbf{u} \cdot \nabla C = D_m \nabla^2 C + S_C \quad (\text{I.27})$$

With D_m the mass diffusivity and S_C a source term.

I.2.e Buoyancy: the Boussinesq approximation

For thermal-hydraulic studies with large temperature gradients, buoyancy effects — caused by the density variation with temperature — can be significant. A temperature-dependant density can be modelled as follows:

$$\rho = \rho_0 + \rho_0 \beta_{th}(T - T_0) \quad (\text{I.28})$$

With ρ_0 the reference density, β_{th} the thermal expansion coefficient, and T_0 a reference temperature.

The problem with this modelling is that the fluid density is not constant any more. Equation I.15 is no more valid, and the Navier-Stokes equations should be modified as well. A convenient way to model buoyancy effects without changing the equations is to use the Boussinesq approximation — not to be confused with the Boussinesq hypothesis (see Section II.2.d). The approximation states that the density variation is important only along the vertical axis, in the gravitation term. It simply adds a source term to the incompressible Navier-Stokes equations:

$$\frac{\partial \mathbf{u}}{\partial t} + \mathbf{u} \cdot \nabla \mathbf{u} = -\frac{1}{\rho_0} \nabla p + \nu \nabla^2 \mathbf{u} - \mathbf{g} \beta_{th}(T - T_0) + S_m \quad (\text{I.29})$$

$$p = P - \rho_0 \mathbf{g} \cdot \mathbf{u}_z$$

With \mathbf{g} the gravitation acceleration, and \mathbf{u}_z the unit vector for the vertical axis. The Boussinesq approximation is valid only for small density variations ($\Delta\rho \ll \rho_0$), and is mostly useful for natural convection flows. In this thesis, where convection was always forced — either with a pump or a set inlet flow rate — the approximation was used nonetheless.

I.2.f Wall flows

For wall-bounded flows, the velocity at the wall is usually assumed null (no-slip condition). Therefore, the velocity field near the wall — a zone called the inner layer — is small. When the flow is parallel to the assumed smooth wall, universal near-wall laws can be applied. At the wall, since the velocity is null, the shear stress can be written as a pure viscous stress:

$$\tau_w = \rho\nu \left(\frac{\partial u_x}{\partial y} \right)_{y=0} \quad (\text{I.30})$$

With u_x the axial velocity, and y the distance perpendicular to the wall with its origin at the wall.

Using this shear stress expression, we can define a dimensionless velocity u^+ and a dimensionless distance to the wall y^+ :

$$y^+ = \frac{y}{\nu} \sqrt{\frac{\tau_w}{\rho}} \quad (\text{I.31})$$

$$u^+ = u \sqrt{\frac{\rho}{\tau_w}}$$

Prandtl found that very near to the wall, in a region called the viscous sublayer ($y^+ < 5$), the velocity depended only on the viscous phenomena [46]; he thus defined the law of the wall as:

$$u^+ = y^+ \quad (\text{I.32})$$

This law has been verified both experimentally and through numerical simulations (see Figure I.7). For larger y^+ however, the law of the wall does not stand. Von Karman, assuming that the viscosity was negligible at higher y^+ , derived another law [47], called the logarithmic law of the wall (log law):

$$u^+ = \frac{1}{\kappa^*} \ln(y^+) + B \quad (\text{I.33})$$

With $\kappa^* \approx 0.41$ the Von Karman constant, and B a constant experimentally determined at 5.2. The log law has been verified both experimentally and through numerical simulations (see Figure I.8). It holds for $30 < y^+ < 300$. Between the two different regions, in the buffer region ($5 < y^+ < 30$), neither law applies, although

different smoothing models that can be applied in the whole inner layer exist — for example Reichardt’s law [48]:

$$u^+ = \frac{1}{\kappa^*} \ln(1 + \kappa^* y^+) + 7.8 \left(1 - e^{-y^+/11} - \frac{y^+}{11} e^{-y^+/3} \right) \quad (\text{I.34})$$

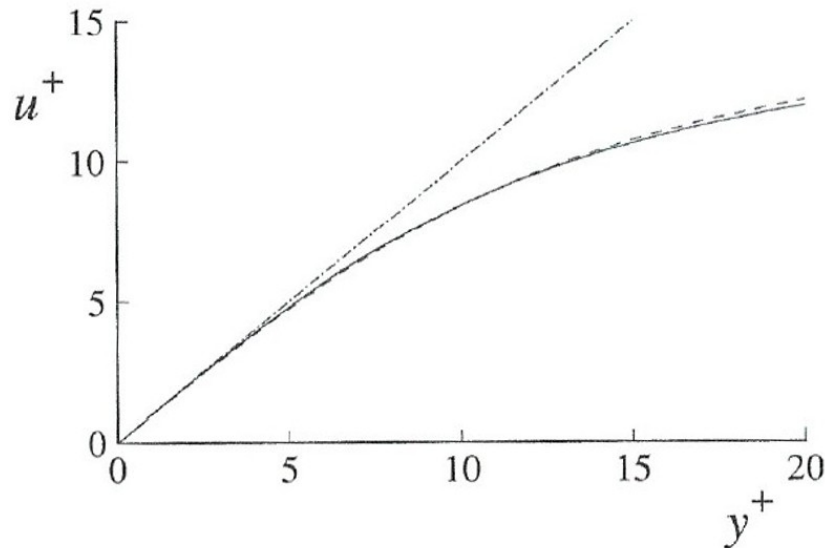


Figure I.7: The wall law (straight, dot-dashed line) plotted against DNS data (curved lines) at two different Reynolds numbers, taken from Pope [26].

These wall laws can be used in numerical simulations in order to reduce the computation time of the calculations (see Section II.2).

Similar laws can be derived for the energy equation in the case of non-adiabatic walls. In the inner layer ($y^+ < 30$), the wall laws is:

$$T^+ = \text{P}_R y^+ \quad (\text{I.35})$$

$$T^+ = \frac{c_p \sqrt{\rho \tau_w} (T_w - T)}{Q_w}$$

With T^+ the dimensionless temperature, T_w the temperature of the wall, Q_w the heat transfer at the wall, and P_R the Prandtl number, defined as $\text{P}_R = \mu c_p / \lambda$. For the outer part of the inner layer ($30 < y^+ < 300$), a log-law can be derived:

$$u^+ = \frac{1}{\kappa_{th}^*} \ln(y^+) + B_{th} \quad (\text{I.36})$$

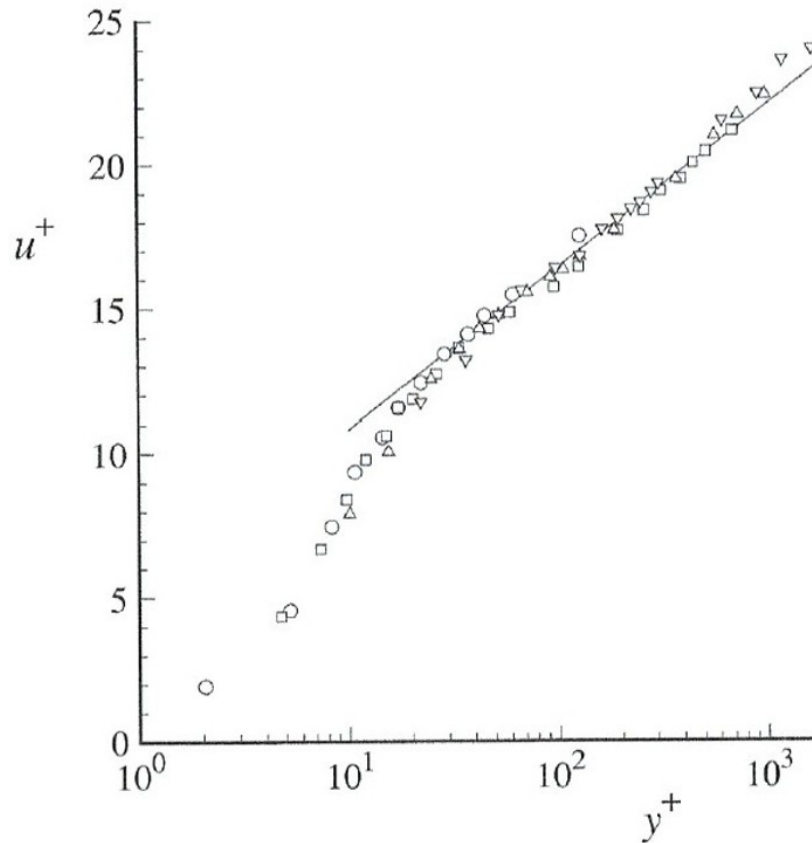


Figure I.8: The log law (line) plotted against different developed turbulent channel flow measures, taken from Pope [26].

With $\kappa_{th}^* \approx 0.38$ the thermal Von Karman constant, and B_{th} an experimentally determined constant. In this thesis, only adiabatic walls were considered.

I.3 Molten salt reactors physics

I.3.a The coupled neutronic–thermal-hydraulic problem

In the molten salt reactors considered in this thesis, the fuel salt is both the fuel and the coolant, so we must solve the neutronic problem and the thermal-hydraulic problem for the salt. The unknowns are the fuel velocity field \mathbf{u} — the modified pressure is replaced by its expression in Equation 1.21 — the fuel temperature field T , the precursor concentration fields C_i , and the neutron flux ψ from which we derive the thermal power density field P_{th} and the precursor source fields S_{C_i} . The coupled

problem can then be expressed as:

$$\left\{ \begin{array}{l} \frac{1}{|\mathbf{v}|} \frac{\partial \psi}{\partial t} = (-\mathcal{L}(T) + \mathcal{S}(T) + \mathcal{F}(T) + \mathcal{D}(T, C_i)) \psi \\ \frac{\partial \mathbf{u}}{\partial t} + \mathbf{u} \cdot \nabla \mathbf{u} = -\frac{1}{\rho} \nabla p + \nu \nabla^2 \mathbf{u} + S_m \\ \frac{\partial T}{\partial t} + \mathbf{u} \cdot \nabla T = \alpha \nabla^2 T + \frac{P_{th}(\psi)}{\rho c_p} \\ \frac{\partial C_i}{\partial t} + \mathbf{u} \cdot \nabla C_i = D_m \nabla^2 C_i - \lambda_i C_i + S_{C_i}(\psi) \end{array} \right. \quad (\text{I.37})$$

The neutron flux depends on the temperature and concentration fields, which in turn depend on the neutron flux. Furthermore, all the fields depend on the velocity field. In the case of a turbulent flow, all the unknowns are therefore turbulent.

I.3.b Transport of the delayed neutrons precursors

Even for a constant temperature field — so the temperature feedbacks can be neglected — the usual steady-state expression for the delayed fission operator (Equation I.7) cannot be derived here, because of the transport of the precursors. The steady-state Boltzmann equation is therefore different for an MSR. The steady-state precursor concentration equations are expressed as:

$$\lambda_i C_i = D_m \nabla^2 C_i - \mathbf{u} \cdot \nabla C_i + \beta_i \int_{E_{min}}^{E_{max}} \nu \Sigma_f \phi dE' \quad (\text{I.38})$$

Because of the advection and diffusion terms, the delayed and prompt fission operators cannot be combined into the \mathcal{F}_∞ operator. Delayed and prompt neutrons must be distinguished in the steady-state Boltzmann equation for MSRs:

$$\left(-\mathcal{L} + \mathcal{S} + \frac{1}{k_{eff}} \mathcal{F} \right) \psi + \frac{1}{k_{eff}} \sum_i \frac{\chi_{d,i}}{4\pi} \lambda_i C_i = 0 \quad (\text{I.39})$$

I.3.c Wall laws for MSRs

For MSRs simulations with non-adiabatic walls, the thermal wall laws established previously (Equations I.35 and I.36) must be modified. The boundary layer in an MSR presents large temperature gradients — due to the low thermal diffusivity — and the boundary layer is internally heated by the fission reactions in the salt. New thermal wall laws adapted to MSRs studies have been derived [49]. These new laws were not used in this thesis however, because only adiabatic walls were considered.

In this chapter, we presented the main phenomena and equations involved in nuclear reactor physics, both regarding neutronics and thermal-hydraulics; we also showed how these equations are coupled in the specific case of molten salt reactors. The objective of the next chapter is to present ways to numerically solve the coupled problem I.37.

Chapter II

Numerical resolution of the coupled problem

The purpose of this chapter is to present how to numerically solve the neutronic problem (the Boltzmann equation, see Section II.1) and the thermal-hydraulic problem (the Navier-Stokes equations as well as the energy and concentration equations, see Section II.2). Some multiphysics codes adapted for MSRs are then presented (Section II.3), with a focus on the APOLL03[®] – TrioCFD multiphysics code (Section II.4).

II.1	Numerical resolution of the Boltzmann equation	45
II.1.a	Discretisation of the steady-state Boltzmann equation	45
II.1.b	Lattice calculation and self-shielding	46
II.1.c	Core calculation	48
II.1.d	Discretisation of the time-dependant Boltzmann equation	49
II.1.e	Critical calculation for transient simulations	49
II.2	Numerical resolution of the Navier-Stokes equations	50
II.2.a	Time discretisation of the Navier-Stokes equations	50

II.2.b	Laminar flows	51
II.2.c	Direct Numerical Simulation (DNS)	51
II.2.d	Reynolds-Averaged Navier-Stokes (RANS) approach	52
II.2.e	Large Eddy Simulation (LES) approach	54
II.2.f	Flow near the wall	57
II.3	Multiphysics codes for MSRs simulations	57
II.3.a	The need for specific codes	57
II.3.b	Existing multiphysics codes adapted for MSRs	58
II.4	The APOLL03 [®] – TrioCFD multiphysics code	59
II.4.a	Presentation	59
II.4.b	Field exchanges	61
II.4.c	Steady-state calculation strategy	61
II.4.d	Transient calculation strategy	61
II.4.e	V&V roadmap of the APOLL03 [®] – TrioCFD code	62

II.1 Numerical resolution of the Boltzmann equation

II.1.a Discretisation of the steady-state Boltzmann equation

The steady-state Boltzmann Equation (I.10) is a first order linear integro-differential equation. In order to solve it numerically, we need to discretise the different variables: space, energy, and angle.

The space discretisation relies on a meshing of the physical domain, as well as a finite difference or finite element method. The spatial resolution is given by the neutron mean free path, which is the average distance a neutron travels before interacting with matter (typically 1 cm for a thermal-spectrum reactor, 10 cm for a fast-spectrum reactor).

Different methods exist for the angle discretisation: the main ones are the diffusion approximation (no angle dependency), the discretisation on a number of solid angles intervals (discrete ordinates method, also called S_N method), or the discretisation on a number of spherical harmonics (P_N and SP_N methods). While the SP_N method is an approximation, both the S_N and the P_N methods converge towards the analytical solution for N large enough [50]. For nuclear reactors simulations, the S_N method is usually preferred because it is easily parallelizable [50].

The energy discretisation is more complex. Because the cross sections for heavy nuclei present many resonances (see Figure I.2), a very fine energy mesh would be required to solve the transport equation. Such a fine mesh would be prohibitive for calculations on a whole nuclear reactor core — because of the inelastic scattering term in the Boltzmann equation, the different energy groups are not independent and therefore not easily parallelizable. For this reason, many deterministic neutronics codes, such as APOLL03[®], use a two-steps numerical scheme with two different calculations: the lattice calculation and the core calculation.

II.1.b Lattice calculation and self-shielding

The core calculation on the whole reactor core uses a rather coarse energy discretisation — in this thesis, from 6 to 33 energy intervals, called energy groups. This number of groups is not enough to represent the many resonances of heavy nuclei. A preliminary step is therefore needed to compute the averaged cross sections on each energy group, called the multigroup cross sections.

The goal of the so-called lattice calculation is to obtain the multigroup cross sections for the different materials composing the core. A very fine energy mesh is used (typically between 10^4 and 10^5 groups) on a small domain (typically one sector of the reactor, with symmetry boundary conditions). The steady-state Boltzmann equation is solved for this domain, which gives the neutron flux and the different reaction rates (the product of the different cross sections by the scalar neutron flux) in the different core materials. The multigroup cross sections are then determined so that the multigroup reaction rates are equal to the calculated reaction rates :

$$\sigma_{q,g} \phi_g = \int_g \sigma_q(E) \phi(E) dE \quad (\text{II.1})$$

With $\sigma_{q,g}$ the multigroup cross section for the reaction q and the energy group

g , ϕ_g the multigroup scalar flux for the group g , and σ_q and ϕ the continuous cross section and flux — during the lattice calculation, these are not continuous but finely discretised.

In addition to reducing the number of energy groups for the core calculation, the lattice calculation is usually also used to perform a homogenisation: the many different isotopes and elements composing a material like the fuel or the reflector, each having their own cross sections, are regrouped in one material with one set of cross sections. The homogenisation greatly reduces the size of the cross sections library to use in the core calculation: instead of dozens of different isotopes, only a handful of different materials are used to construct the core. Depending on the reactor studied, the homogenisation can vary: for a Pressurised Water Reactor for example, it is not unusual to homogenise together all the materials along the vertical axis into macro-materials called assemblies, so the whole core can be modelled as a 2D geometry of assemblies extruded along the vertical axis. In this thesis, such an axial homogenisation was tested on the Aircraft Reactor Experiment (see Section III.3).

The multigroup cross sections depend on the neutron flux and therefore on the whole core geometry and composition. For example, if we consider two different fuel assemblies, one near a control rod (a neutron absorbent), and another one further away, both assemblies will have different fission rates because the neutron flux in both assemblies is different — there will be fewer fissions in the assembly closer to the rod, because there will be fewer neutrons. Therefore, the multigroup cross sections for both assemblies will be different. This phenomenon is known as spatial self-shielding.

The same reasoning applies even for one element: a high cross section, typically at a resonance, will result in a lower neutron flux at this resonance, so the reaction rate spectrum (which is the product of the cross section by the flux) will be flatter than the cross section spectrum (Figure II.1). This phenomenon is known as energy self-shielding.

Self-shielding is the reason why multigroup cross sections cannot be computed "once and for all" for every nucleus: they vary with every core geometry and composition. During the lattice calculation, choices must be made regarding the final number of energy groups (the number of groups used in the core calculation), and the number of assemblies considered (should the fuel assembly near the rod and the one further from it be differentiated?).

Usually, the temperature dependency of the cross sections — through both the Doppler effect and the density variation of the material — is also computed during

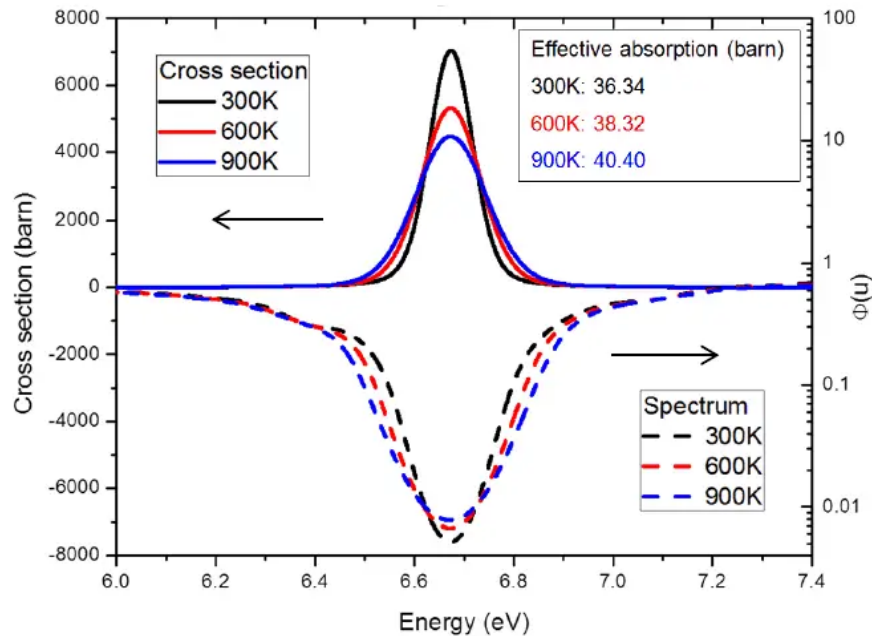


Figure II.1: Absorption cross section and neutron spectrum at the 6.67eV resonance of ^{235}U .

this step, so that the output of the lattice calculation is a library of self-shielded, multigroup, temperature-parametrized macroscopic cross sections for every reaction and every assembly/material composing the core. It is important to note that these sections depend not only on their own assembly temperature, but every assembly temperatures, because of the spatial self-shielding.

II.1.c Core calculation

During the core calculation, the whole reactor core geometry is numerically constructed, using the different materials or assemblies from the lattice calculation as the elementary bricks of this construction. The steady-state Boltzmann equation (Equation I.10) can then be solved. An iterative numerical scheme is used: starting with a uniform neutron flux, Equation I.10 is solved, the new neutron flux stored and the eigenvalue k_{eff} taken as the ratio of the new flux amplitude to the previous flux amplitude. The process is repeated until convergence of both the flux and the eigenvalue. At the end of each step, the neutron flux amplitude is also normalised by the imposed total power.

II.1.d Discretisation of the time-dependant Boltzmann equation

For transient calculations, we must solve the time-dependent Boltzmann equation (Equation I.4) and the precursor concentration evolution equations (Equation I.6). The space, angle and energy discretisations are the same as for the steady-state case. For a solid-fuel reactor, the precursor equations can be integrated and injected in the transport equation:

$$C_i(t, \mathbf{r}) = e^{-\lambda_i(t-t_0)} C_{0,i}(t, \mathbf{r}) + \beta_i \int_{t_0}^t e^{-\lambda_i(t-t')} \int_{E_{min}}^{E_{max}} \nu \Sigma_f \phi dE' dt' \quad (\text{II.2})$$

For the time discretisation, in this thesis, a finite difference method with an implicit first-order scheme was used (Euler backward scheme). The use of an implicit scheme allows for a rather coarse temporal resolution (around 10^{-2} s) instead of the typical lifetime of a prompt neutron (10^{-6} s). The quasi-static approach, where the distribution of the neutron flux is assumed constant and only its total amplitude varies, cannot be used in this thesis because we want to represent the neutron flux distribution distortions linked to turbulence.

II.1.e Critical calculation for transient simulations

Usually, a steady-state simulation is performed before a transient simulation, in order to determine the initial state of the transient. However, the k_{eff} value obtained during a steady-state calculation will never be exactly 1. If we start a transient calculation with a k_{eff} value different from 1, even with no perturbation from the initial state, the unknowns will evolve.

In order to ensure that the initial state is a steady state, a critical calculation needs to be performed first. It is simply a succession of steady-state calculations, but between each step, the total neutron multiplicity ν is divided by k_{eff} , effectively adjusting the computed neutron flux towards a perfectly steady flux. The iterations are stopped when $1 - k_{eff}$ falls below an imposed threshold — typically 10^{-6} . While this operation makes no physical sense — the neutron multiplicity is not an adjustable parameter in a nuclear reactor — it is a convenient mathematical operation necessary to initiate transient calculations "properly".

II.2 Numerical resolution of the Navier-Stokes equations

The numerical resolution of the Navier-Stokes equations is the purpose of Computational Fluid Dynamics (CFD). Compared to the discretisation of the Boltzmann equation, the discretisation of the Navier-Stokes equations is more straightforward: the space discretisation relies on a meshing of the physical domain, as well as a finite difference or finite element method. The time discretisation relies on a finite difference method, with either implicit or explicit schemes.

II.2.a Time discretisation of the Navier-Stokes equations

When using a first-order explicit time scheme to solve the Navier-Stokes equations, the highest stable timestep must be determined. This timestep is not the same for the convection part of the Navier-Stokes equations (the $\mathbf{u} \cdot \nabla \mathbf{u}$ term) and the diffusion part (the $\nu \nabla^2 \mathbf{u}$ term). The convective stable timestep on one cell is given by the Courant-Friedrichs-Lewy (CFL) condition:

$$\Delta t_{max,conv} = \min \left(\frac{d_i}{u_i} \right) \quad (\text{II.3})$$

With d_i and u_i the length of a cell and the fluid velocity in the i -th direction. This condition must be verified for all cells of the mesh, so the actual convective stable timestep is the lowest among all cells.

The diffusive stable timestep however, follows a second-order law:

$$\Delta t_{max,diff}^{NS} = \frac{\min(d_i)^2}{2\nu} \quad (\text{II.4})$$

It should also be noted that for the temperature and concentration equations, while the convective timestep remains the same, the diffusive timestep does not:

$$\Delta t_{max,diff}^{th} = \frac{\min(d_i)^2}{2\alpha} = P_R \Delta t_{max,diff}^{NS} \quad (\text{II.5})$$

$$\Delta t_{max,diff}^{conc} = \frac{\min(d_i)^2}{2D_m} = S_C \Delta t_{max,diff}^{NS}$$

With $P_R = \nu/\alpha$ the Prandtl number, and $S_C = \nu/D_m$ the Schmidt number.

Depending on which equations are solved in the problem, the stable diffusive timestep is the minimum of the different diffusive timesteps.

In this thesis, the same timestep was used for both the convection and the diffusion term, so the highest stable timestep is the minimum on every cells of the two timesteps:

$$\Delta t_{max} = \min(\Delta t_{max,diff}, \Delta t_{max,conv}) \quad (\text{II.6})$$

When using an N-order explicit time scheme, the stable timestep is N times as high as the first-order stable timestep. However, higher order time schemes require more memory, as more unknowns need to be kept between two timesteps. The use of an implicit time scheme also enables dynamic, higher timesteps to be used, once again at the cost of memory use.

II.2.b Laminar flows

For a laminar flow, the Navier-Stokes equations can simply be discretised and solved without extra steps. The spatial resolution is obtained through a mesh convergence study: gradually finer meshes are used, until the simulation results do not vary between two meshes. The temporal resolution depends on the type and order of the time scheme used, as described above.

II.2.c Direct Numerical Simulation (DNS)

For a turbulent flow, the most intuitive resolution is the same as for a laminar flow. In the case of a turbulent flow however, the spatial resolution is known: all eddies lengthscales must be solved until the dissipation range, so the mesh size is given by the Kolmogorov lengthscale η (see Section I.2.c). The temporal resolution is given by Equation II.6 for an explicit scheme, which imposes a very small timestep because the mesh size is very small. We can see that the computation time of such a method, known as Direct Numerical Simulation (DNS), grows very rapidly with the Reynolds number:

$$\begin{aligned} \text{Computation Time} &\propto (\Delta t)^{-1} N_{cells} \\ &\propto \eta^{-1} \eta^{-3} \\ &\propto \text{Re}^{3/4} \text{Re}^{9/4} \\ &\propto \text{Re}^3 \end{aligned} \quad (\text{II.7})$$

With N_{cells} the total number of cells, inversely proportional to the volume of a cell, and Δt the timestep, proportional to the minimum length of a cell — we consider only the convective timestep, the diffusion can be solved with an implicit scheme. A more rigorous demonstration of the computation time for DNS can be found in Pope [26].

DNS is the most precise simulation method — the Navier-Stokes equations are solved without approximations — but its high computation time requires either a large amount of computational resources, or to restrict its use to small domains and low Reynolds numbers. For other cases, approximations of the Navier-Stokes equations must be made.

II.2.d Reynolds-Averaged Navier-Stokes (RANS) approach

A common method for turbulent flow simulations is to decompose the velocity field into a mean value and a random value:

$$\mathbf{u} = \bar{\mathbf{u}} + \mathbf{u}^* \tag{II.8}$$

Only the mean velocity field $\bar{\mathbf{u}}$ is solved, and not the random component \mathbf{u}^* . This method, known as Reynolds-Averaged Navier-Stokes (RANS), does not represent the eddies in a turbulent flow. The RANS equations are the Navier-Stokes equations for the mean field:

$$\nabla \cdot \bar{\mathbf{u}} = 0 \tag{II.9}$$

$$\frac{\partial \bar{\mathbf{u}}}{\partial t} + \bar{\mathbf{u}} \cdot \nabla \bar{\mathbf{u}} = -\frac{1}{\rho} \nabla p + \nu \nabla^2 \bar{\mathbf{u}} - \nabla \tau + S_m$$

We can see that Equation II.9 is very similar to Equation I.20. The difficulty comes from the Reynolds stress tensor τ which contains the unknown random velocity:

$$\tau_{ij} = \overline{u_i^* u_j^*} \tag{II.10}$$

The Reynolds stress tensor also intervenes in the modified pressure equation:

$$\nabla^2 p = -\rho(\nabla^2 \bar{\mathbf{u}} + \nabla \tau) \tag{II.11}$$

We need an equation for this tensor in order to close the problem. One of the

most common hypotheses is the Boussinesq hypothesis, which links the stress tensor to the mean velocity gradient:

$$\tau_{ij} = \overline{u_i^* u_j^*} = \frac{2}{3} k \delta_{ij} - \nu_t \left(\frac{\partial \overline{u_i}}{\partial x_j} + \frac{\partial \overline{u_j}}{\partial x_i} \right) \quad (\text{II.12})$$

With k the turbulent kinetic energy and ν_t the turbulent viscosity, to be determined. We see that the Boussinesq hypothesis is similar to the Newtonian fluid hypothesis (Equation I.17). There are other expressions for the Reynolds stress tensor, used in Reynolds stress methods, which will not be presented here.

With the Boussinesq hypothesis, the RANS momentum equation can be expressed as:

$$\frac{\partial \overline{\mathbf{u}}}{\partial t} + \overline{\mathbf{u}} \cdot \nabla \overline{\mathbf{u}} = -\frac{1}{\rho} \nabla \left(p + \frac{2}{3} \rho k \right) + \nabla \cdot [(\nu + \nu_t) \nabla \overline{\mathbf{u}}] + S_m \quad (\text{II.13})$$

We still need an equation for the turbulent kinetic energy k and the turbulent viscosity ν_t . Many methods exist, we present here the classical $k - \epsilon$ method [51] (the main method used in this thesis), which considers a third unknown, the turbulent dissipation rate ϵ , and links the three unknowns to the velocity through the following equations:

$$\left\{ \begin{array}{l} \frac{\partial k}{\partial t} + \overline{\mathbf{u}} \cdot \nabla k = \nabla \cdot \left[\left(\nu + \frac{\nu_t}{\sigma_k} \right) \nabla k \right] - \epsilon + P_k + P_b \\ \frac{\partial \epsilon}{\partial t} + \overline{\mathbf{u}} \cdot \nabla \epsilon = \nabla \cdot \left[\left(\nu + \frac{\nu_t}{\sigma_\epsilon} \right) \nabla \epsilon \right] + C_{\epsilon 1} P_k \frac{\epsilon}{k} - C_{\epsilon 2} \frac{\epsilon^2}{k} + C_{\epsilon 3} C_{\epsilon 1} P_b \frac{\epsilon}{k} \\ \nu_t = C_\mu \frac{k^2}{\epsilon} \\ P_k = -\tau_{ij} \frac{\partial \overline{u_i}}{\partial x_j} \\ P_b = \frac{\nu_t}{P_{Rt}} \beta_{th} \mathbf{g} \nabla T \end{array} \right. \quad (\text{II.14})$$

Einstein notation is used for clarity. P_k is calculated using Equation II.12. P_b is

the source of turbulent kinetic energy from buoyancy, with \mathbf{g} the gravity acceleration, β_{th} the thermal expansion coefficient, and P_{Rt} the turbulent Prandtl number. The other free parameters $C_\mu = 0.09$, $C_{\epsilon 1} = 1.44$, $C_{\epsilon 2} = 1.92$, $\sigma_k = 1$ and $\sigma_\epsilon = 1.3$ are experimentally determined constants. For the energy and concentration equations, the turbulence is modelled by introducing an eddy diffusion coefficient — the eddies in the flow act as a "turbulent diffusion":

$$\begin{aligned} \frac{\partial T}{\partial t} + \bar{\mathbf{u}} \cdot \nabla T &= \nabla \cdot \left[\left(\alpha + \frac{\nu_t}{P_{Rt}} \right) \nabla T \right] + S_{th} \\ \frac{\partial C}{\partial t} + \bar{\mathbf{u}} \cdot \nabla C &= \nabla \cdot \left[\left(D_m + \frac{\nu_t}{S_{Ct}} \right) \nabla C \right] + S_C \end{aligned} \tag{II.15}$$

With P_{Rt} the turbulent Prandtl number, varying between 0.7 and 0.9, depending on the fluid; S_{Ct} the turbulent Schmidt number, varying between 0.2 and 6.

The spatial resolution for RANS studies is obtained through mesh convergence studies. The temporal resolution is given by Equation II.6 for an explicit scheme.

II.2.e Large Eddy Simulation (LES) approach

If we need to directly represent the eddies in the flow, a RANS approach is not possible. For large domains or large Reynolds numbers, where DNS is prohibitive, the most common approach is the Large Eddy Simulation (LES). The velocity field is once again decomposed into two parts, but this time into a filtered component and a residual one:

$$\mathbf{u} = \tilde{\mathbf{u}} + \mathbf{u}' \tag{II.16}$$

Only the filtered velocity field $\tilde{\mathbf{u}}$ is solved, and not the residual component \mathbf{u}' . The idea behind the LES approach is to explicitly compute the large-scale eddies in the energy-containing and transitional ranges, and to model the smaller eddies in the dissipation range, which are assumed to be flow-independent. The LES equations are the Navier-Stokes equations for the filtered field:

$$\nabla \cdot \tilde{\mathbf{u}} = 0 \tag{II.17}$$

$$\frac{\partial \tilde{\mathbf{u}}}{\partial t} + \tilde{\mathbf{u}} \cdot \nabla \tilde{\mathbf{u}} = -\frac{1}{\rho} \nabla p + \nu \nabla^2 \tilde{\mathbf{u}} - \nabla \tilde{\tau} + S_m$$

Which are similar to the RANS equations [II.9](#).

The stress tensor, called the sub-grid-scale stress tensor, is defined as:

$$\tilde{\tau}_{ij} = \widetilde{u_i u_j} - \tilde{u}_i \tilde{u}_j \tag{II.18}$$

Which is rewritten with the Boussinesq hypothesis as:

$$\tilde{\tau}_{ij} = \frac{1}{3} \tilde{\tau}_{kk} \delta_{ij} - \nu_{SGS} \left(\frac{\partial \tilde{u}_i}{\partial x_j} + \frac{\partial \tilde{u}_j}{\partial x_i} \right) \tag{II.19}$$

With ν_{SGS} the sub-grid-scale viscosity, to be determined. The trace of the tensor is included in the modified pressure term. With the Boussinesq hypothesis, the LES momentum equation can be expressed as:

$$\frac{\partial \tilde{\mathbf{u}}}{\partial t} + \tilde{\mathbf{u}} \cdot \nabla \tilde{\mathbf{u}} = -\frac{1}{\rho} \nabla \tilde{p} + \nabla \cdot [(\nu + \nu_{SGS}) \nabla \tilde{\mathbf{u}}] + S_m \tag{II.20}$$

$$\tilde{p} = p + \frac{1}{3} \rho \sum_k \tilde{\tau}_{kk}$$

Which is once again similar to the RANS momentum equation [II.13](#). The modified pressure \tilde{p} is solved as usual, by taking the divergence of the momentum equation (see [Section 1.2.b](#)). We still need an equation for the sub-grid-scale viscosity ν_{SGS} . The historical model by Smagorinsky [\[52\]](#) is not presented here, but rather the more recent Wall Adaptive Local Eddy-viscosity (WALE) model [\[53\]](#), which was used in this thesis:

$$\nu_{SGS} = (C_w \Delta)^2 \frac{(s_{ij}^d s_{ij}^d)^{3/2}}{(S_{ij} S_{ij})^{5/2} + (s_{ij}^d s_{ij}^d)^{5/4}}$$

$$S_{ij} = \frac{1}{2} \left(\frac{\partial \tilde{u}_i}{\partial x_j} + \frac{\partial \tilde{u}_j}{\partial x_i} \right) \quad (\text{II.21})$$

$$s_{ij}^d = \frac{1}{2} \left[\left(\frac{\partial \tilde{u}_i}{\partial x_j} \right)^2 + \left(\frac{\partial \tilde{u}_j}{\partial x_i} \right)^2 \right] - \frac{1}{3} \left(\frac{\partial \tilde{u}_k}{\partial x_k} \right)^2 \delta_{ij}$$

With Δ the sub-grid-scale typical lengthscale, and C_w a constant experimentally determined at 0.5. Einstein notation is used for clarity.

For the energy and concentration equations, they are the same as in the RANS approach (Equation II.15), but with the sub-grid-scale viscosity rather than the turbulent viscosity.

We can observe that the filtering operation applied on the velocity field does not appear in the LES equation nor in the sub-grid-scale equations. It is because the filtering is implicit: choosing a mesh resolution and solving the LES equation and the sub-grid-scale equations on this mesh is equivalent to applying a low-pass filter on the exact velocity field — given by a DNS simulation for example.

The mesh size is inversely proportional to the implicit filter width. Mesh convergence studies are therefore not possible for LES simulations: refining the mesh leads to more resolved wavelengths, until all the eddies wavelengths are simulated and the mesh size is the Kolmogorov lengthscale, which means we are performing a DNS simulation.

The criterion for the spatial convergence is rather based on the turbulent energy spectrum: the large and intermediate eddies must be resolved in LES, which corresponds to approximately 80% of the total turbulent energy. We thus define the Large Eddy Simulation Index of Quality (LES_IQ) [54] as the ratio of the resolved turbulent kinetic energy to the total turbulent kinetic energy, which must be over 0.8 in every cell:

$$\text{LES_IQ} = \frac{k_{res}}{k_{res} + k_{SGS}} > 0.8 \quad (\text{II.22})$$

However, the LES_IQ can only be computed after the calculation, as a validation criterion. Different indicators exist to estimate the meshing spatial resolution before the calculation. One of them is the transverse Taylor microscale, which can be computed

during a RANS calculation with the following approximation:

$$\lambda_T \approx \sqrt{10\nu \frac{k}{\epsilon}} \quad (\text{II.23})$$

The temporal resolution for LES is given by Equation II.6 for an explicit scheme.

II.2.f Flow near the wall

If we want to explicitly compute the flow near the wall, a very fine mesh is required in the inner layer, as the velocity varies very rapidly near the wall. We typically want to have $y^+ \sim 1$ in the first cell, and to gradually increase the cell size in the inner layer, which can be impactful on the total number of cells and on the simulation timestep.

Another possibility is to use wall laws (section I.2.f). For example, we can ensure that $30 < y^+ < 300$ in the first cell, and apply the log law. This allows the use of non-refined meshes, but it introduces an approximation in the model, as these laws have been determined for channel flows with a flow parallel to the wall, and not any flow.

For Large Eddy Simulations, we usually differentiate wall-resolved LES and LES with near-wall modelling (LES-NWM). In this thesis, the Reichardt law (Equation I.34) was used for both RANS and LES calculations, which is valid for $y^+ < 300$.

II.3 Multiphysics codes for MSRs simulations

II.3.a The need for specific codes

Molten salt reactor studies require the development of specific codes. If the strong coupling between neutronics and thermal-hydraulics requires to couple a neutronic code with a thermal-hydraulic code, developments are also needed to model the precursor transport with the flow, and to adapt the steady-state Boltzmann equation (see Equation I.39).

Another reason for the development of new numerical tools is the geometry of recent MSRs designs, where a free, flow-optimised volume replaces the square or hexagonal lattice of assemblies composing most of current reactors. These new, non-extruded geometries often require the use of unstructured meshes, which are not always supported by existing codes.

Different codes have thus been developed for MSRs studies. We present some of them that use CFD for the thermal-hydraulic model.

II.3.b Existing multiphysics codes adapted for MSRs

The first multiphysics code using CFD to be developed for MSRs studies was the TFM-OpenFOAM code, developed within CNRS in 2015 [55]. The open-source CFD code OpenFOAM [56] is used to compute the velocity, temperature, and precursor concentration fields; the Monte-Carlo neutronic code MCNP [57] is then used to solve the neutron flux and power distribution; external iterations are performed until all the unknowns converge.

Because Monte-Carlo calculations have an important computation time, another approach has been developed for transient simulations and reduced computation time using transient fission matrices (TFM) [55, 58]. Deterministic methods, with diffusion and SP_N angular discretisations, have also been developed in OpenFOAM [59].

The CNRS code has been used for steady-state and transient simulations on the Molten Salt Fast Reactor (MSFR) design [55, 60] — as well as steady-state simulations on Pressurized Water Reactors [55]. A numerical benchmark for MSRs codes has also been created, in order to compare different multiphysics codes on a two-dimensional fuel salt square [55, 61]. The TFM-OpenFOAM code has also been used on fast sodium reactors and compared with deterministic neutronic codes [62]. More recently, this code has also been used on the MSFR with a Detached Eddy Simulation (DES, mixing LES where the mesh is fine enough and RANS elsewhere [63]) approach for design optimization [64].

A multiphysics code called GeN-Foam and based on OpenFOAM has been developed at Paul Scherrer Institute in 2015 [65]. The code combines the CFD libraries of OpenFOAM and a deterministic diffusion neutronic solver. It has been verified on the numerical benchmark [59].

A two-phases solver using OpenFOAM for thermal-hydraulics and neutronics (diffusion and SP_N angular discretisations) has been developed at Politecnico di Milano in 2017 [66]. It has been verified on the numerical benchmark [59], and compressible steady-state simulations on the MSFR have been performed [67]. The two-phases solver also enabled the modelling of a bubbling system in the MSFR to remove gaseous fission products, and the study of its impact on the density feedback [68].

A multiphysics code combining the CFD solver DGFlores and the deterministic neutronic code PHANTOM- S_N has been developed at Delft University of Technology in

2019 [69, 70]. It has been verified on the numerical benchmark [59], and was the first to use an S_N angular discretisation. Steady-state and transient simulations on the MSFR have been realised [69].

Recently, a coupling between the Monte Carlo transport code `OpenMC` and the CFD code `NekRS` through the `MOOSE` coupling application has been designed in Argonne National Laboratory [71]. This multiphysics tool has been used to perform coupled simulations on the MSFR with a spectral LES approach [71, 72].

The previously mentioned studies — except the most recent works [64, 71] — used a RANS approach for the thermal-hydraulic model. RANS simulations require a coarser mesh and a larger timestep than LES. Furthermore, for a symmetric domain, since the mean fields are also symmetric, only a fraction of the whole core can be modelled, with symmetric or periodic boundary conditions. RANS simulations are therefore much more "economical" than LES calculations. Unfortunately, RANS calculations do not show the eddies in the core, so the analysis of turbulent fluctuations of the power distribution, neutron flux, and temperature field is not possible with RANS simulations.

In CEA, since 2018, different multiphysics codes are developed for MSRs simulations: for core simulations, two system codes for transient analysis, called `MOSAICS` and `COCCINELLE`, were developed in collaboration with CNRS from 2019 to 2022 [73]. Recently, a diffusion neutronic solver called `TRUST-NK` was added to the CFD platform `TRUST/TrioCFD`, and should be used to perform simulations on MSRs — it is currently under development. The CEA reference code, which is used for detailed simulations of MSRs cores, is the `APOLL03® - TrioCFD` multiphysics code — used in this thesis.

II.4 The `APOLL03® - TrioCFD` multiphysics code

II.4.a Presentation

The high-fidelity multiphysics code for MSRs studies in CEA is based on two existing codes, developed within CEA: the deterministic neutronic code `APOLL03®` [21], and the CFD platform `TRUST/TrioCFD` [22]. This code must be able to perform reference calculations for MSRs cores, using the most precise numerical methods available. `TRUST/TrioCFD` performs turbulent simulations with either RANS, LES, or DNS approaches. `APOLL03®` possesses different solvers for different angular discretisations, notably `MINARET` for S_N discretisation.

The coupling strategy of the APOLLO3[®] – TrioCFD code is presented in Figure II.2: preliminary steps include the creation of a geometry and a mesh for the neutronic problem and the thermal-hydraulic problem, and a lattice calculation to compute the self-shielded, temperature-parametrised, macroscopic cross sections for the different materials composing the core. APOLLO3[®] is usually the first code to run in a coupled simulation; it computes the neutron flux, the power density field and the precursor source fields for an initial homogeneous temperature and null precursor concentrations. The power density field and the precursor source fields are sent to TrioCFD, which computes the velocity and pressure fields, the temperature field and the precursor concentration fields. The temperatures are then sent to APOLLO3[®] to update the macroscopic cross sections, and the precursor concentration fields are used as a source term for the Boltzmann equation.

In APOLLO3[®] – TrioCFD, the precursor concentration equations are solved by the thermal-hydraulic solver, contrary to most other coupled codes where the velocity field is sent to the neutronic code in order to solve the concentration equation. This is because the concentration equation is already available and parallelizable in TrioCFD, so no further development is required.

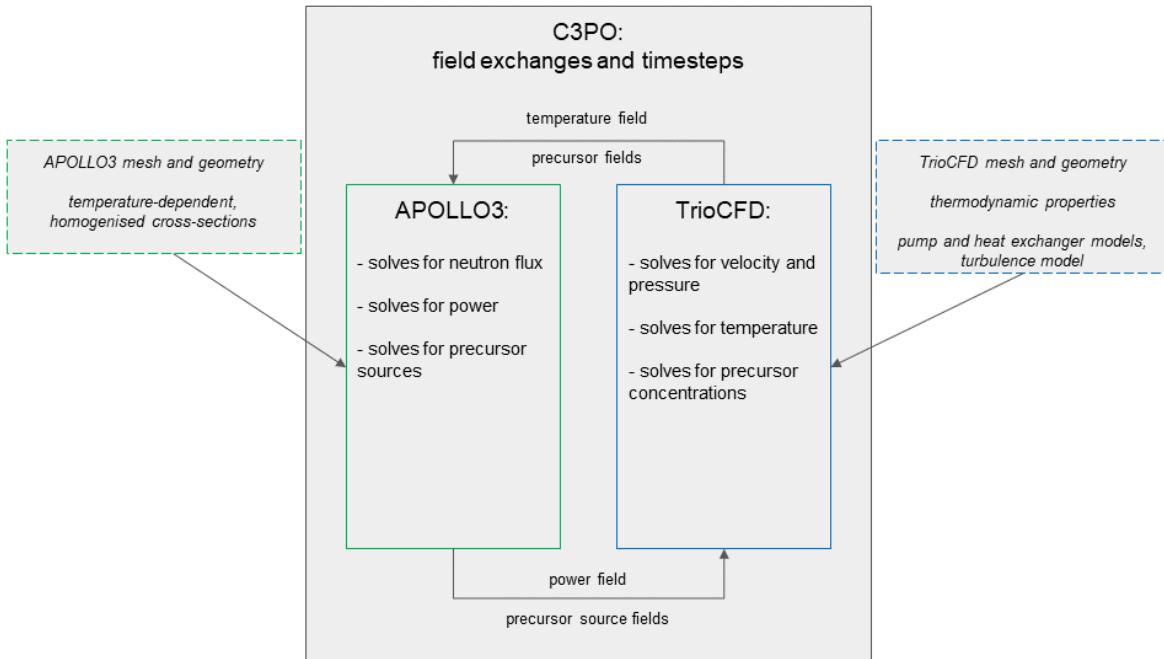


Figure II.2: The APOLLO3[®] – TrioCFD coupling strategy.

II.4.b Field exchanges

The meshes for each code are usually different, so the field exchanges and remappings are handled by a python library called C3PO [74], developed within CEA, which uses the MEDCoupling library [75]. Projections methods from MEDCoupling are used to exchange the different P0 (unknowns at the center of the cell), intensive fields between the two non-overlapping meshes. The maximum principle is favored over conservativity for the temperature fields, while the conservativity is favored for the power density, precursor concentration and precursor source fields.

II.4.c Steady-state calculation strategy

For steady-state calculations, APOLL03[®] solves the steady-state Boltzmann equation for MSRs (Equation I.39) with fixed, arbitrary temperature and precursor concentration fields. Once the neutronic unknowns (neutron flux, k_{eff} , power distribution and precursor source fields) have converged, power and precursor source fields are sent to TrioCFD. Depending on the turbulence modelling, TrioCFD solves the time-dependant velocity, pressure, temperature and concentration equations in either the RANS or LES formalism. For RANS calculations, fields convergence can be achieved, and for LES the convergence is assessed on the mean fields — since the instantaneous fields fluctuate. The temperature and precursor concentration fields are then sent to APOLL03[®]. This loop is repeated until the exchanged fields relative difference between two iterations fall below a threshold value. This method is known as the Gauss-Seidel method, and can be resumed by the following equation:

$$\begin{cases} \psi^{N+1}, k_{eff}^{N+1}, P_{th}^{N+1}, S_{C_i}^{N+1} = \mathcal{N}(T^N, C_i^N) \\ \mathbf{u}^{N+1}, p^{N+1}, T^{N+1}, C_i^{N+1} = \mathcal{TH}(P_{th}^{N+1}, S_{C_i}^{N+1}) \end{cases} \quad (\text{II.24})$$

With \mathcal{N} the neutronic operator, that regroups all the different neutronic equations, and \mathcal{TH} the thermal-hydraulic operator.

II.4.d Transient calculation strategy

For transient calculations, an explicit scheme is used. The thermal-hydraulic scheme is the same, because the steady-state calculation is already time-dependent. Instead of a convergence assessment however, a total duration before exchange of the

fields between both codes Δt_{exch} is imposed (typically 10^{-2} s). This duration is usually larger than the stable thermal-hydraulic timestep Δt_{TH} , so several timesteps are actually performed before the exchange. The thermal-hydraulic fields are then sent to APOLL03[®], which solves the time-dependent transport equation (Equation I.4) for the same duration Δt_{exch} , but using the "future" thermal-hydraulic fields. Just like for the thermal-hydraulic calculation, if the duration before exchange is longer than the neutronic timestep Δt_N , several timesteps are performed before exchange. The neutronic fields are then sent to TrioCFD, which resumes its calculation with the updated neutronic fields. This loop is performed until both codes reach the total transient simulation $T_{transient}$. A diagram of the transient scheme can be seen in Figure II.3. An explicit scheme is stable and accurate, provided that the Δt_{exch} duration is small enough [76].

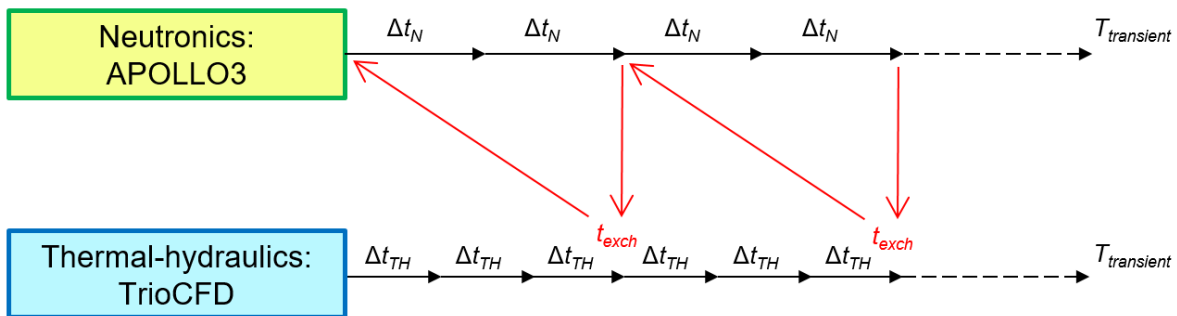


Figure II.3: Transient calculation numerical scheme.

II.4.e V&V roadmap of the APOLL03[®] – TrioCFD code

The APOLL03[®] – TrioCFD code is a new, still in development, tool. A Verification and Validation (V&V) roadmap for the code has thus been elaborated as follows:

- A verification step, where the APOLL03[®] – TrioCFD code is used on the CNRS numerical benchmark for MSRs codes. This step has been passed, details can be found in Greiner and al. [77].
- A validation step, where the APOLL03[®] – TrioCFD code is used to reproduce experimental data obtained on the historical Aircraft Reactor Experiment, the first-ever MSR (see Chapter III).

After these two steps, the APOLL03[®] – TrioCFD code is finally used to model the Molten Salt Fast Reactor (MSFR), in order to study the turbulent fluctuations in the core (see Chapter IV).

In this chapter, we presented the methods used to numerically solve the neutronic and thermal-hydraulic equations; we also showed how these methods are modified for MSRs simulations. Some existing multiphysics codes have been presented, with a focus on the APOLL03[®] – TrioCFD code used in this thesis. The objective of the next chapter is to present the validation step of the APOLL03[®] – TrioCFD code on the Aircraft Reactor Experiment.

Chapter III

Validation of the APOLL03[®] – TrioCFD code on a historical MSR: the Aircraft Reactor Experiment

The purpose of this chapter is the validation of the APOLL03[®] – TrioCFD code on the Aircraft Reactor Experiment (ARE), presented in Section III.1. A thermal-hydraulics model of the ARE was created in TrioCFD (Section III.2), as well as a neutronic model in APOLL03[®] (Section III.3). A steady-state simulation was performed in order to reproduce the ARE nominal state (Section III.4). Experiments realised on the ARE were then selected and reproduced on the numerical model: the variation of β_{eff} with the fuel flow (Section III.5), the insertion of a dollar of reactivity (Section III.6), and the variation of the extracted power (Section III.7).

Some early results on the ARE modelling led to a conference paper [78], and a journal paper (soon-to-be-published) [79].

III.1 The Aircraft Reactor Experiment	65
III.2 Thermal-hydraulic model of the ARE	68

III.2.a Geometries and meshing	68
III.2.b Resolved equations	69
III.2.c Physical properties	70
III.2.d Boundary conditions	72
III.2.e Source terms	72
III.3 Neutronic model of the ARE	72
III.3.a Lattice calculation	72
III.3.b Determining the materials' compositions	74
III.3.c Core calculation	75
III.4 Steady-state simulation: the ARE nominal state	77
III.5 Variation of β_{eff} with the fuel flow rate	79
III.6 Transient simulation: insertion of a dollar of reactivity	81
III.6.a The actual experiment	81
III.6.b First test run: instantaneous reactivity insertion	81
III.6.c Progressive reactivity insertion by diluting the rod	83
III.6.d Progressive reactivity insertion with a varying inlet temperature	86
III.7 Transient simulation: variation of extracted power	87
III.7.a The actual experiment	87
III.7.b The simulated experiment	89

III.1 The Aircraft Reactor Experiment

In order to validate the APOLL03[®] – TrioCFD code on an existing reactor, two choices are available: the Aircraft Reactor Experiment (ARE) or the Molten Salt Reac-

tor Experiment (MSRE). The ARE was chosen for its smaller size — which will speed up the calculations — and the many experiments realized on it and documented in detailed operation reports [4, 80, 81].

The ARE was built at Oak Ridge National Laboratory in 1954. The initial goal of the project, the Aircraft Nuclear Propulsion project, was to build a nuclear-propelled aircraft, so the compactness and excellent load-following capability of a molten salt reactor made it a natural candidate. The ARE went critical in November 1954, and functioned for 221 hours before final shutdown. Its purpose was to demonstrate the feasibility of such a reactor, as well as to measure the feedback coefficients and the load-following capability of an MSR.

The ARE core is contained in a metallic cylinder (120 cm in diameter and height). This cylinder is filled with hexagonal prisms made of beryllium oxide (Figure III.2). These BeO blocks act as the neutron moderator. The blocks in the center of the core have a 3.175 cm diameter circular hole in their center, and inconel tubes are inserted in these holes. The fuel salt flows from the top to the bottom of the core within the inconel tubes. The salt flow is divided into six parallel circuits, each of which passes 11 times through the core in a serpentine pattern, for a total of 66 fuel assemblies in parallel (Figure III.3). The six circuits then merge in the bottom salt collector, and the salt is cooled via two fuel-to-helium heat exchangers before returning to the core (Figure III.1).

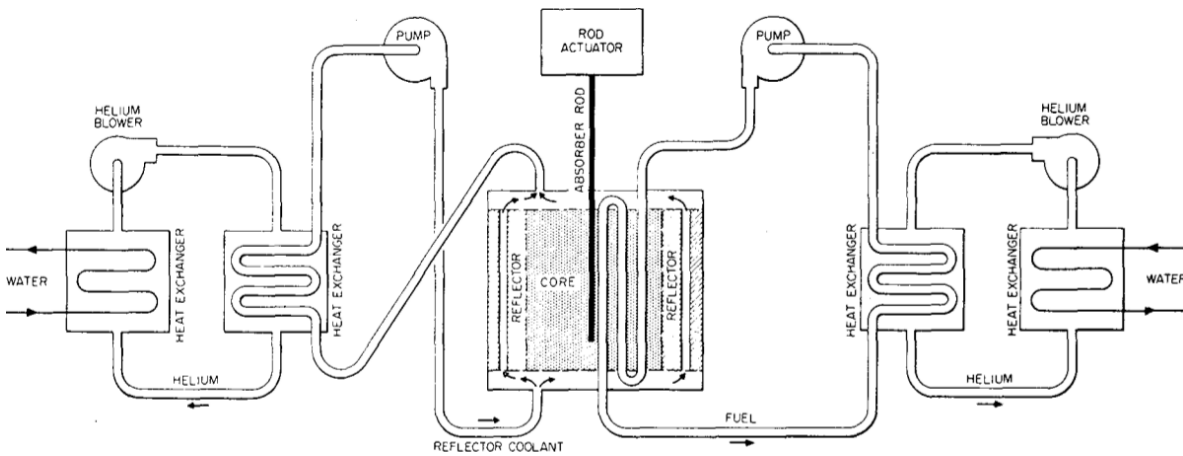


Figure III.1: Schematic diagram of the ARE [4].

The BeO blocks on the outer rings of the core have a 1.27 cm diameter circular hole, through which liquid sodium flows. The sodium acts as the moderator coolant. It flows from the bottom to the top of the core through the outer holes and the BeO

porosities, and is then cooled via two sodium-to-helium heat exchangers (Figure III.1).

The fuel salt is a $\text{NaF} - \text{ZrF}_4 - \text{UF}_4$ mixture (53% – 41% – 6% mol). The uranium is 93.4% enriched in ^{235}U .

Four rods are present, one regulating rod (stainless steel) and three shim rods (B_4C) that offset the initial reactivity excess and allow for an emergency shutdown (Figure III.1). Two instrumentation assemblies are also present near the outer edge of the core.

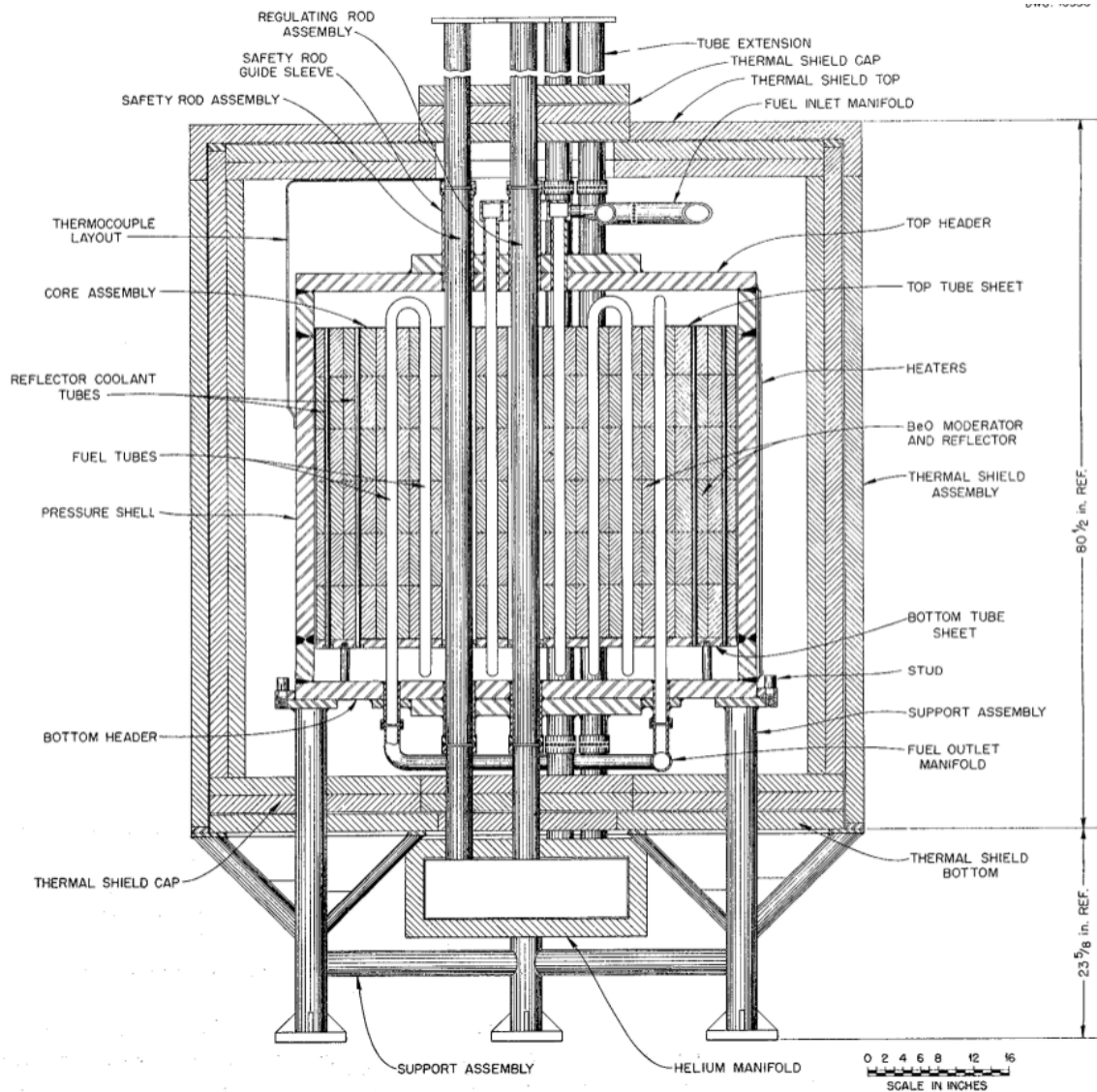


Figure III.2: Elevation section of the ARE core [4].

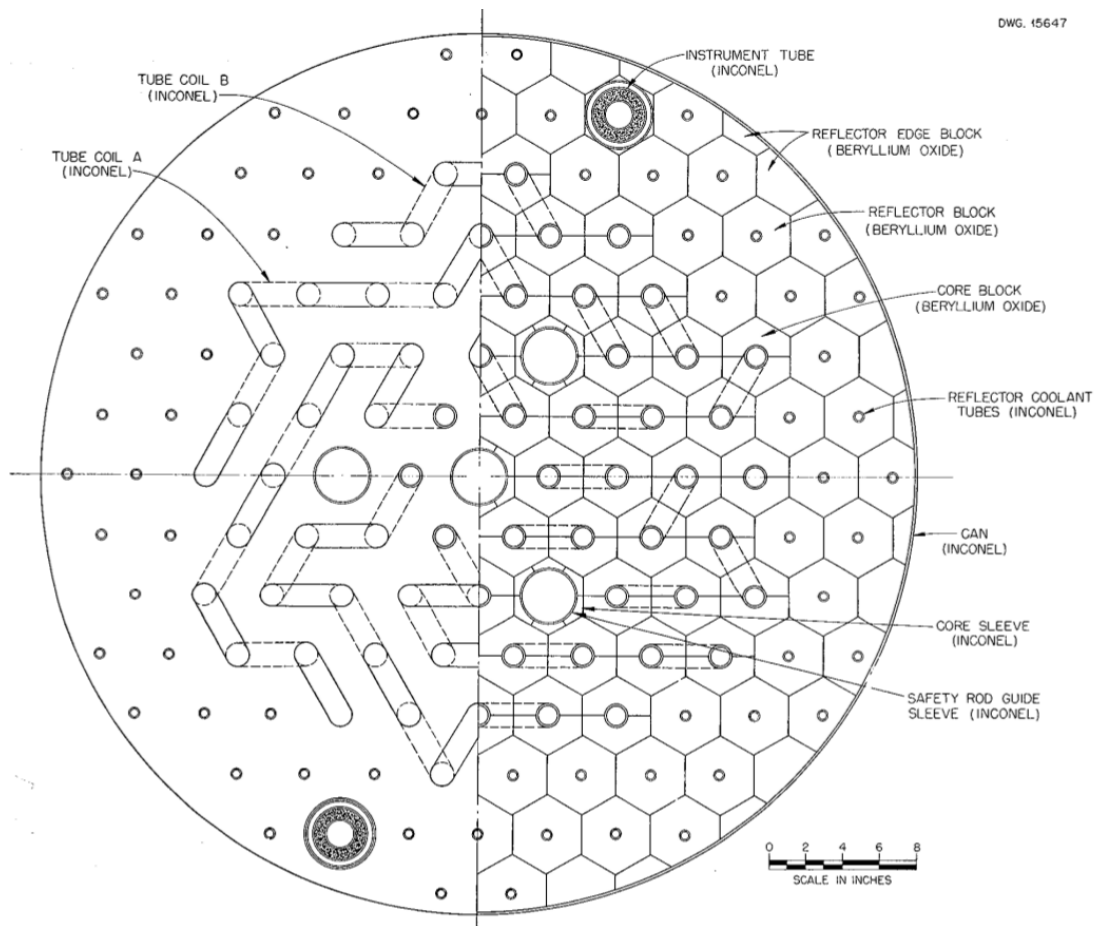


Figure III.3: Plan section of the ARE core [4].

III.2 Thermal-hydraulic model of the ARE

III.2.a Geometries and meshing

Three different domains are used in the ARE thermal-hydraulic model: the fuel salt, the sodium, and the solid domain. The meshes for the three domains can be seen in Figure III.4. The exterior BeO blocks are not cut to fit a cylinder. Instead, some blocks are removed entirely from the model. The rods and instrumentation assemblies are also removed entirely.

The salt flow in the inconel pipes is treated as one-dimensional. The salt mesh is composed of hexagonal prisms with the same section as the cylindrical pipes of the actual reactor.

In the actual ARE, the sodium flows through both the outer holes and the BeO

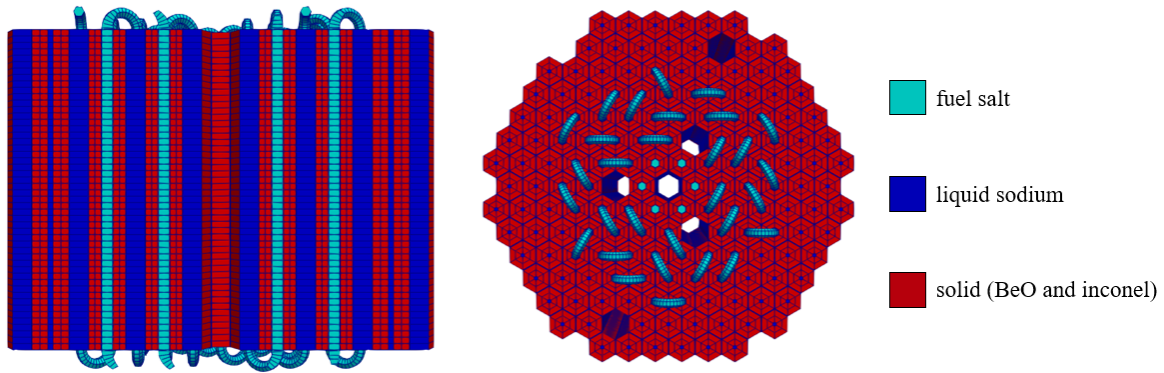


Figure III.4: Elevation section and top view of the ARE meshing in TrioCFD.

porosities. In the thermal-hydraulic model, the BeO is not treated as a porous medium. There are instead small gaps (2 mm in width) between the BeO blocks through which the sodium flows. The BeO block section in the thermal-hydraulic model is smaller than in the actual reactor, so that the section of a block and the sodium gap in our model equals the section of a block in the ARE. The sodium flow through both the holes and the gaps is treated as one-dimensional.

In the actual reactor, the bends on top and on the bottom of the reactor are immersed in liquid sodium. These two sodium layers are not modelled, because it would require to mesh a rather large, three-dimensional zone of free flow, which would greatly increase the computation time for the sodium flow.

III.2.b Resolved equations

Since the fuel salt flow is treated as one-dimensional along a coordinate x , the following equations are solved for the salt domain:

$$\frac{\partial u}{\partial x} = 0$$

$$\frac{\partial u}{\partial t} + u \frac{\partial u}{\partial x} = -\frac{1}{\rho} \frac{\partial P}{\partial x} + \mu \frac{\partial^2 u}{\partial x^2} + g(1 - \beta_{th})(T - T_0) \quad (\text{III.1})$$

$$\frac{\partial T}{\partial t} + u \frac{\partial T}{\partial x} = \alpha \frac{\partial^2 T}{\partial x^2} + \frac{S_{th}}{\rho c_p}$$

$$\frac{\partial C_i}{\partial t} + u \frac{\partial C_i}{\partial x} = D_m \frac{\partial^2 C_i}{\partial x^2} + S_{C_i} - \lambda_i C_i$$

Which results very simply for the velocity in $u(x, t) = u_{inlet}$, the imposed velocity at the inlet. The pressure gradient due to friction along the pipes is modelled by the empirical Darcy-Weisbach equation:

$$\frac{\Delta P}{L} = \Lambda \rho \frac{u^2}{2D} \quad (\text{III.2})$$

With ΔP the total pressure variation over the pipe length L , D the hydraulic diameter of the pipe, and Λ the Darcy friction factor, which is computed using the Blasius correlation:

$$\Lambda = 0.316 \text{Re}^{-0.25} \quad (\text{III.3})$$

For the sodium domain, similar equations are solved for the velocity and the temperature fields — there is no concentration equation — with different properties and source terms. The pressure gradient is also modelled by a Darcy-Weisbach equation.

For the solid domain, only a temperature equation is solved, in three dimensions (Equation 1.26).

III.2.c Physical properties

The three different domains possess different physical properties. The solid domain is divided into two different zones corresponding to the BeO blocks and the inconel tubes, with different physical properties. The properties of the different domains

were taken from the ARE operation report [4], and are summarised in Table III.1. All the properties were treated as constant in TrioCFD, at the reference temperature of 1100 K for the salt, and 950 K for the sodium and the solid. For the mass diffusivity, an arbitrary value was taken (at the order of magnitude for liquids).

Table III.1: Properties of the different materials in the ARE thermal-hydraulic model, at the reference temperature of 1100 K for the salt, and 950 K for the sodium and the solid.

Property	Unit	Material	Value
ρ	kg.m^{-3}	salt	3345
		sodium	738
		BeO	2400
		inconel	8510
c_p	$\text{J.K}^{-1}.\text{kg}^{-1}$	salt	1089
		sodium	875
		BeO	2010
		inconel	456
λ	W.K^{-1}	salt	2.6
		sodium	26.62
		BeO	1.3
		inconel	21.6
α	$\text{m}^2.\text{s}^{-1}$	salt	$7.13 \cdot 10^{-7}$
		sodium	$4.1 \cdot 10^{-5}$
		BeO	$2.3 \cdot 10^{-7}$
		inconel	$5.6 \cdot 10^{-6}$
μ	Pa.s	salt	$1.25 \cdot 10^{-2}$
		sodium	$1.46 \cdot 10^{-4}$
ν	$\text{m}^2.\text{s}^{-1}$	salt	$3.7 \cdot 10^{-6}$
		sodium	$1.98 \cdot 10^{-7}$
β_{th}	–	salt	$3.01 \cdot 10^{-4}$
		sodium	$2.60 \cdot 10^{-4}$
P_R	–	salt	5.19
		sodium	$4.8 \cdot 10^{-3}$
D_m	$\text{m}^2.\text{s}^{-1}$	salt	10^{-9}
S_C	–	salt	3700

III.2.d Boundary conditions

The heat exchangers, pumps and secondary circuits are not modelled. Instead, the salt and sodium velocities and temperatures are imposed at the inlets. Considering the long time the fuel salt spends out of the core (47 s) we assume a null precursor concentration at the fuel inlet. Zero gradients boundary conditions are applied at the salt and sodium outlets for every unknown. Since the sodium layers covering the bends are not modelled, the bends are treated as adiabatic walls. For the solid domain, For the solid domain, the heat transfer between the solid and the salt or the sodium is computed through a Newton's law where the two domains are in contact; adiabatic boundary conditions are applied elsewhere.

III.2.e Source terms

A Boussinesq source term (see Section I.2.e) is applied to the salt and the sodium velocity equations. The power source field — computed by the neutronic code — is a source term in the temperature equation for the fuel salt. Similarly, the precursor source fields are source terms in the concentration equations.

III.3 Neutronic model of the ARE

III.3.a Lattice calculation

In the lattice calculation step, a two-dimensional, detailed geometry of a third of the ARE core is used in order to compute the macroscopic, self-shielded, temperature-parametrised cross sections for the different materials composing the core (Figure III.5). These cross sections are stored in a file called a Multi-Parameter Output (MPO). Only a third of the core is used because the ARE presents a rotational symmetry by thirds — excluding the instrumentation assemblies. The boundary conditions are rotational symmetry conditions where appropriate, and vacuum conditions (no incoming flux) on the outer boundary of the reactor third. The regulating rod assembly at the center is included, but the concentrations in this assembly are divided by three, in order to offset the symmetry boundary conditions applied to it.

Three different energy meshes were tested: a very fine mesh of 33 energy groups, a fine mesh of 20 energy groups, and a coarse one of 6 groups. There was a 100 pcm

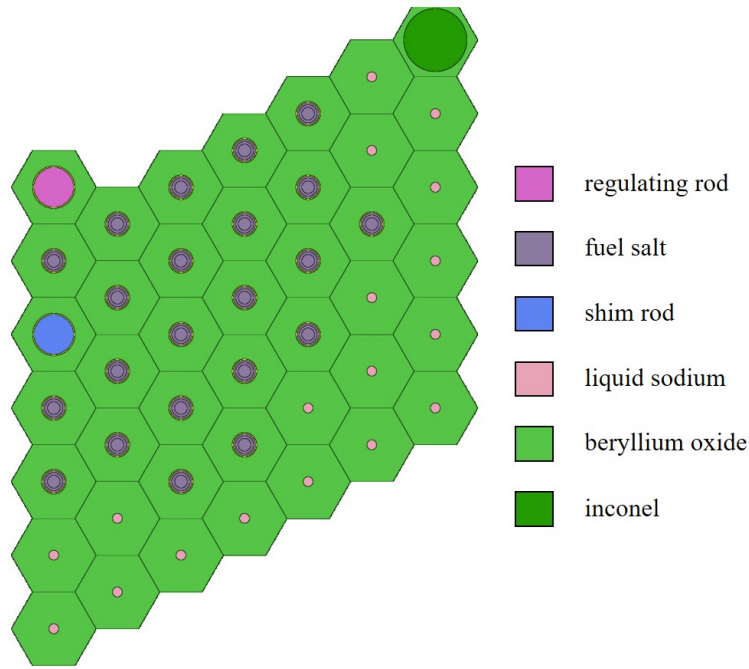


Figure III.5: Geometry used for the lattice calculation.

reactivity difference between the 6 group and the 20 group meshes on a core steady-state calculation, and no meaningful difference — less than 10 pcm — between the 20 group and the 33 group meshes. The 20 group mesh was thus used for the steady-state simulations, and the 6 group mesh was used for the transient simulations in order to speed up the calculations.

The number of precursor groups was set to 8 — since the library used for the microscopic cross sections is JEFF-3.3 [36], which considers 8 groups of precursors.

Regarding the fuel temperature parameter, 6 different points were computed during the lattice calculation, from 673 K to 1273 K; only three points were considered, at 673, 1273, and at 953 K which is the mean solid temperature of the ARE in its nominal state. Only two points were computed for the sodium (673 and 1273 K), sensitivity studies having shown that the impact of the sodium temperature on the core neutronics is negligible. Only two points were used for the rod concentration parameters as well (0 and 1). This results in 144 different states to compute during the lattice calculation.

III.3.b Determining the materials' compositions

The exact composition of the different materials in the ARE is not precisely known. In particular, the exact density of the beryllium oxide in the core is not known (it varies from 2270 to 2830 kg.m⁻³ between samples), as well as the exact concentration of different impurities in the inconel and the beryllium oxide (see Figure III.6). Sensitivity studies showed that both had a great impact on the core reactivity: a 10 % variation in BeO density caused a 6 % variation in reactivity, and there was a 2 % reactivity difference between the high and low estimations for impurities.

b. Inconel^a

Constituent	Amount (wt %)	Constituent	Amount (wt %)	Constituent	Amount (wt %)
Ni	78.5	Co ^b	0.2	Zr ^b	0.1
Cr	14.0	Al ^b	0.2	C	0.08
Fe	6.5	Ti ^b	0.2	Mo	Trace
Mn	0.25	Ta ^b	0.5	Ag, B, Ba	Trace
Si	0.25	W ^b	0.5	Be, Ca, Cd	Trace
Cu	0.2	Zn ^b	0.2	V, Sn, Mg	Trace

^aB. B. Betty and W. A. Mudge, *Mechanical Engineering*, February 1945.

^bAccuracy, $\pm 100\%$. Y-12 Isotope Analysis Methods Laboratory (spectrographic analysis). Y-12 Area Report Y-F20-14.

c. Beryllium Oxide*

Impurities	Amount (ppm)	Impurities	Amount (ppm)	Impurities	Amount (ppm)
Si	1050	Ca	780	Na	330
Al	213	Fe	114	Mg	50
Pb	45	Zn	<30	K	<25
Ni	<20	Cr	10	Li	<5
Mn	<5	B	2.8	Ag	<1
Co	<1				

Figure III.6: Estimated concentrations for different impurities in the inconel and BeO [4].

The critical mass for the ARE is known, however. Two MPOs were then created, that both gave $k_{eff} = 1$ with the critical fuel mass: one with a low BeO density and low impurities concentrations, and another with the high estimations for BeO density and impurities concentrations (see Table III.2).

The next step in the composition validation was to weight the control rods. The value of the regulating rod was measured at 400 pcm in the actual ARE, and each shim rod at 5800 pcm. For the low density, low impurities MPO, the values obtained for the rods coincided. For the high density, high impurities MPO however, the values of the

rods were too low (see Table III.2). This MPO was subsequently discarded, and the low density, low impurities MPO was used for the simulations.

Table III.2: BeO density, impurities concentrations, and rods values in the ARE and two different MPOs.

Property	Experimental data	High density, high impurities MPO	Low density, low impurities MPO
BeO density (kg.m ⁻³)	between 2270 and 2830	2700	2400
Impurities concentrations	see Figure III.6	highest estimations and 10 ppm for "Traces"	"Traces" and values under 30 ppm neglected
Regulating rod value (pcm)	400	299 (25 % difference)	398 (0.5 % difference)
Shim rod value (pcm)	5800	5107 (12 % difference)	5680 (2 % difference)

III.3.c Core calculation

Two different neutronic models of the ARE core were created. In the first one, the materials composing the core were homogenised into assemblies during the lattice step, and a core was created using four different homogenised assemblies: fuel assemblies (containing the fuel salt, the inconel piping, and the BeO block), reflector assemblies (containing the liquid sodium and the BeO block), the regulating rod assembly and the shim rods assemblies. In addition to these four assemblies, a homogenised paste was used to model the bends and the top and bottom sodium layers, containing a mix of fuel salt and liquid sodium. The geometry can be seen in Figure III.7.

A second, non homogenised model was created, which is presented in Figure III.8. One homogenised material was still used for the reflector in the fuel salt assemblies, which is a mix of the inconel piping and the BeO block. The inconel bottom sheet, as well as the sodium layers, are represented. The bends are straightened, but the total bend length is maintained. The instrumentation assemblies are also present — filled with inconel.

Like in the thermal-hydraulic model, the outer blocks are not cut to fit a cylinder, but some assemblies are completely filled with void — actually oxygen with a concentration of 10^{-16} cm⁻³.

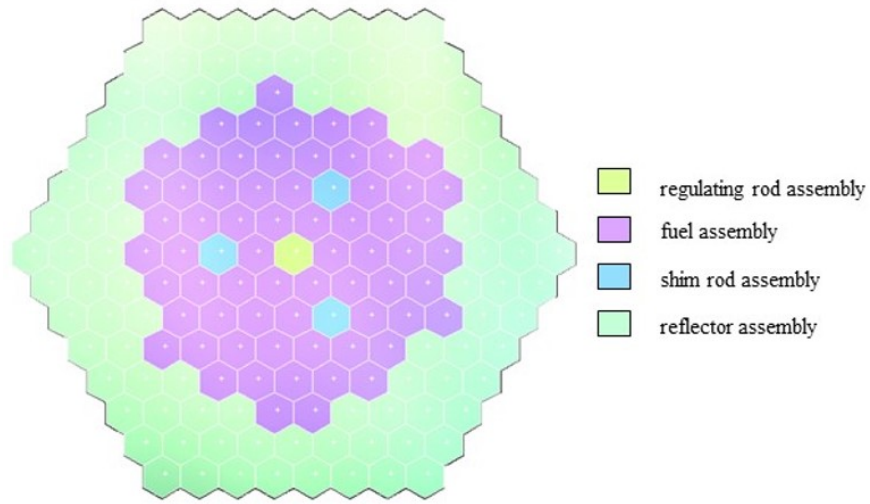


Figure III.7: Equatorial section of the homogenised geometry used for core calculations.

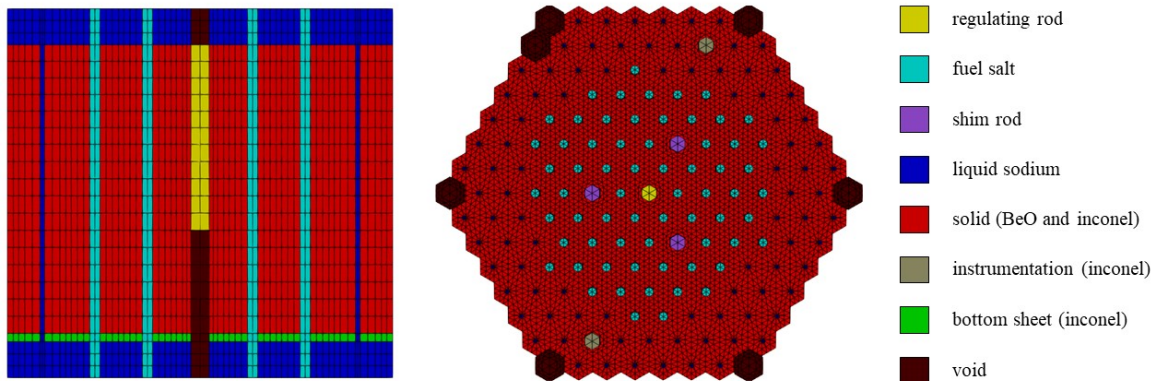


Figure III.8: Elevation and equatorial sections of the non-homogenised geometry used for core calculations.

A steady-state neutronic calculation was performed on both models, and a 200 pcm discrepancy was observed between the two models. Moreover, because of the dilution of the fuel in the paste material, the power density in the bends in the homogenised model was very low compared to the other one — between five and ten

times lower. The homogenised model was therefore discarded, and the non-homogenised model was used for the coupled calculations.

However, the use of a non-homogenised geometry required a development in the coupling scheme: the self-shielded cross sections for the salt depends on the three temperatures, and not just the salt temperature, but TrioCFD sends a null moderator temperature for the salt domain to APOLL03[®] — because there is no moderator in the salt domain. Therefore, an interpolation is performed where the moderator temperature in a salt cell (in the APOLL03[®] geometry) is equal to the mean of the surrounding moderator cells. The sodium temperature in a salt cell stays null, because the impact of the sodium temperature on the self-shielded salt cross sections is negligible. This interpolation was not performed on the other materials, because its impact was also negligible.

On a steady-state coupled calculation, the difference between performing or not this interpolation on the total reactivity was found to be about 10 pcm. Since the computational time of this interpolation is low — it is proportional to the quantity of fuel cells in the APOLL03[®] geometry — it was performed nonetheless.

III.4 Steady-state simulation: the ARE nominal state

The first steady-state, coupled calculation performed was the ARE nominal state. It is defined in the operation report [4] as:

- Total power: 2.1 MW.
- Fuel flow rate: $3.10^{-3} \text{ m}^3.\text{s}^{-1}$.
- Sodium flow rate: $10^{-2} \text{ m}^3.\text{s}^{-1}$.

In our numerical model, since the heat exchangers are not modelled, the fuel and sodium temperatures at the inlets were also set to their nominal value:

- Fuel inlet temperature: 928 K.
- Sodium inlet temperature: 937 K.

The coupling strategy is as defined in Section [II.4.c](#):

- A steady-state APOLL03[®] calculation is performed — for the first one, temperatures are uniform and the precursor concentrations are null.
- The power field and the precursor source fields are sent to TrioCFD.
- A steady-state TrioCFD calculation is performed.
- The precursor concentration fields and the temperature fields are sent to APOLL03[®]. The moderator temperature in the fuel cells is interpolated from neighbouring moderator cells.

This sequence loops until the convergence of the exchanged fields. The fuel and sodium outlet temperature were then measured and compared with the experimental values. Results are presented in Table III.3.

Table III.3: Compared values for nominal operating conditions.

Measure	Experimental Value	Simulation Value
T_{fuel}^{out} (K)	1102	1105
$T_{fuel}^{out} - T_{fuel}^{in}$ (K)	174	177
T_{sodium}^{out} (K)	998	950
$T_{sodium}^{out} - T_{sodium}^{in}$ (K)	61	13

The simulated fuel appears to be a little too warm, while the simulated sodium appears to be substantially too cold. These discrepancies can most probably be explained by the simplified sodium flow modelling:

- In the numerical model, the liquid sodium flows only through the reflector holes and between the BeO blocks, while in the actual experiment it also flows through the BeO porosities, resulting in a higher outlet temperature.
- In the numerical model, the top and bottom sodium layers are not modelled, so the sodium enters and exits the core rapidly. In the actual experiment, these layers would act as buffers, giving time for the sodium to heat up. The fuel salt in the bends also cools in these layers in the experiment, while this salt-sodium transfer is not reproduced in our model.
- Since the modelled sodium does not extract enough heat, the excessive heat is instead partly extracted by the fuel, which results in a slightly hotter fuel salt in the numerical model.

The nominal moderator temperature was not measured on the ARE, so it is not possible to know if the modelled moderator temperature coincides with the experimental value.

In order to reduce the discrepancies, the sodium flow rate was reduced in the numerical model. The results were not satisfying: even when dividing the sodium inlet flow rate by ten, the outlet temperature was only slightly hotter (+10 K). Since the sodium flow rate was modified in some experiments, the nominal flow rate was eventually kept in the numerical model. The main cause for the sodium temperature discrepancies would then be the absence of the top and bottom layers, but modelling them would greatly complexify the thermal-hydraulic model.

The low sodium temperature was eventually kept as is. Sensitivity studies were performed, and showed that the sodium density and temperature variations had a negligible impact on the neutronic calculation. The impact of the sodium modelling on the calculations is indirect, by modifying the temperatures of the fuel salt and the moderator.

III.5 Variation of β_{eff} with the fuel flow rate

The first actual experiment reproduced on the numerical model is the variation of β_{eff} with the fuel flow rate (experiment L-7 [4]). In the actual experiment, the ARE was set to a low-power (1 W) steady state, at nominal fuel flow rate, with all materials at 984 K. The fuel flow rate was then lowered, and the regulating rod adjusted to keep the reactor critical. The rod displacement was measured — which was translated into a reactivity variation — and the flow rate lowered further, until zero flow rate. Since the temperatures are kept constant, the reactivity variation with the fuel flow rate is solely caused by the precursor transport variation, so the reactivity variation is actually a β_{eff} variation. While β_{eff} at nominal flow is measured at 400 pcm, it goes up to 798 pcm for an immobile salt.

The experiment L-7 was easy to reproduce on the numerical model. All temperatures were set to 984 K in the neutronic model. Only the salt domain was used in the thermal-hydraulic model, and the energy equation was not solved — only the salt velocity and the precursor concentrations were computed. Different steady-state, coupled simulations were then performed — with the same coupling strategy as for the nominal state — with different imposed fuel flow rates. The final k_{eff} value for each

simulation was noted, and the variation of the k_{eff} compared to the k_{eff} at nominal flow rate was compared with the experimental data. Results are shown in Figure III.9.

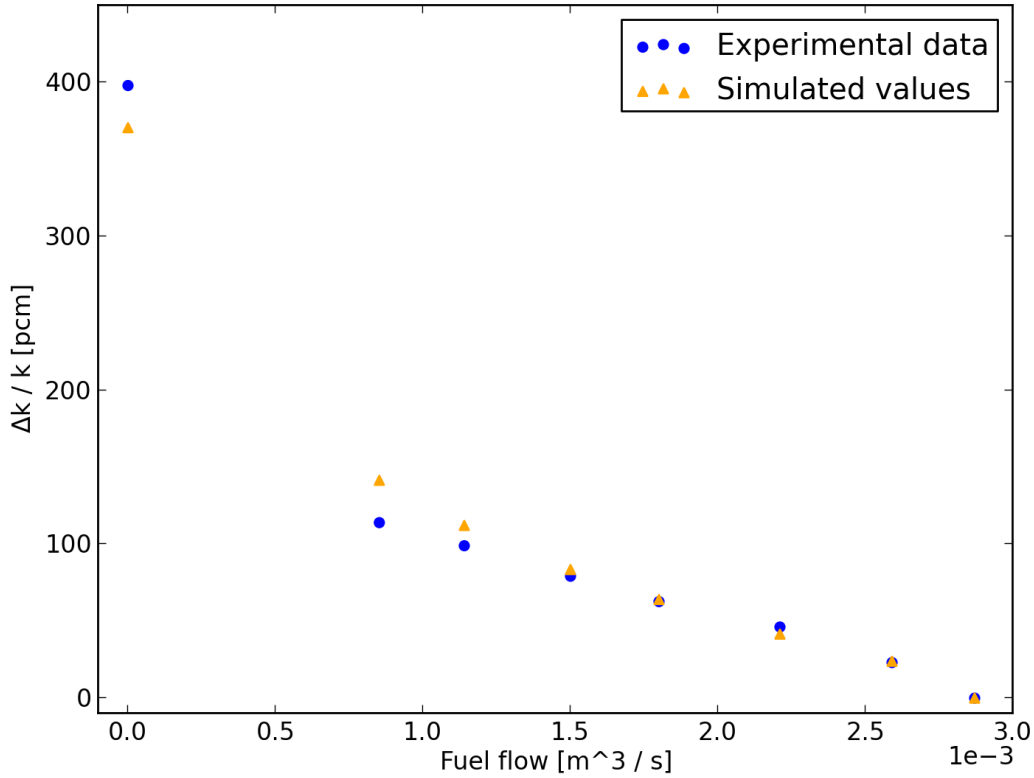


Figure III.9: Variations of reactivity with fuel flow rate: experimental values (blue circles) and simulated values (yellow triangles).

For small variations of the flow rate, the results are in good agreement with the experimental values. The higher simulated values on the intermediary points (at $1.14 \cdot 10^{-3}$ and $0.8 \cdot 10^{-3} \text{ m}^3 \cdot \text{s}^{-1}$) could be explained by the simplified one-dimensional flow, which would flush out more precursors than a more realistic velocity profile with a viscous sublayer. It is also possible that the imposed null precursor concentration at the inlet is causing this over-variation in the simulation. However, at null flow rate — so with immobile precursors — the simulated data present a 7 % lower value than the experiment, which cannot be explained by the simplified one-dimensional flow nor the inlet boundary condition. Since the flow rate is null, the k_{eff} value given by APOLL03[®] was compared to a Monte-Carlo calculation, using TRIPOLI-4[®] [82]. The value given for the k_{eff} by TRIPOLI-4[®] was $1.0380 \pm 10 \text{ pcm}$, which corresponds to the

value of 1.0370 computed by APOLL03[®].

III.6 Transient simulation: insertion of a dollar of reactivity

III.6.a The actual experiment

Two transient experiments were selected to be reproduced. The first one (experiment H-8) is a reactivity insertion. Starting at nominal state (power at 2.1 MW) with the regulating rod fully inserted, the rod is withdrawn at maximum speed: this corresponds to a +400 pcm reactivity insertion (one β_{eff} , or one dollar) in 37.5 seconds.

The power thus increases — it doubles and reaches 3.9 MW in 37.5 s — which causes the fuel temperature to rise. The temperature feedback in turn lowers the reactivity and the power, and the reactor reaches a new steady state at 2.9 MW in three minutes. The experimental data are presented in Figure III.10.

We can see in Figure III.10 that the power starts to increase as soon as the rod is moving. The outlet temperature is also immediately impacted, because the fuel salt is heated by a higher power before exiting the core. A time delay of about 47 s between the outlet and inlet temperature variation can be noted, which corresponds to the fuel transit time. Because of this transit time, the time for the mean fuel temperature to reach equilibrium is quite long.

The new equilibrium power (2.9 MW) is slightly higher than the initial power (2.1 MW) because the mean fuel temperature is higher, which results in more heat extraction in the heat exchangers — the helium flow rate in the heat exchanger is constant throughout the experiment. The extracted power being higher, the neutronic power adapts to it.

III.6.b First test run: instantaneous reactivity insertion

The modelling of the experiment H-8 on the numerical model rose several problems, in particular regarding the rod movement. While it is easy to set a ramp in TrioCFD for a transient simulation — like an inlet temperature ramp — it is not possible to set an MPO parameter ramp in APOLL03[®]. A first test run was thus modelled in an extremely simplified way:

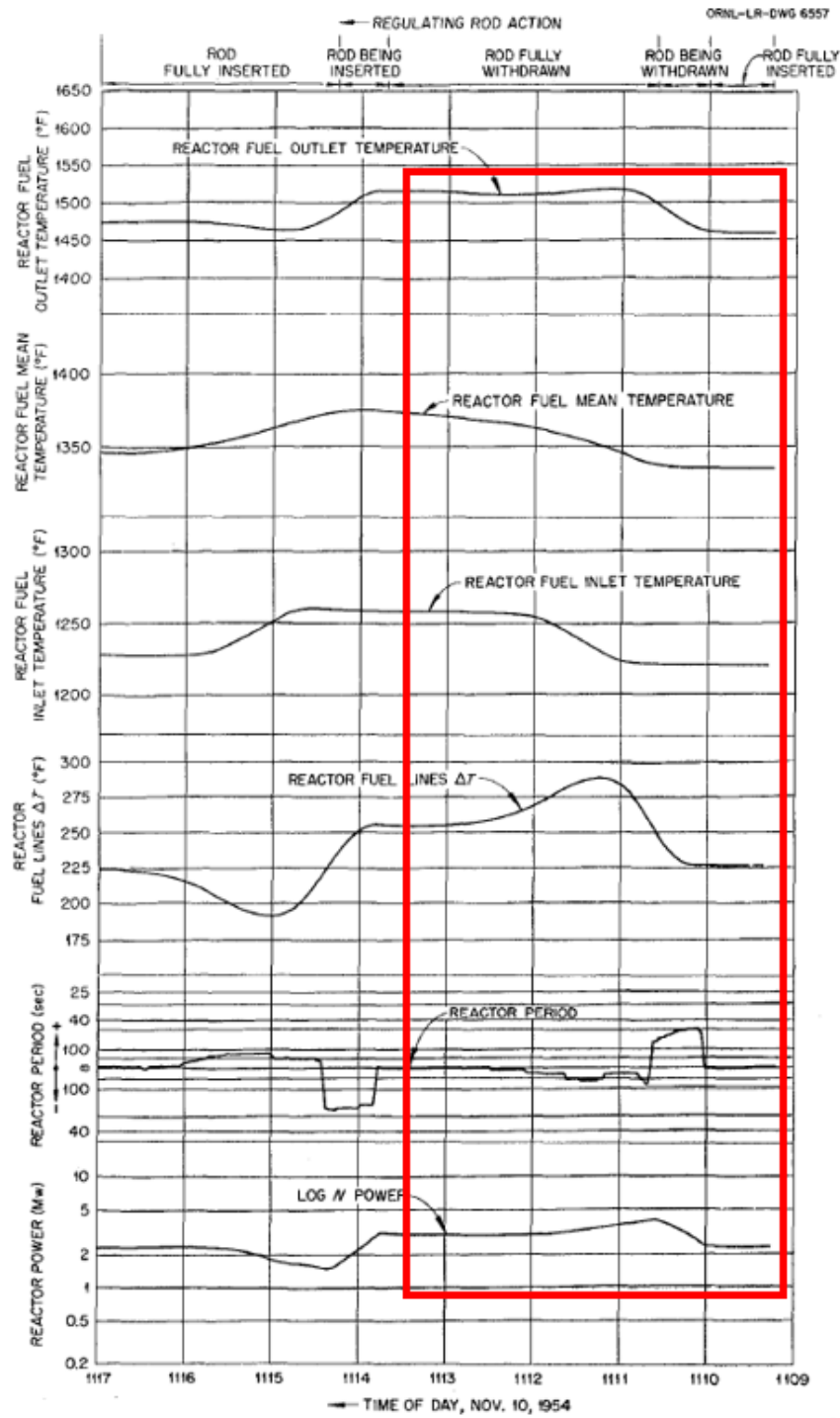


Figure III.10: Experiment H-8, reactivity insertion: time is read from right to left (in minutes). The first half of the experiment (in the red square) is described and reproduced.

- The initial state is the nominal state with the regulating rod fully inserted (rod parameter at 1). A critical simulation has been performed, so the reactor is perfectly critical (see Section II.1.e).
- The regulating rod parameter is set to 0. This corresponds to an instantaneous reactivity insertion of +400 pcm.
- A transient coupled simulation is performed — as defined in Section II.4.d. The timestep before exchange between both codes is 10^{-2} s.

This first test run resulted in a higher power increase on a much shorter time. Results are presented in Figure III.11. The neutronic power triples and reaches 6.7 MW in 0.3 s, before decreasing due to the temperature feedback. A new equilibrium is reached in about 15 s at 3.3 MW. Once again, the new power at equilibrium is higher than initially, because the virtual extracted power has increased — the outlet fuel temperature has increased, and the inlet fuel temperature has been kept constant.

The higher maximum power on the simulation has two likely causes: the instantaneous reactivity variation, and the constant inlet fuel temperature — it increases by 30 K in the actual experiment — which inhibits a part of the temperature feedback. The final simulated power is 3.3 MW, which is 14 % higher than the experimental data — the virtual extracted power should be higher than in the experiment because the inlet temperature is lower.

When looking at the outlet fuel temperature evolution, it reaches a maximum of 1163 K at 5.6 s before going down and reaching a final value of 1145 K — although the transient has not quite converged. The final value is within 10 K of the experimental data — the final experimental outlet temperature is 1155 K.

III.6.c Progressive reactivity insertion by diluting the rod

The results of the previous simulation were promising, especially the final state, but the instantaneous reactivity variation was too far from the actual experiment protocol and resulted in a much shorter transient. To solve this problem, a progressive reactivity insertion simulation was designed:

- The initial state is the nominal state with the regulating rod fully inserted. A critical simulation has been performed, so the reactor is perfectly critical (see Section II.1.e).

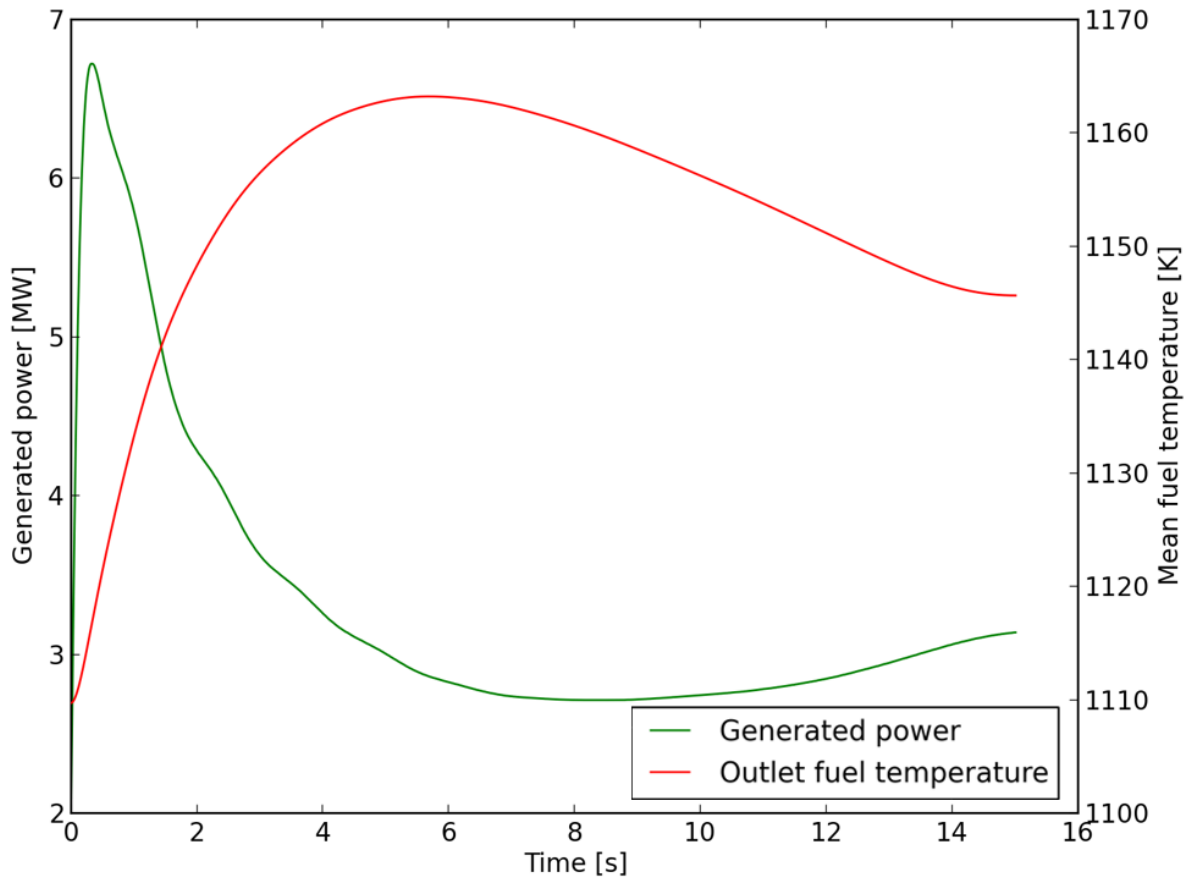


Figure III.11: Transient simulation H8: instantaneous reactivity insertion of +400 pcm.

- A transient coupled simulation is performed (with a timestep before exchange of 10^{-2} s); for the first 37.5 s of the simulation, at every exchange, the value of the regulating rod parameter is decreased linearly, such that the parameter is null at 37.5 s.
- The transient then continues normally until convergence of the fields.

This method effectively dilutes progressively the entire regulating rod on 37.5 s, which is slightly different than withdrawing it. The results are presented in Figure III.12.

The neutronic power increases steadily and reaches a maximum of 3.8 MW at 36.5 s (instead of 3.9 MW at 37.5 s in the actual experiment, a 2.5 % difference). The temperature feedback then causes the power to decrease, and to reach a final value of 3.3 MW, like for the previous simulation. Some oscillations of the neutronic power are observed after 40 s, which do not appear in the experimental data.

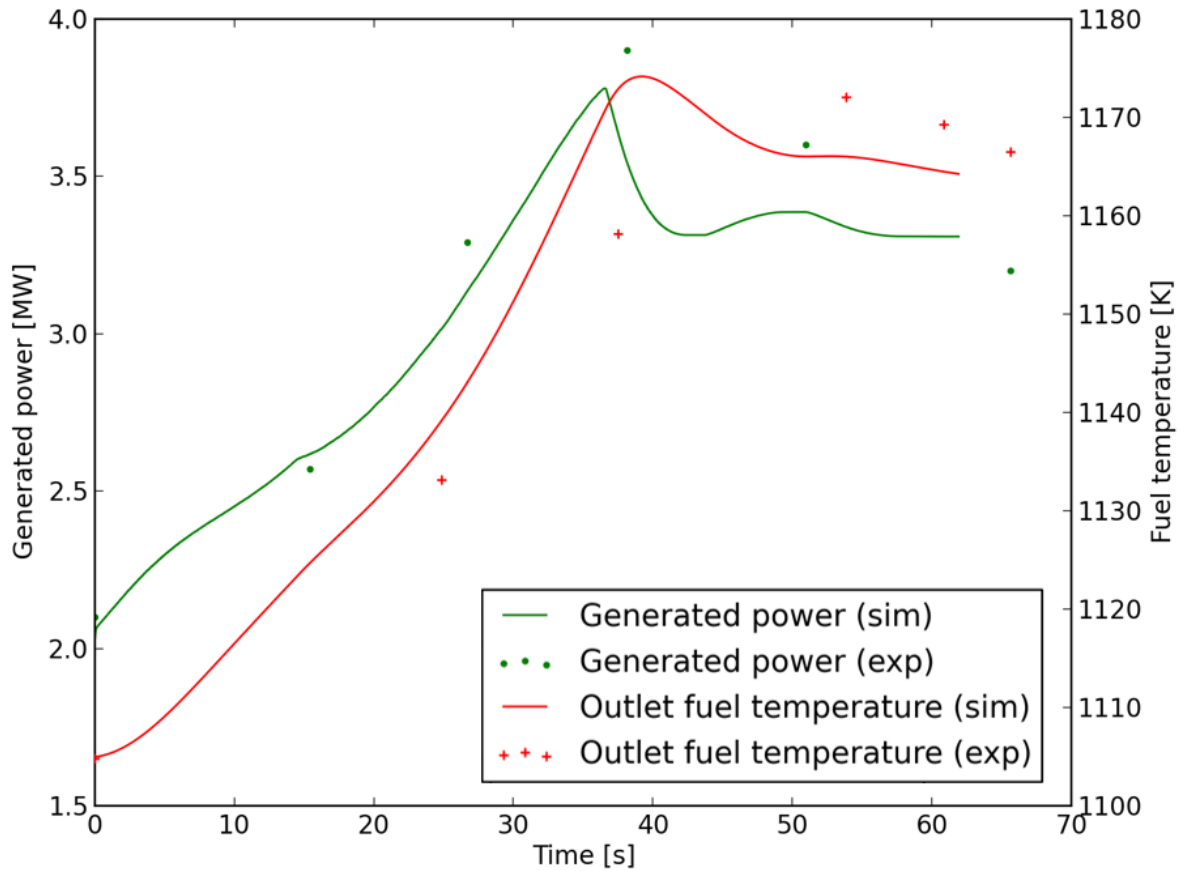


Figure III.12: Transient simulation H8: progressive dilution of the regulating rod. The experimental data were digitalized using WebPlotDigitizer [83].

When looking at the outlet temperature evolution, it reaches a maximum of 1174 K at 39 s (instead of 1172 K at 55 s) before going down to 1164 K, although the transient is not quite converged.

Diluting the rod over 37.5 s greatly improved the power evolution — the maximum value is 2.5 % lower than the experimental value — as well as the temperature evolution — the maximum value is 2 K higher than the experimental value. Yet the final values (the final power is still 14 % too high) are still not quite in agreement with the experiment. The final values discrepancies are most likely due to the fact that the inlet temperature is fixed in the simulation.

III.6.d Progressive reactivity insertion with a varying inlet temperature

A final simulation was performed, with a progressive dilution of the regulating rod, and where the inlet temperature increased linearly to better reproduce the experimental data.

- The initial state is the nominal state with the regulating rod fully inserted. A critical simulation has been performed, so the reactor is perfectly critical (see Section II.1.e).
- A transient coupled simulation is performed (with a timestep before exchange of 10^{-2} s); for the first 37.5 s of the simulation, at every exchange, the value of the regulating rod parameter is decreased linearly, such that the parameter is null at 37.5 s.
- The inlet fuel temperature is set to 928 K until 47 s, where it increases linearly over a minute to 950 K.
- The transient continues until convergence of the fields.

The results are presented in Figure III.13.

Before 47 s, the results are identical to the previous simulation, the transient being the same. Unfortunately, the calculation stopped at 63 s, for unknown reasons (it seems linked to memory use). However, even with a low increase of the inlet fuel temperature, we can observe a decrease of the neutronic power after 50 s compared to the previous simulation.

A longer simulation should be performed in order to assess the temperature and power final values. Still, the results currently available show a good agreement between our numerical model and the experimental data, which contributes to the validation of our model and the APOLL03[®] – TrioCFD code.

It should also be noted that while the mean fuel temperature evolution was recorded during the simulations, it is not presented in the figures above, due to great discrepancies with the experimental data. The most plausible explanation for these discrepancies is that the experimental mean fuel temperature is not simply the mean fuel temperature in the core, but in the whole fuel loop, or at least in the core and the top and bottom salt collectors — it is unfortunately not precisely defined in the

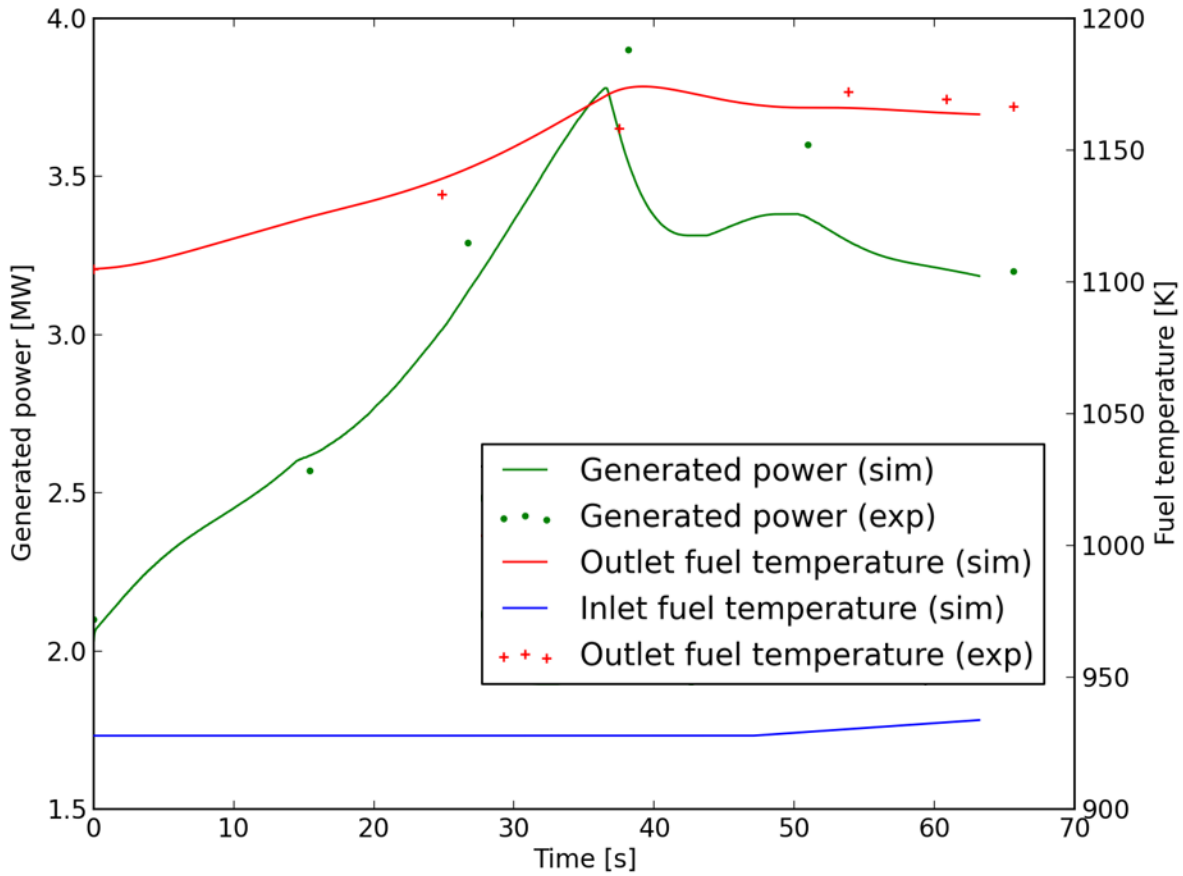


Figure III.13: Transient simulation H8: progressive dilution of the regulating rod with a varying inlet temperature. The experimental data were digitalized using WebPlot-Digitizer [83].

operation report [4]. It seems difficult to explain the very different evolutions of the experimental mean and outlet fuel temperatures otherwise.

III.7 Transient simulation: variation of extracted power

III.7.a The actual experiment

The second transient experiment selected (experiment H-14) is a load-following transient: starting at a low-power state ($5.66 \cdot 10^{-2}$ MW), the helium flow rate in the fuel-to-helium heat exchangers is increased over a minute, which results in a lower inlet fuel temperature in the core (it decreases from 997 to 953 K over a minute) and a slightly lower mean fuel temperature (it decreases from 1016 to 1013 K). The

temperature feedback causes the reactivity and the power to increase, until the reactor reaches a new steady state at 1.05 MW. When the power increases, it causes the mean and outlet fuel temperature to increase (the outlet fuel temperature increases from 1036 K to 1080 K while the mean fuel temperature increases slowly to 1020 K). The experimental data are presented in Figure III.14.

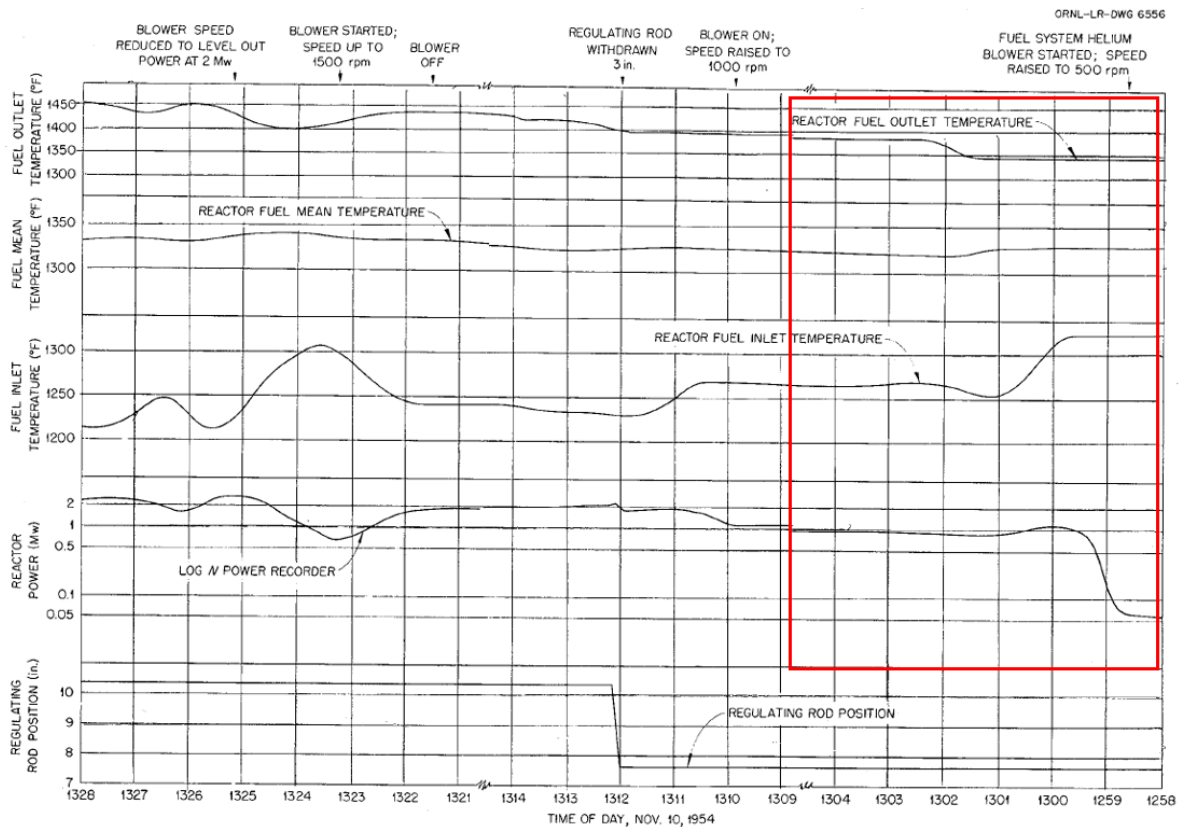


Figure III.14: Experiment H-14, extracted power increase: time is read from right to left (in minutes). The first part of the experiment (in the red square) is described and reproduced.

Important time lags can be observed in Figure III.14. The fuel inlet temperature should be modified as soon as the extracted power increases, but instead a 1 min time lag is observed. The time lag does not appear on the neutronic power reading, so it would seem like the power increases without any temperature variation — which is not possible. The time lags for the mean and outlet fuel temperatures are larger yet, estimated at respectively 1.5 and 2 min.

There is no definitive explanation for such time lags (see [4], p91): the most plausible one is that, while the power detectors were placed inside the core and registered

power variations very quickly, the thermocouples were placed at the exterior of the core, so their readings were influenced not only by the quick fuel temperature variations, but also by the much slower temperature variations of the moderator.

By starting the inlet fuel temperature variation at the same time as the power variation, and adding the time required to pass through the core for the outlet temperature reading (about 8 s), the temperature readings can be adjusted.

III.7.b The simulated experiment

Since the heat exchangers are not present in our ARE numerical model, the inlet fuel temperature is instead directly modified in TrioCFD:

- The initial state is a low-power steady state (power at $5.66 \cdot 10^{-2}$ MW, inlet fuel temperature at 997 K, outlet fuel temperature at 1035 K). A critical simulation has been performed, so the reactor is perfectly critical (see Section II.1.e).
- A transient coupled simulation is performed (with a timestep before exchange of 10^{-2} s); for the first 58 s of the simulation, the inlet fuel temperature decreases linearly from 997 to 953 K.

The power and outlet fuel temperature are then measured and compared with the experimental data. Results are presented in Figure III.15.

Unfortunately, the calculation stopped at 50 s, for the same unexplained reason than in the previous simulation. The power evolution seems promising however: it reaches 0.88 MW at 50 s, and is still increasing. The outlet fuel temperature evolution seems also in quite good agreement with the experimental data, except for a slight decrease of the simulated temperature between 15 and 30 s which is not observed in the experiment.

The error causing the transient simulations to stop should be solved before performing other long transients. It is difficult to conclude on the H-14 experiment with the results currently available, although they look promising.

While some troubleshooting must be done before concluding on the accuracy of our numerical model of the ARE, the global behaviour of the APOLL03[®] – TrioCFD was extensively tested during this validation step, and the results were satisfactory. The code should be able to solve more complex MSR models, assuming no long transients are computed.

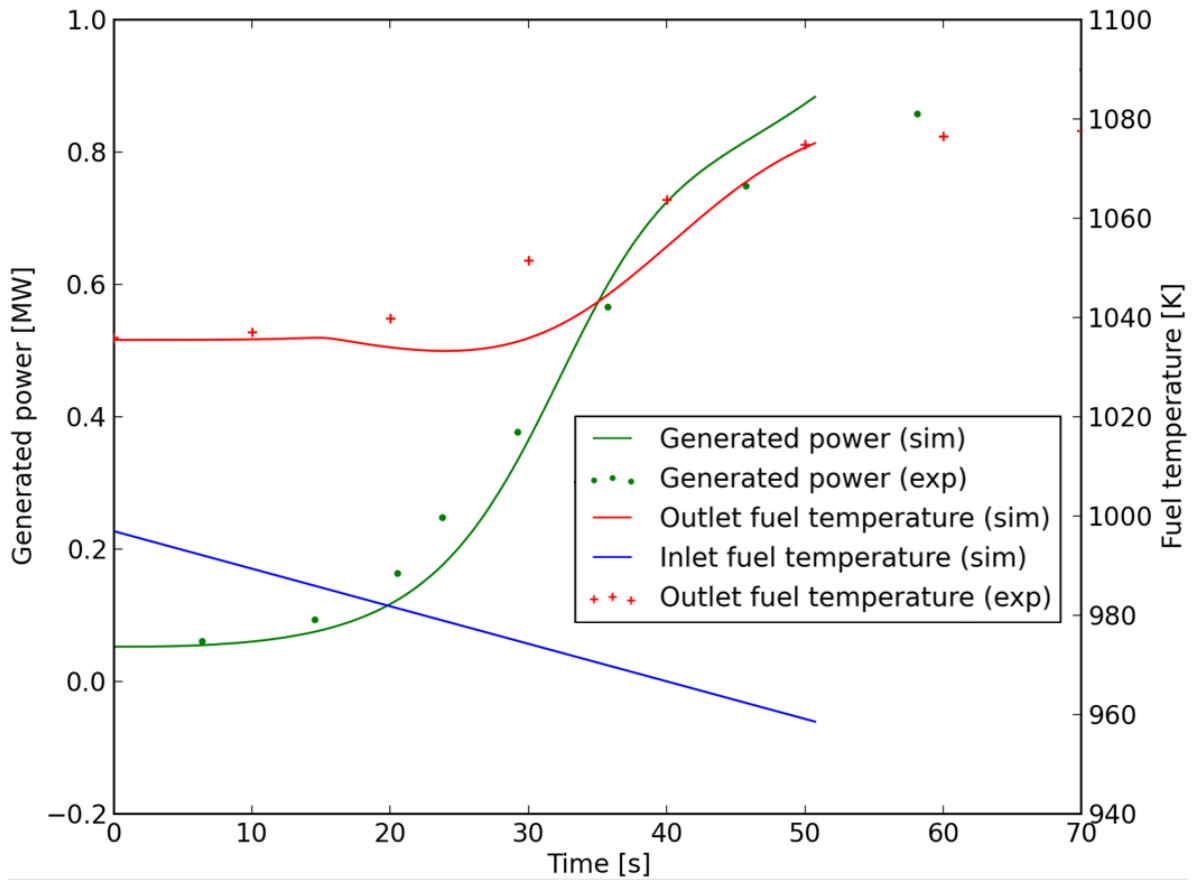


Figure III.15: Simulated experiment H-14: inlet fuel temperature ramp. The experimental data were digitalized using WebPlotDigitizer [83] and corrected for the time lags.

In this chapter, we created a numerical model of the Aircraft Reactor Experiment (ARE). Using the APOLL03[®] – TrioCFD code, steady-state and transient simulations were performed on the numerical model and compared with the experimental data. The results contributed to the validation of the multiphysics code. The next step, presented in the next chapter, is to use the APOLL03[®] – TrioCFD code to model turbulent flows in MSR.

Chapter IV

Modelling of turbulent fluctuations in the Molten Salt Fast Reactor

The purpose of this chapter is to use the APOLL03[®] – TrioCFD code to model the turbulent fluctuations in the core of the Molten Salt Fast Reactor, presented in Section IV.1. A thermal-hydraulic model of the MSFR was created in TrioCFD (Section IV.2). Many sensitivity studies were performed on the thermal-hydraulic model of the MSFR, using a RANS turbulence model, in order to optimise the model (Section IV.3). A numerical benchmark using RANS modelling was developed in collaboration with other partners, in order to compare the results given by different CFD codes (Section IV.4). The thermal-hydraulic model was then used to perform LES simulations, in order to estimate the temperature turbulent fluctuations without neutronic feedbacks (Section IV.5). A neutronic model of the MSFR was developed in APOLL03[®] (Section IV.6). Both models were coupled in order to compute the coupled nominal state of the MSFR (Section IV.7).

Some early results on the MSFR thermal-hydraulic modelling led to a conference paper [84].

IV.1 The Molten Salt Fast Reactor	93
IV.1.a Fuel cycle and salt composition	94

IV.1.b	Core geometry and materials	94
IV.1.c	Bubble injection	94
IV.1.d	Pumps and heat exchangers	95
IV.1.e	Free volume and draining tanks	95
IV.2	Thermal-hydraulic model of the MSFR	95
IV.2.a	Resolved equations	95
IV.2.b	Physical properties	96
IV.2.c	Geometries and meshing	96
IV.2.d	Turbulence models	99
IV.2.e	Boundary conditions	99
IV.2.f	Source terms	100
IV.3	RANS simulations on the MSFR	101
IV.3.a	Impact of the geometry	101
IV.3.b	Impact of the heat exchanger modelling	105
IV.3.c	Mesh convergence on the open sector geometry	106
IV.3.d	Impact of the spatial scheme	106
IV.3.e	Impact of the RANS model	107
IV.4	Numerical benchmark on the open sector	108
IV.5	LES simulations on the MSFR	111
IV.5.a	Impact of the geometry	112
IV.5.b	Comparison with RANS simulations	115
IV.5.c	Turbulent fluctuations in the MSFR core	115
IV.6	Neutronic model of the MSFR	120

IV.6.a	Lattice calculation	120
IV.6.b	Core calculation	121
IV.6.c	Neutronic simulation: power distribution	121
IV.7	Coupled simulations on the MSFR	122
IV.7.a	Delayed neutrons precursors modelling	122
IV.7.b	Coupled steady-state of the MSFR	124
IV.7.c	Coupled transient simulations on the MSFR	125

IV.1 The Molten Salt Fast Reactor

The Molten Salt Fast Reactor (MSFR) is a fast-spectrum breeder molten salt reactor concept, developed initially by CNRS in France [85], then through European projects [12]. The MSFR system is composed of a core (in green in Figure IV.1) connected to 16 sectors, each containing a pump and a heat exchanger. Different variations on the MSFR design exist [86], we present here the characteristics of the reference MSFR.

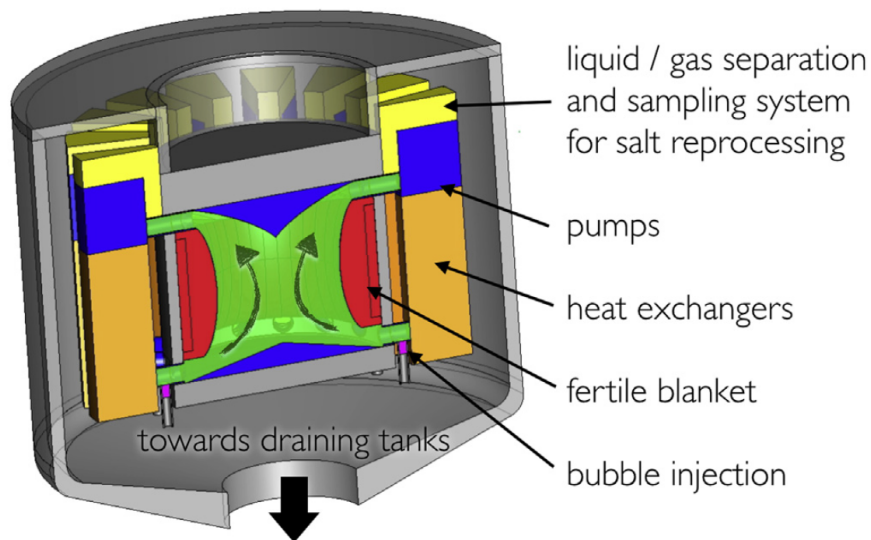


Figure IV.1: Schematic layout of the MSFR.

IV.1.a Fuel cycle and salt composition

The MSFR is a breeder reactor, that operates with a $^{232}\text{Th}/^{233}\text{U}$ cycle and a $\text{LiF}-\text{ThF}_4-\text{UF}_3$ fluoride salt (77.5 – 22.5 – 2.5 mol% at start-up). The lithium is heavily enriched in ^7Li to limit the tritium generation — the lithium is composed of 99.999 mol% of ^7Li and 0.001 mol% of ^6Li .

A radial fertile blanket (in red in Figure IV.1) is also present to improve the breeding ratio. It has the same composition as the fuel salt, but loaded only with ^{232}Th as heavy nuclei.

IV.1.b Core geometry and materials

As shown in Figure IV.1, the core geometry is a toroid — approximately 2 m in height and diameter. The fuel salt flows through the critical region where it heats up and rises to the sixteen "legs" connecting the core to the heat exchangers, then goes down the heat exchangers and back to the critical region. The fuel completes the loop in about 4 seconds. The flow in the core is highly turbulent ($\text{Re} \approx 5 \cdot 10^5$). The toroidal geometry results from a preliminary optimization study using RANS simulations [87].

The total fuel salt volume is 18 m^3 : half in the critical region and half outside. The total volume results from a trade-off between the temperature feedbacks on the one hand, and the breeding ratio and the vessel irradiation on the other — a smaller volume boosts the density feedback as more fissile matter will escape the critical region quicker, but also implies more neutron leakage, which will lower the breeding ratio and cause more vessel irradiation [85]. The fuel volume outside of the critical zone also results from a trade-off between the extracted heat — more extracted heat with more fuel outside of the critical zone — and the β_{eff} — which is lower with more fuel outside of the critical zone.

The total power is 3 GW_{th} , the mean temperature is about 700°C — the inlet core temperature is at about 650°C , the outlet core temperature at about 750°C .

The structural materials of the reactor are composed of Hastelloy-N — a nickel-based alloy, similarly to what was used in the MSRE [88].

IV.1.c Bubble injection

In previous MSFR designs, a bubbling system was present to help removing the gaseous fission products. Helium was injected in the core, and the gas was extracted

before the fuel would reach the pump. The presence of helium bubbles in the core however, had an impact on the core neutronics and the fuel compressibility, which delayed the temperature feedbacks during transients [67].

In the current MSFR design, there is no bubble injection. The gaseous fission products could form some bubbles in the core, before being extracted at the pumps. No bubbles were considered in this study.

IV.1.d Pumps and heat exchangers

The pumps are located above the heat exchangers, where the fuel is the hottest. This is to limit the cavitation in the pump: the solubility in the salt increases with the temperature, so there are fewer bubbles when it is hot.

The exact composition and configuration of the heat exchangers is not known yet. The heat exchangers are usually considered to be plate exchangers made of a nickel-based alloy [89].

IV.1.e Free volume and draining tanks

An expansion vessel, enabling the fuel salt expansion when it heats up, is necessary. While not precisely defined, it is usually modelled just above the critical zone [73]. No expansion vessel was modelled in this study.

Below the core, there is an emergency draining tank: in case of a breach, the fuel salt would flow down into this tank, which must have a sub-critical geometry when full while allowing for the decay heat passive removal through natural convection [73]. This emergency draining system was not modelled in this study.

IV.2 Thermal-hydraulic model of the MSFR

IV.2.a Resolved equations

Only the fuel salt is considered in the thermal-hydraulic model. The velocity and pressure fields for the fuel are obtained by computing the Navier-Stokes and pressure equations (Equations I.29 and I.21). The temperature field is obtained through the energy equation (Equation I.26).

For the model to be complete, the precursor concentrations should also be computed (through Equation I.27) and be exchanged with APOLL03[®]. They were not computed in this study however, in order to speed up both the thermal-hydraulic calculation — by not solving the concentration equation — but mostly the neutronic calculation (see Section IV.7).

IV.2.b Physical properties

We consider the salt composition defined above (Section IV.1.a), used for the start-up of the MSFR with a thorium cycle [88]. In the absence of precise measures of this specific salt’s properties, the modelled salt properties are taken constant, from a ⁷LiF–ThF₄ salt at the reference temperature of 700 °C [55]. These properties are described in Table IV.1.

Table IV.1: Properties of the MSFR salt used in the simulations.

Property	Unit	Value at 700 °C	Variation from 600 °C to 750 °C
ρ	kg.m ⁻³	4125	4214 – 4081
c_p	J.K ⁻¹ .kg ⁻¹	1594	1316 – 1733
λ	W.K ⁻¹	1.01	1.001 – 1.014
α	m ² .s ⁻¹	1.5 10 ⁻⁷	1.81 10 ⁻⁷ – 1.42 10 ⁻⁷
μ	Pa.s	1.015 10 ⁻²	1.5 10 ⁻² – 8.43 10 ⁻³
ν	m ² .s ⁻¹	2.46 10 ⁻⁶	3.56 10 ⁻⁶ – 2.07 10 ⁻⁶
β_{th}	–	2.14 10 ⁻⁴	–
P _R	–	16	19.67 – 14.57

IV.2.c Geometries and meshing

A CAD model and different meshes were created for the MSFR, using the SALOME software [75]. The CAD model is presented in Figure IV.2. Two different geometries were considered: only one sector — one 16th — of the core, and the full core. TrioCFD currently only handles tetrahedral meshes for turbulent simulations. The RANS simulations were performed on a coarse mesh — 7 millions tetrahedra for the full core — determined through a mesh convergence study (see Section IV.3.c); the RANS mesh can be seen in Figure IV.3.

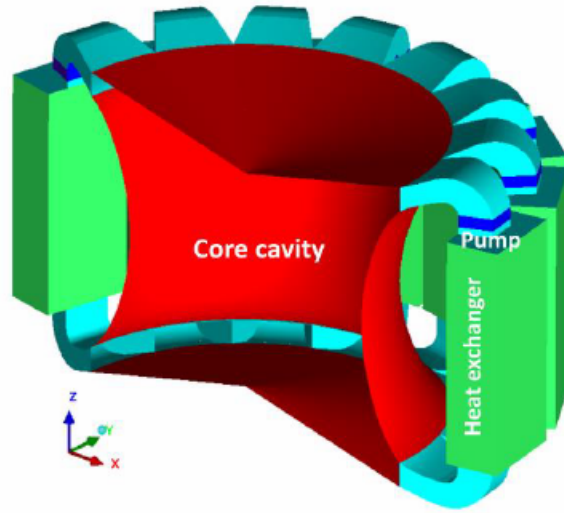


Figure IV.2: CAD of the MSFR for the thermalhydraulics modelling.

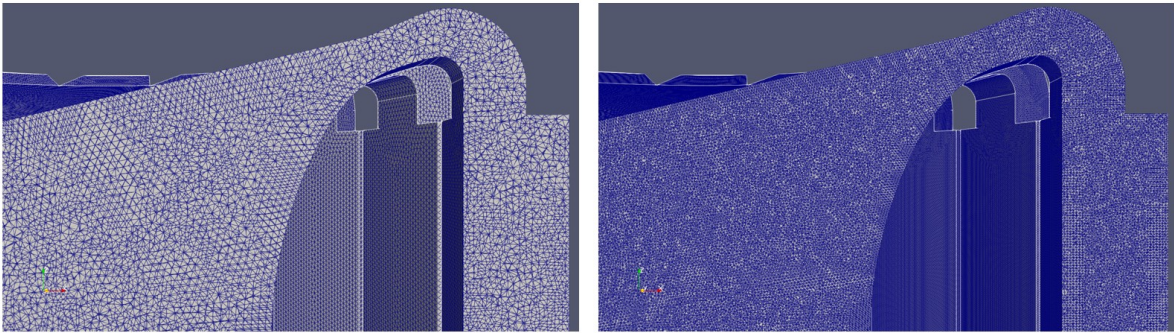


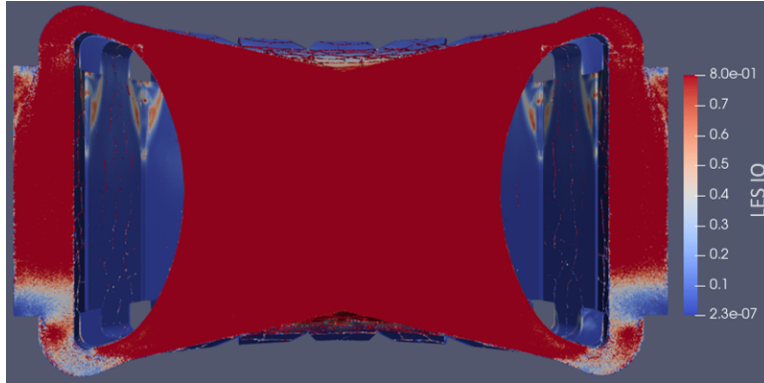
Figure IV.3: Meshes used for the RANS (left) and the LES (right) simulations.

A RANS calculation was performed in order to compute the transverse Taylor microscale λ_T of the flow. λ_T was about 5 mm in the critical region, and about 2.5 mm near the legs connecting to the heat exchangers. The LES mesh was thus built with a reference edge size of 1 cm — as the unknowns are discretized in the centre of the tetrahedra's faces in TrioCFD, the distance between two calculation points is about three times smaller than the reference edge size. The LES mesh is composed of 120 millions tetrahedra for the full core, and can be seen in Figure IV.3.

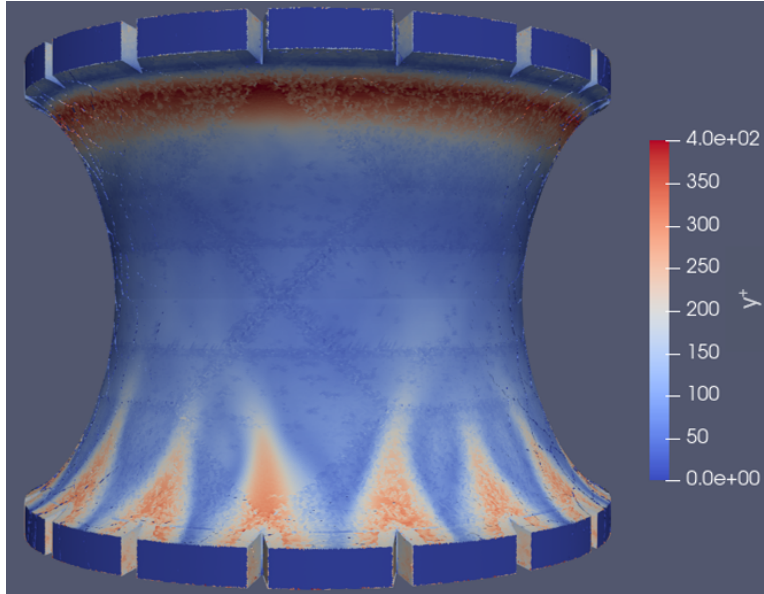
The good resolution of the LES mesh was verified by computing the Index of Resolution Quality (LES_IQ, see Equation II.22). The LES_IQ of the full-core simulation is presented in Figure IV.4(a). In the critical region, it is over 0.8 in every cell. The mesh is under-refined in the heat exchangers, but a detailed prediction of the velocity is not necessary in these regions — since the heat exchangers are not precisely

modelled.

Since the Reichardt law of the wall (Equation I.34) was used in both RANS and LES calculations, the good resolution of the surface mesh was verified by computing the dimensionless wall distance (y^+). The y^+ for the LES simulation is presented in Figure IV.4(b). With this surface mesh size, some of the upper region cells have a y^+ value a little over 400, which is satisfactory.



(a) LES_IQ for the LES simulation (max scale fixed at 0.8).



(b) y^+ for the LES simulation (max scale fixed at 400).

Figure IV.4: Parameters for the fine mesh quality assessment.

The RANS mesh was decomposed into 350 zones of approximately 20 000 cells, so the RANS simulations were performed on a cluster using 350 threads. The LES mesh required more computational resources: it was decomposed into 2 000 zones of

approximately 60 000 cells, so the simulations ran on 2 000 threads.

IV.2.d Turbulence models

Both RANS and LES simulations were performed. The numerical schemes used in both cases are summarised in Table IV.2 and Table IV.3.

Table IV.2: RANS numerical scheme.

Mesh	Tetrahedral mesh	7 millions tetrahedra
Time scheme	Euler backwards	1st order implicit
Spatial discretisation	Convection	2nd order centered
	Diffusion	2nd order centered
	Pressure Solver	Conjugated gradient with SSOR preconditioning
Turbulence model	RANS	classical $k - \epsilon$
	Wall law	Reichardt law

Table IV.3: LES numerical scheme.

Mesh	Tetrahedral mesh	120 millions tetrahedra
Time scheme	Adams-Bashforth	2nd order explicit
Spatial discretisation	Convection	2nd order centered
	Diffusion	2nd order centered
	Pressure Solver	Conjugated gradient with SSOR preconditioning
Turbulence model	LES	WALE
	Wall law	Reichardt law

IV.2.e Boundary conditions

The boundaries are non-slip, adiabatic walls. The initial velocity is null, the flow is established in approximately two seconds. The initial temperature is 700°C on

the whole domain. For the sector mesh, symmetry boundary conditions are imposed on each side of the sector.

IV.2.f Source terms

The pump is modelled by a momentum source S_m above the heat exchanger, tuned to give a steady-state mass flow rate of $1170.46 \text{ kg}\cdot\text{s}^{-1}$ in each heat exchanger.

The heat exchanger is not explicitly modelled in the CAD model. Instead, the linear pressure loss in the heat exchanger zone is modelled by the Darcy-Weisbach equation (Equation III.2), with D a hydraulic diameter arbitrarily set to 8 mm, and Λ a Reynolds-number-dependent coefficient, equal to $0.316Re^{-0.25}$ (Blasius correlation [90]). Since the final design for the intermediate heat exchanger in the MSFR is not known yet, this very simple model is arbitrary and can be modified.

Thermal-hydraulic simulations of the MSFR were performed first, without neutronics. A power distribution was thus needed. It was modelled as a constant function with a spatial distribution taken from the PhD thesis of A. Laureau [55]. The total power was 3 GW, with the following distribution:

$$S_{th} = \left| 9.5 \times 10^8 \cdot \cos\left(\frac{\pi}{2} \cdot \frac{z}{H^*}\right) \cdot \cos\left(\frac{\pi}{2} \cdot \frac{r}{R^*}\right) \right| \quad (\text{IV.1})$$

With $H^* = 2.2\text{m}$ and $R^* = 1.4\text{m}$, and for $r < 1.2\text{m}$.

The power field corresponding to this distribution can be seen in Figure IV.5.

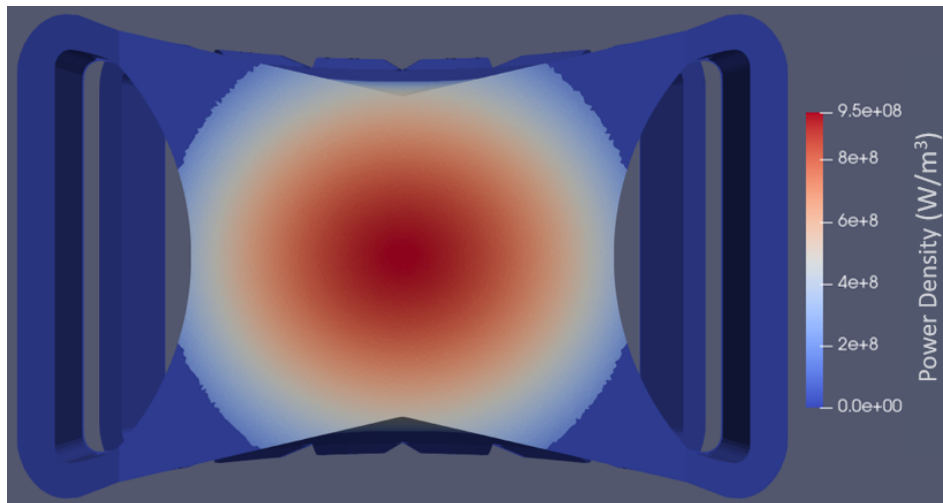


Figure IV.5: Power field used for pure thermal-hydraulic calculations.

The heat removal in the heat exchanger zone is modelled by a convective heat transfer function:

$$S_{exch} = h(T_{salt} - T_{ext}) \quad (\text{IV.2})$$

With T_{ext} varying between the bottom and top of the heat exchanger from 600°C to 750°C, and h taken arbitrarily very high ($10^7 \text{ W.m}^{-2}.\text{K}^{-1}$) to ensure that the salt temperature reaches 600°C at the end of the heat exchanger.

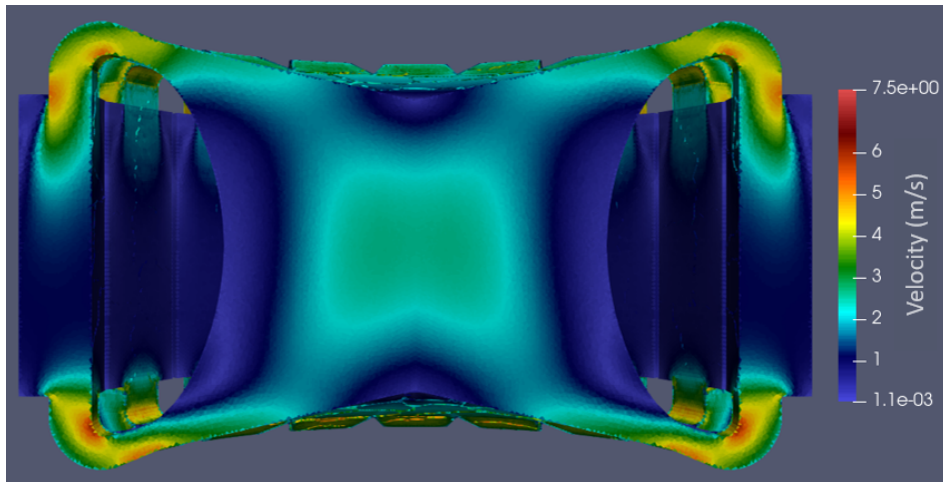
IV.3 RANS simulations on the MSFR

In order to test the thermal-hydraulic model and obtain useful parameters for the LES mesh (y^+ and λ_T), pure thermal-hydraulic RANS simulations were performed. The velocity and temperature fields for the RANS model described above are presented in Figure IV.6. Many different RANS studies were then performed, in order to evaluate the impact of different parameters on the results: namely the geometry used for the calculation, the heat exchanger modelling, the spatial scheme and the turbulent viscosity model.

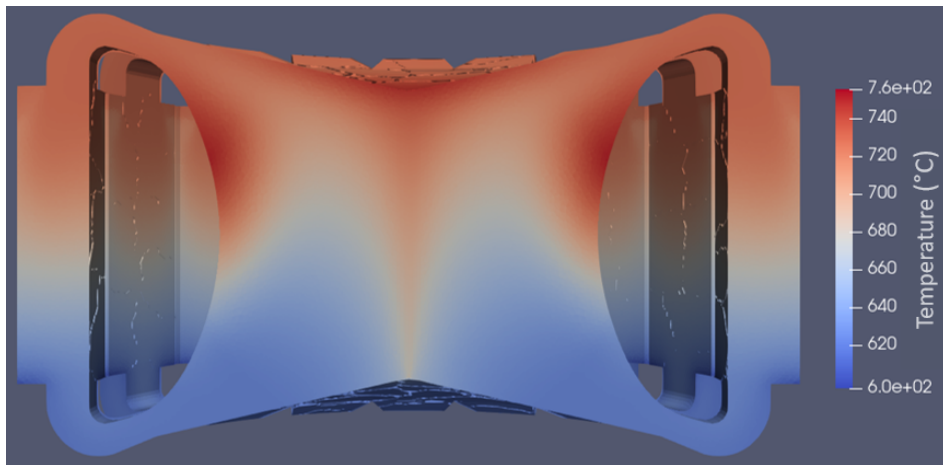
IV.3.a Impact of the geometry

First of all, the impact of the geometry considered was studied. The RANS simulations on the full core was compared to the same simulation, but performed on only a sector of the core with symmetry boundary conditions. The velocity and temperature fields for the sector are presented in Figure IV.7. The velocity and temperature fields at the equator were then plotted and compared for the two geometries. Results are presented in Figure IV.8.

The geometry considered has almost no impact for RANS simulations (the maximum difference is 4°C or 0.6 % between both temperatures at the center of the core). Since the RANS equations only model the mean fields, and the mean fields are expected to be the same for each sector, the boundary conditions applied do not disturb the flow. Symmetry boundary conditions are probably not ideal, periodic boundary conditions could potentially improve the results further by better representing the transverse flow between the sectors.



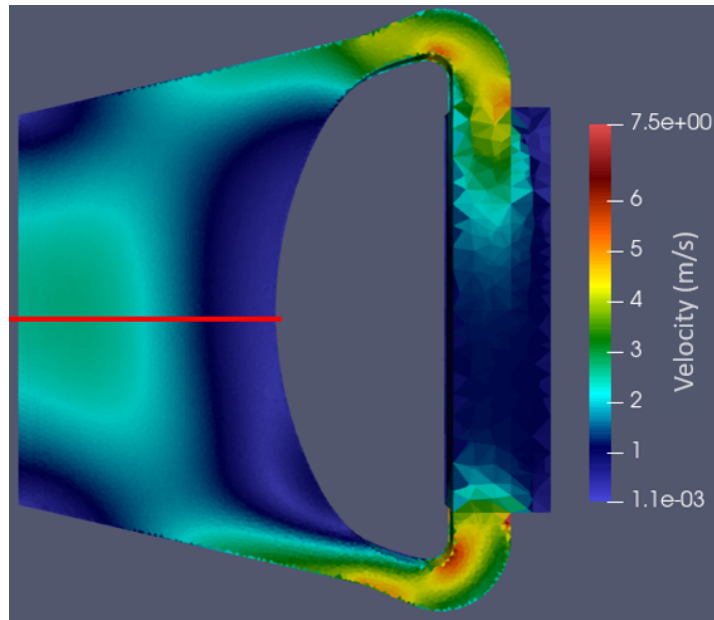
(a) Velocity field of the MSFR with RANS modelling.



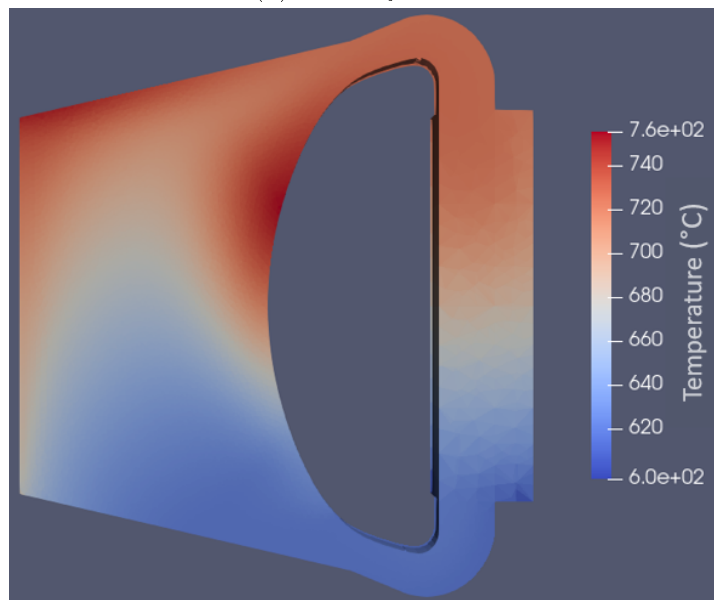
(b) Temperature field of the MSFR with RANS modelling.

Figure IV.6: RANS steady-state fields of the MSFR (full core).

Subsequent RANS studies were performed on a single sector of the MSFR, in order to speed up the calculations.

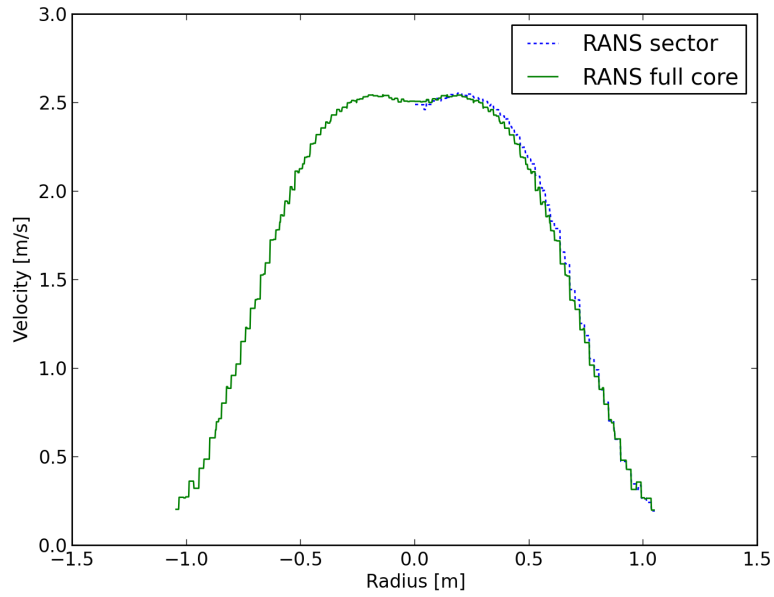


(a) Velocity field.

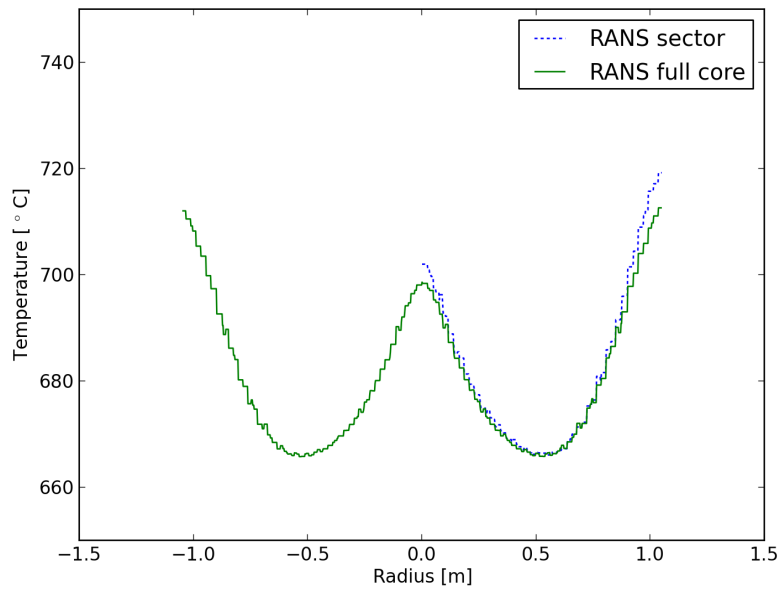


(b) Temperature field.

Figure IV.7: RANS steady-state fields of the MSFR (one sector). The equatorial line used for plots is shown in red.



(a) Velocity equatorial plots.



(b) Temperature equatorial plots.

Figure IV.8: Compared equatorial plots of the full core (solid green line) against one sector (dashed blue line) for the RANS model.

IV.3.b Impact of the heat exchanger modelling

Since the exact design of the heat exchangers of the MSFR is not yet known, the impact of the model used for the heat exchanger on the velocity field was studied next. The sector simulation presented above — with a pressure drop in the heat exchanger described in Section IV.2.f — was compared to a simulation on an "open" sector: the pump and heat exchanger block was completely removed and replaced by a set flow rate at the inlet of the critical zone — so the mass flow rate in both cases is the same. In order to prevent the thermal discrepancies, the energy equation was not solved for this simulation, only the momentum equations were computed. The velocity field for the open sector geometry is presented in Figure IV.9. The compared equatorial velocity plots are presented in Figure IV.10.

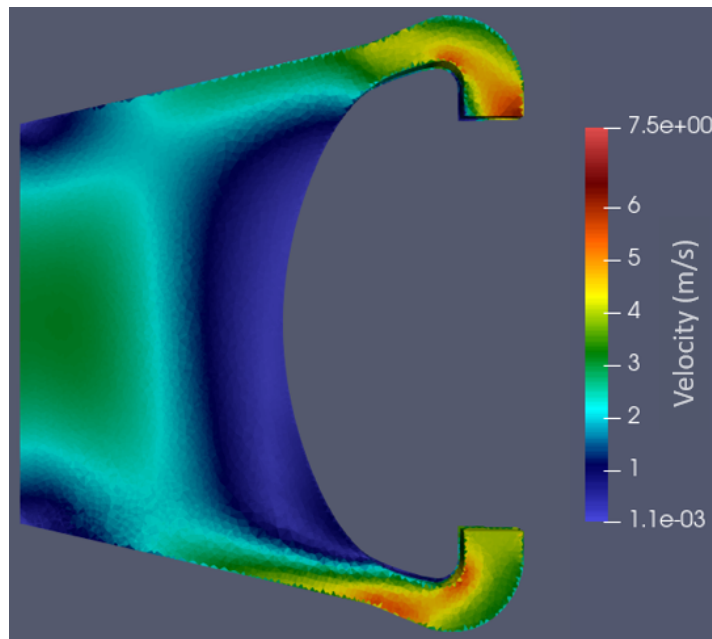


Figure IV.9: Velocity field for the "open" sector geometry.

The modelling of the heat exchanger has a significant impact on the velocity field (a difference of 17 % can be measured between both velocities at the center of the core). For this reason, in order to limit the potential variations due to the heat exchanger model — and to reduce the computation time — the subsequent RANS studies were performed on the "open" sector geometry.

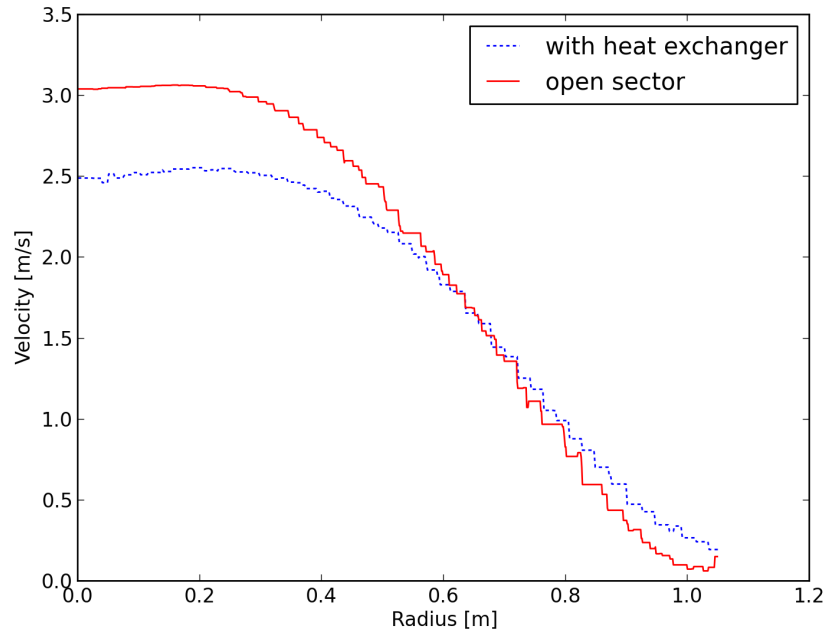


Figure IV.10: Velocity equatorial plots for the "standard" sector geometry (dashed blue line) and the "open" sector geometry (solid red line) with a coarse 25 mm mesh.

IV.3.c Mesh convergence on the open sector geometry

With RANS modelling, a mesh convergence study is necessary to determine the sufficient spatial resolution. Three different meshes were created with different edge sizes for the volume cells — the size of the cells on the surface mesh is set by the y^+ value and does not vary. Results are presented in Figure IV.11.

While the 25 mm mesh appears to be too coarse, no real discrepancy appears between the 10 mm and the 7 mm mesh. Therefore the 10 mm mesh was used for the subsequent studies.

IV.3.d Impact of the spatial scheme

Different orders were tested for the spatial numerical schemes. More specifically, a first-order scheme for the convection operator was compared to the second-order scheme used in the studies above. Results are presented in Figure IV.12.

A difference of 8 % can be measured between both velocities at the center of the core. A first-order scheme would probably converge towards the second-order solution

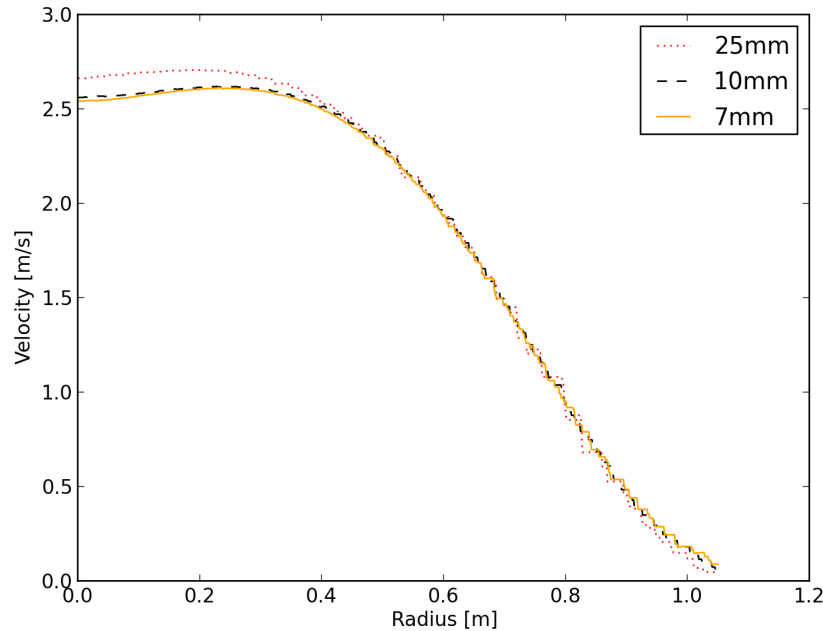


Figure IV.11: Mesh convergence study for the open sector geometry: 25 mm mesh (dotted red line), 10 mm mesh (dashed black line), and 7 mm mesh (solid orange line).

with a finer mesh. The second-order scheme — for which the mesh is fine enough, as shown in Figure IV.11 — was kept for the following studies.

IV.3.e Impact of the RANS model

The impact of the turbulent viscosity model used was then studied. The classical $k - \epsilon$ model (as described in Equation II.14) used above was compared to the more recent, realisable $k - \epsilon$ model [91]. The comparison between both models is presented in Figure IV.13.

Significant discrepancies are observed between both models (a difference of 15 % can be measured between both velocities at the center of the core). For this type of flow, the realisable model should give better results [91].

The best parameters for RANS simulations on the MSFR — with no heat exchanger — with TrioCFD are summed up:

- Geometry considered: Only one sector for faster calculations.
- Size of the surface mesh cells (set by the y^+ value): 25 mm.

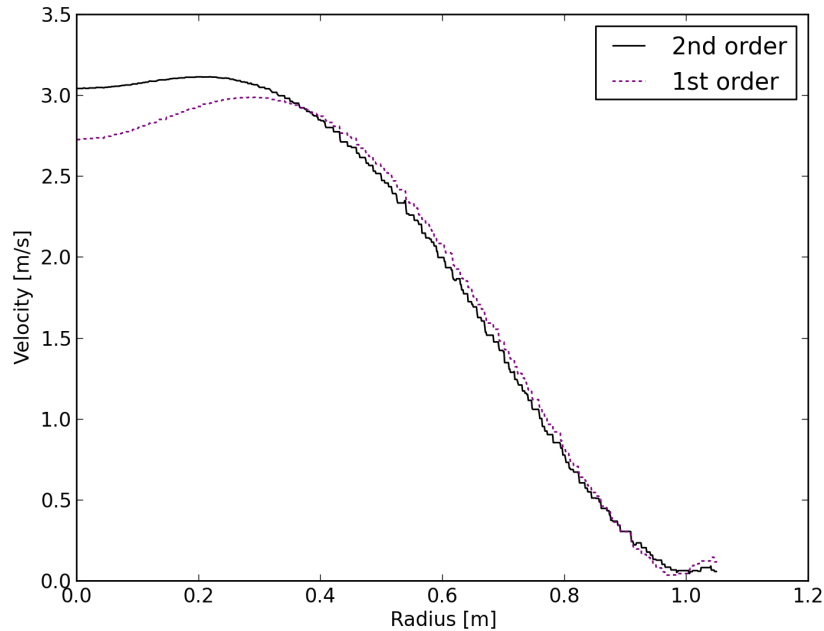


Figure IV.12: Velocity equatorial plots for a second-order scheme for the convection operator (solid black line) and a first-order one (dashed purple line).

- Size of the volume mesh cells (mesh convergence study): 10 mm.
- Order of the spatial scheme: second-order.
- turbulent viscosity model: realisable $k - \epsilon$ model.

IV.4 Numerical benchmark on the open sector

In order to compare the results given by TrioCFD with other CFD codes, the open sector geometry described above was used as a numerical benchmark. This benchmark was developed in collaboration with CNRS, Framatome, and Orano, and is the object of a soon-to-be-published article [92]. The set parameters of the benchmark are the following:

- The geometry used is the "open sector" geometry, with no pump nor heat exchanger.
- The fuel salt properties are the ones described in Table IV.1.

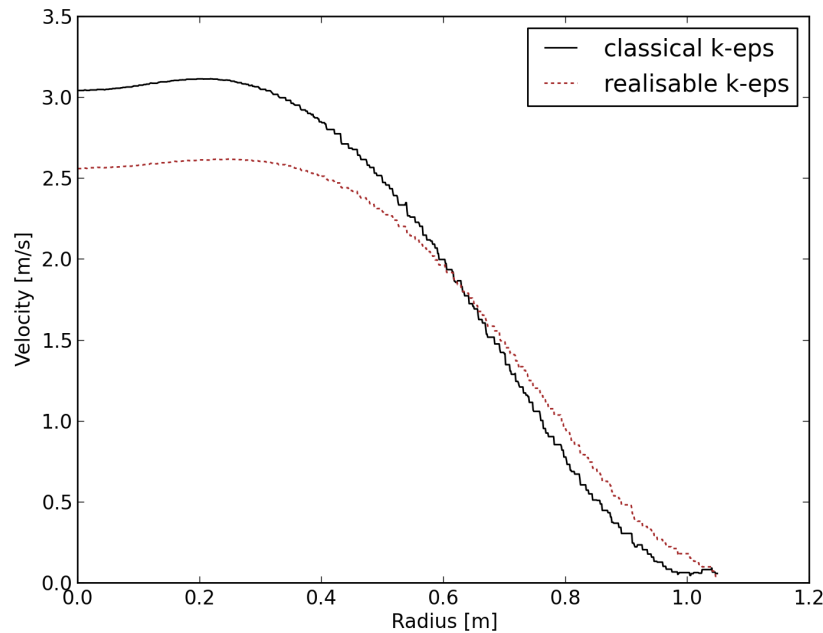


Figure IV.13: Velocity equatorial plots for the standard $k - \epsilon$ model (solid black line) and the realisable $k - \epsilon$ model (dashed brown line).

- Only the velocity and pressure equations are solved, there is no thermal nor concentration equations.
- The inlet velocity is imposed in order to have a mass flow rate of $1170.46 \text{ kg}\cdot\text{s}^{-1}$.
- The boundary conditions are symmetric on both "sides" of the sector, and no-slip walls elsewhere.
- The logarithmic law of the wall is used at every no-slip wall.
- The turbulence model is a RANS model: either the classical or the realisable $k - \epsilon$ models described above.
- The spatial discretisation can use a first or second order scheme.

Three other CFD codes were used on this benchmark and compared with `TricCFD`: `OpenFOAM`, `ANSYS Fluent`, and `STAR-CCM+`[®]. A rigorous comparison between these codes would require to use the same mesh for every code. Unfortunately, this raises two problems:

- **TrioCFD** currently only handles tetrahedral meshes for RANS simulations with a $k - \epsilon$ model. The other codes can use more optimised meshes, combining different types of cells.
- Even if every code used the same tetrahedral mesh, the results would differ due to different spatial discretisations. **TrioCFD** places the unknowns in the center of the faces of a cell, instead of the center of the cell like the other codes. This allows **TrioCFD** simulations to converge on coarser meshes than other codes, but complicates the comparison between codes.

For these reasons, every code used its own optimised mesh, and results were compared using different meshes.

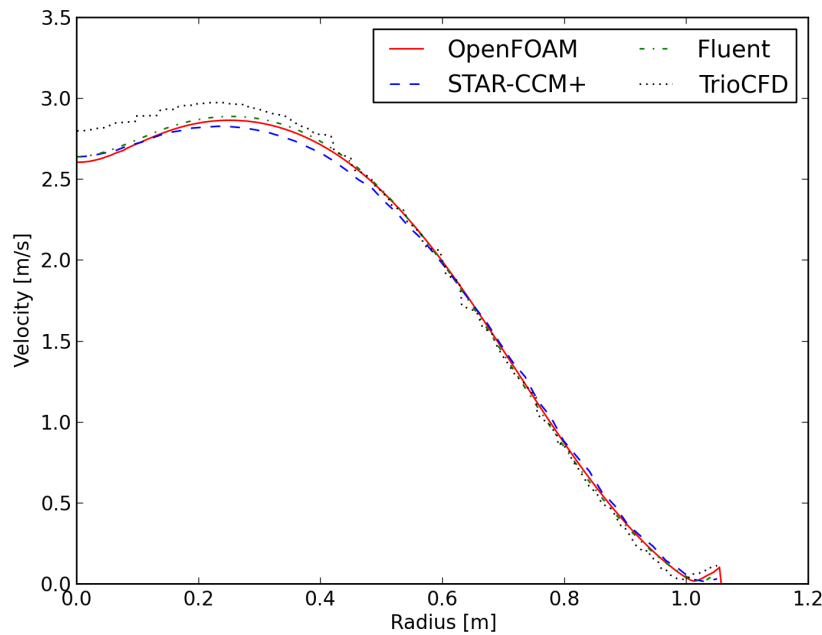


Figure IV.14: Velocity equatorial plots for the different codes (each using its own mesh) on the MSFR benchmark, for a classical $k - \epsilon$ model.

For a classical $k - \epsilon$ model, the different codes are in good agreement in the outer part of the core (radius between 0.5 and 1.), although the results are more dispersed in the central part of the core (radius between 0. and 0.5): the results from **TrioCFD** especially present a higher velocity than the other codes, as well as a less pronounced velocity gradient between 0. and 0.2 m. (Figure IV.14).

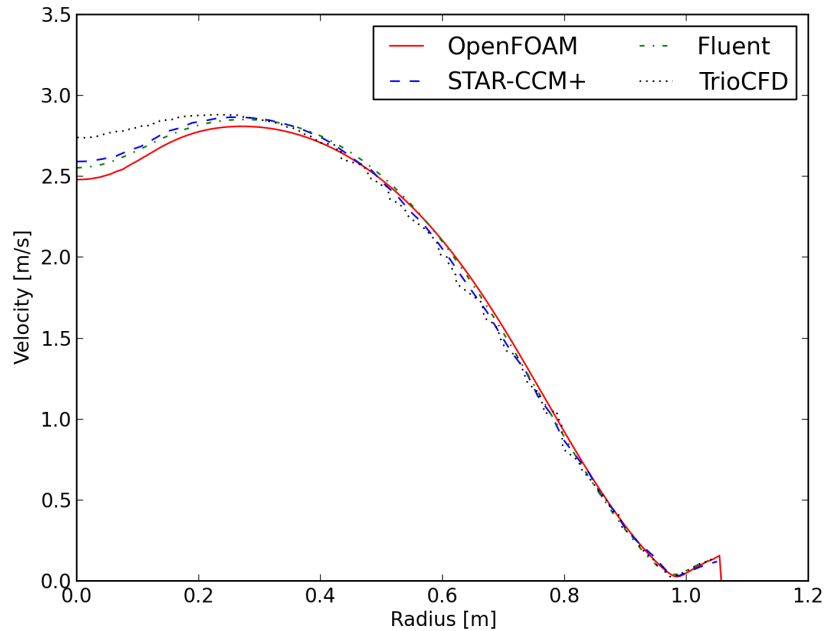


Figure IV.15: Velocity equatorial plots for the different codes (each using its own mesh) on the MSFR benchmark, for a realisable $k - \epsilon$ model.

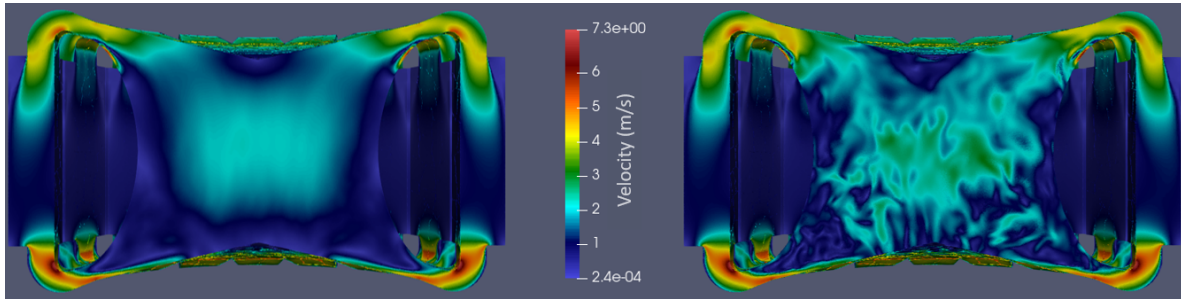
For a realisable $k - \epsilon$ model, while the different codes are once again in good agreement in the outer part of the core (radius between 0.5 and 1.), the results are more dispersed in the central part of the core (radius between 0. and 0.5): a pronounced velocity gradient between 0. and 0.3 m appears on the `OpenFOAM` results; the gradient is a bit lower on the `Star-CCM+`[®] and `Fluent` plots, and the velocity profile in this region is almost flat on the `TrioCFD` plot. (Figure IV.15).

Being limited to tetrahedral-only meshes is currently the biggest constraint regarding mesh optimisation — especially regarding the surface mesh — but the fast development of the PolyMAC discretisation in `TrioCFD`, that could handle all types of meshes, could soon eliminate this difficulty [93].

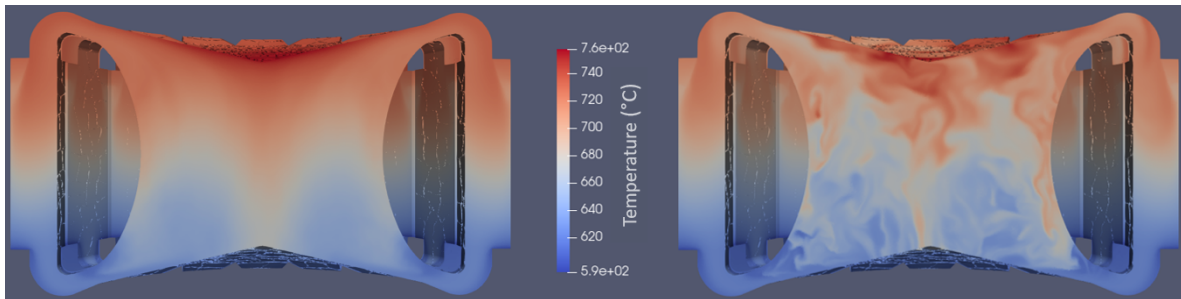
IV.5 LES simulations on the MSFR

In order to study the turbulent fluctuations in the MSFR, LES calculations are necessary. Using the parameters described above (see Section IV.2), an LES calculation was performed on the whole core of the MSFR. Instantaneous and mean fields are

presented in Figure IV.16.



(a) Mean and instantaneous velocity fields.



(b) Mean and instantaneous temperature fields.

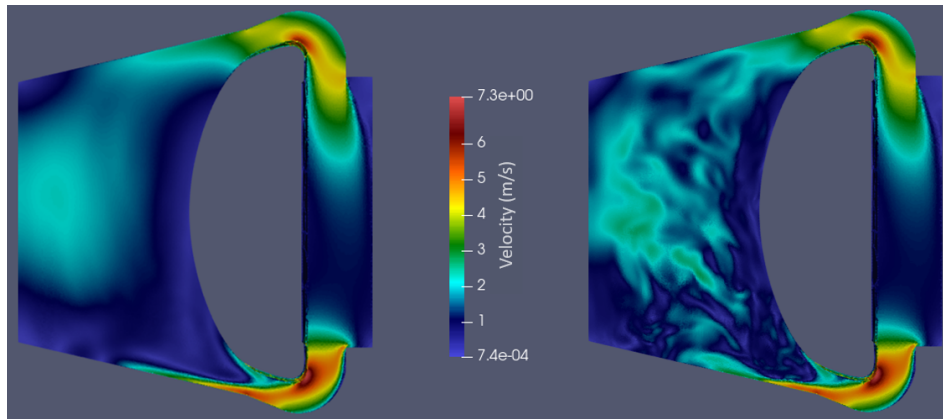
Figure IV.16: LES mean and instantaneous fields of the MSFR (full core).

If the mean fields are somewhat similar to the RANS fields, the instantaneous fields reveal many eddies in the whole critical region.

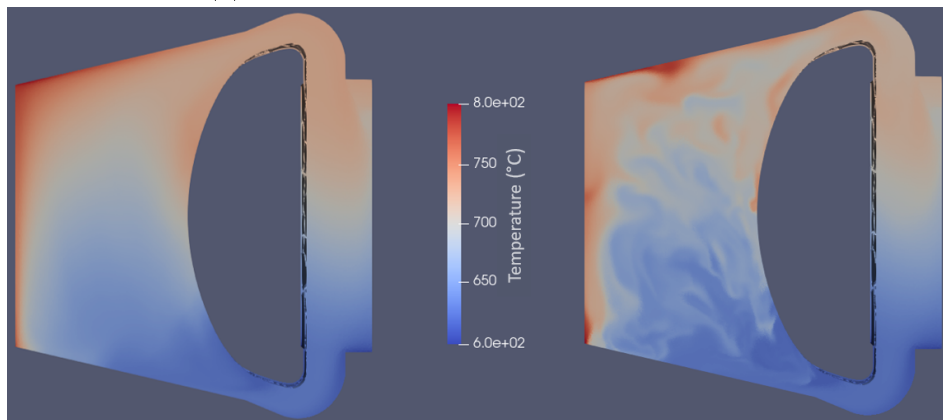
IV.5.a Impact of the geometry

Like for the RANS simulations, the impact of the geometry was tested. The full core simulation presented above was compared with a simulation performed on one sector of the core, using symmetry boundary conditions. The velocity and temperature fields for the sector geometry are presented in Figure IV.17. Equatorial plots of the mean fields for both cases are compared in Figure IV.18.

Important discrepancies between both cases are observed: a difference of 5 % can be measured between both velocities at the center of the core, that goes up to an 8 % difference when comparing the temperatures in the center of the core. Since the instantaneous fields in LES are not symmetric for a symmetric geometry (see Figure IV.16), the symmetric boundary conditions heavily disturb the flow and the eddies formation near the boundary conditions. These disturbances on the instantaneous fields



(a) Mean and instantaneous velocity fields.

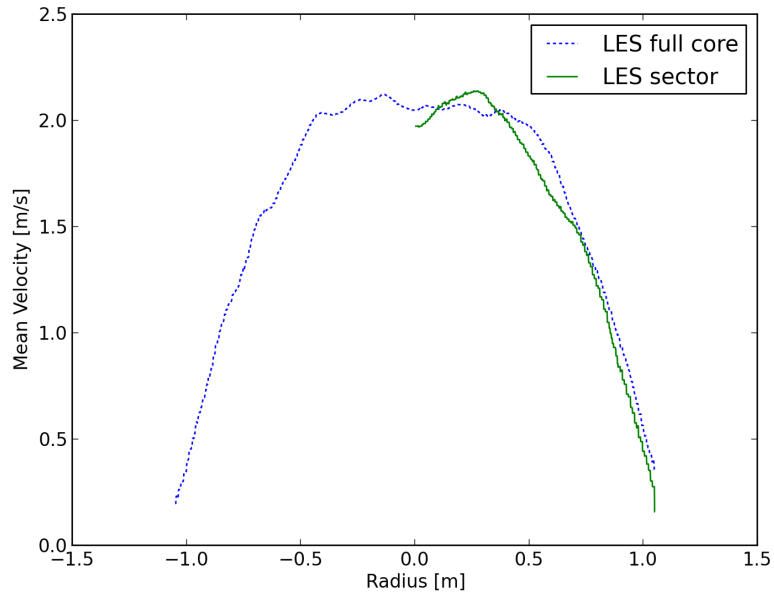


(b) Mean and instantaneous temperature fields.

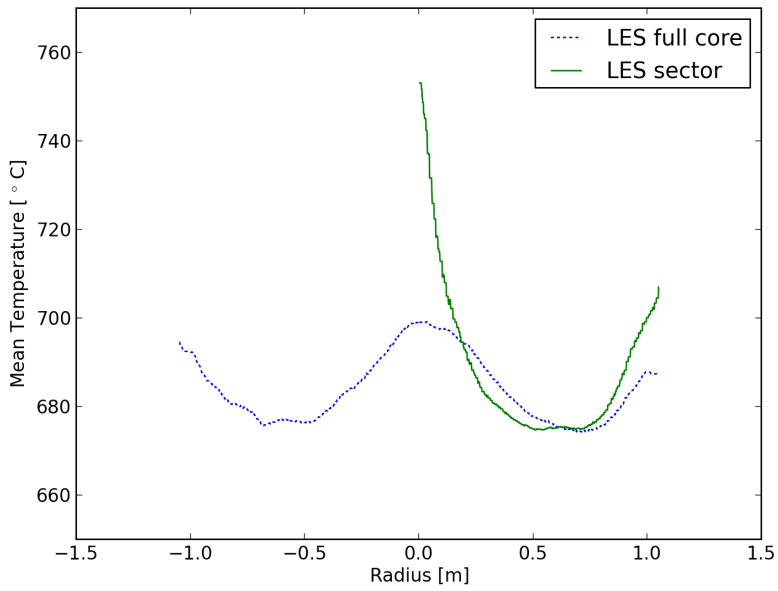
Figure IV.17: LES mean and instantaneous fields of the MSFR (one sector).

impact the mean fields as well. LES simulations with symmetric or periodic boundary conditions are therefore not recommended, the whole core should be used.

It should also be noted that the simulations are not completely converged: the mean fields for the whole core case should be "more" symmetric — assuming the mesh is symmetric, which is not the case, the mean fields for a symmetric problem should converge towards a symmetric solution — which is not quite the case in Figure IV.18. With a longer simulation, the mean fields should become more symmetric and the discrepancies between both geometries could be lower — especially regarding the temperature fields, which are longer to converge. The simulations performed in this study were stopped after 15 s of computed time, which corresponded to the available cluster time for this study (1.5 mega CPU-hours, or MCPUh).



(a) Mean velocity plots.



(b) Mean temperature plots.

Figure IV.18: Compared equatorial plots between the full core geometry (dashed blue line) and the sector geometry (solid green line).

IV.5.b Comparison with RANS simulations

The mean fields for the LES simulations were then compared with the RANS fields, in order to measure how much of an approximation is the RANS modelling on this case. The compared equatorial plots are presented in Figure IV.19.

The mean fields in LES are "flatter" than in RANS: this is probably caused by the increased turbulence, which mixes more the flow in the critical region. However, if we look at the instantaneous fields instead of the mean fields, turbulent fluctuations cause important local temperature gradients.

IV.5.c Turbulent fluctuations in the MSFR core

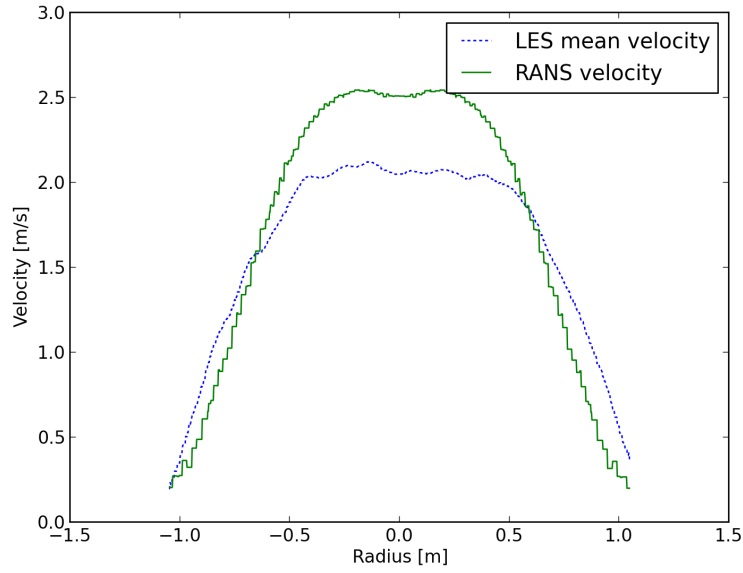
Figure IV.20 shows equatorial plots of the instantaneous fields for the LES simulation on the full MSFR core. It reveals strong local temperature gradients: up to 20 °C per 10 cm in the center of the critical region, and around 10°C per 10 cm closer to the walls — 10 cm is the reference length for neutronics, as it is the fast neutron mean free path.

In order to observe time fluctuations caused by turbulence, probes were set in different places of the core, and the instantaneous temperature field was recorded at these locations. Figure IV.21 shows the evolution of the temperature in the center of the core. The flow takes two seconds to develop, so the times before 2s were removed from the plot. Temperature fluctuations of about $\mp 20^\circ\text{C}$, or $\mp 3\%$, can be measured, but the signals are hard to study as they are.

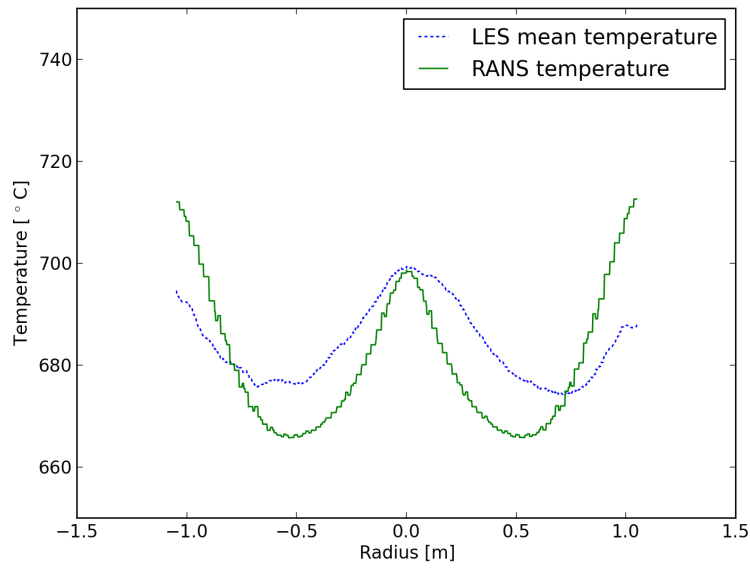
Using the Fourier transformation [94] on the probes signals, a spectrum can be computed. The time spectrum of the temperature probe is shown in Figure IV.22. Specific modes do not emerge clearly: a great variety of modes up to 5 Hz can be seen. Yet this spectrum can be used to filter the probes readings.

By cutting the frequencies above 5 Hz and applying an inverse Fourier transformation, the probes readings are a bit easier to analyse (see Figure IV.23): temperature time fluctuations can be estimated at about $\mp 20^\circ\text{C}$ with a speed of $100^\circ\text{C}\cdot\text{s}^{-1}$ in the center of the critical region.

Such spatial and time fluctuations of the temperature field should have a massive impact on the neutronic behaviour of the core, and thus the power distribution. The question that remains is then, will the power fluctuations dampen the temperature fluctuations, or will some resonances could appear which would increase further these fluctuations? To answer this question, a neutronic model of the MSFR is needed first.

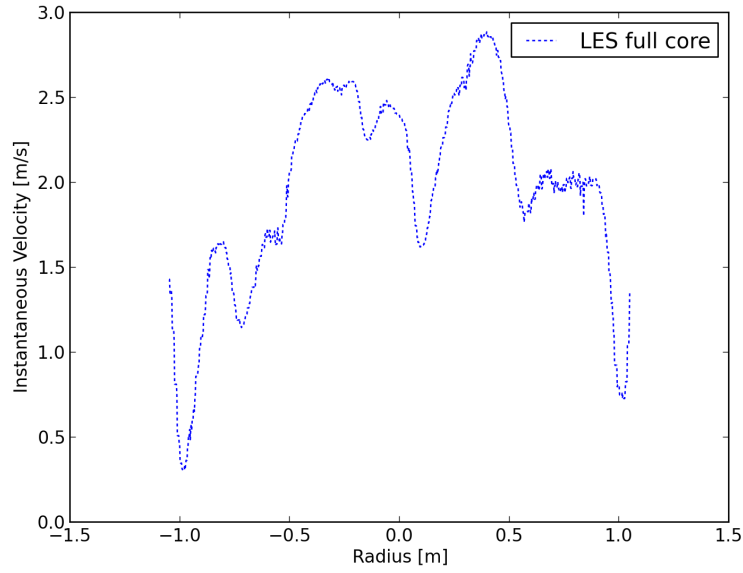


(a) Mean velocity plots.

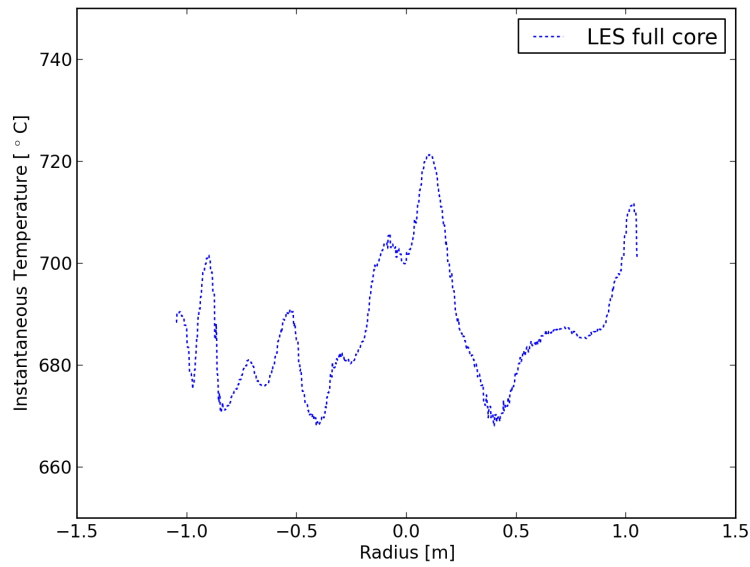


(b) Mean temperature plots.

Figure IV.19: Compared equatorial plots between the LES calculation (dashed blue line) and the RANS calculation (solid green line).



(a) Instantaneous velocity plot.



(b) Instantaneous temperature plot.

Figure IV.20: Spatial fluctuations in the MSFR: equatorial plots of the LES instantaneous fields (full core simulation).

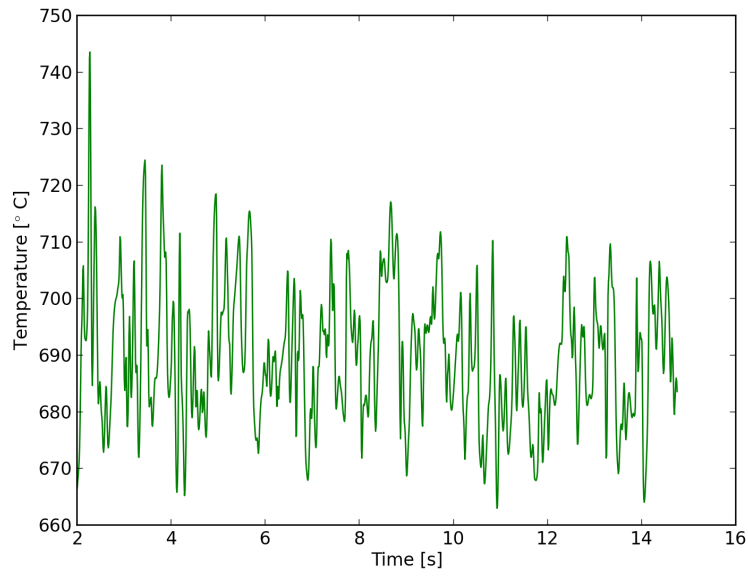


Figure IV.21: Time fluctuations in the MSFR: temperature evolution in the center of the core; times before 2 s are removed because the flow is not developed.

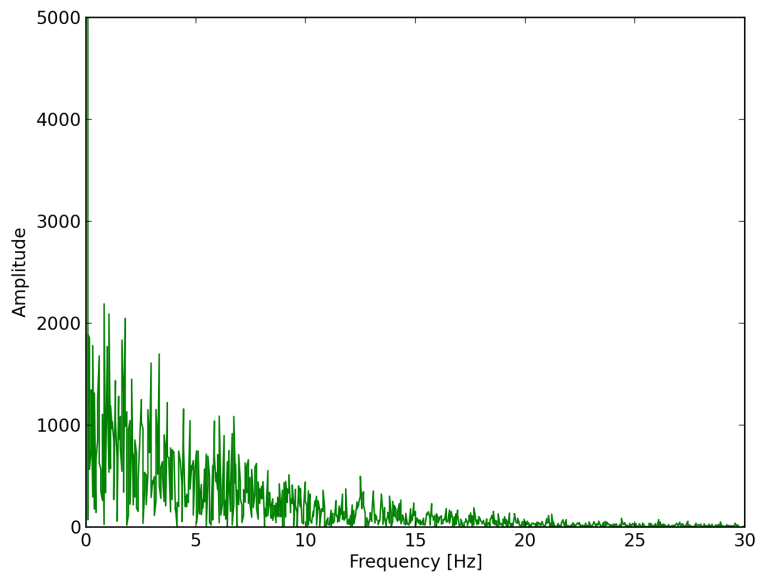


Figure IV.22: Temperature spectrum in the center of the core of the MSFR.

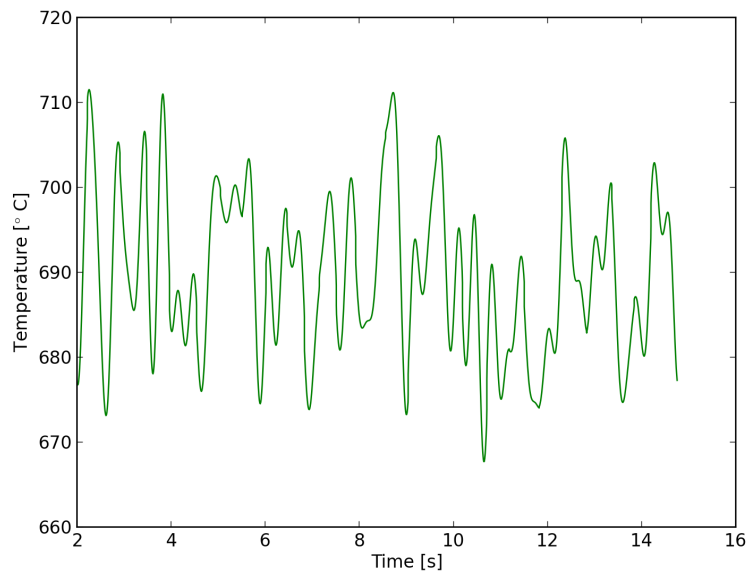


Figure IV.23: Time fluctuations in the MSFR: temperature evolution in the center of the core (high frequencies filtered out).

IV.6 Neutronic model of the MSFR

IV.6.a Lattice calculation

The model used for the lattice calculation is rather coarse. Compared to the ARE, where the comparison with experimental data required a fine model, for the study of power fluctuations a more simplified model can be used. The mesh used for the lattice calculation is presented in Figure IV.24. It is a two-dimensional, 3 m side square with vacuum boundary conditions, composed of three materials:

- The fuel salt, composed of ^{232}Th , ^{233}U , ^7Li and F as described in Section IV.1.a.
- The fertile blanket, with the same composition as for the fuel salt, except that all the ^{233}U is replaced by ^{232}Th .
- The reflector, composed of a nickel-based alloy without impurities (Ni–Cr–W).

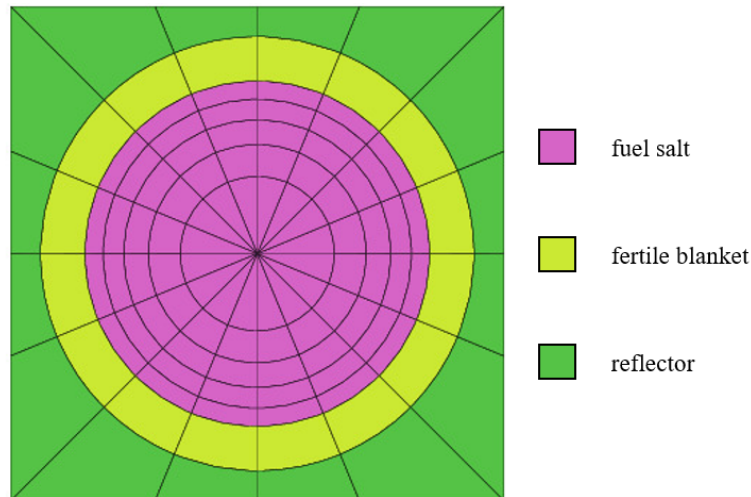


Figure IV.24: Mesh used for the MSFR lattice calculation.

A 6 energy groups mesh was used. The only temperature parameter is the salt temperature, so the computed cross sections do not depend on the blanket and reflector temperatures.

IV.6.b Core calculation

The neutronic core model of the MSFR is necessarily different from the thermal-hydraulic one: the reflectors and the fertile blanket must be represented, but the heat exchangers can be removed — their final design is not yet known, but almost no fission will occur in them. The mesh used (composed of 500 000 tetrahedras) is presented in Figure IV.25. The mesh size is set to 10 cm in the fuel salt, which is the typical mean free path for fast neutrons. A coarser mesh size (50 cm) is used for the reflectors and the fertile blanket. Vacuum boundary conditions are applied outside of the domain. The S_6 angular discretisation is used (48 different directions).

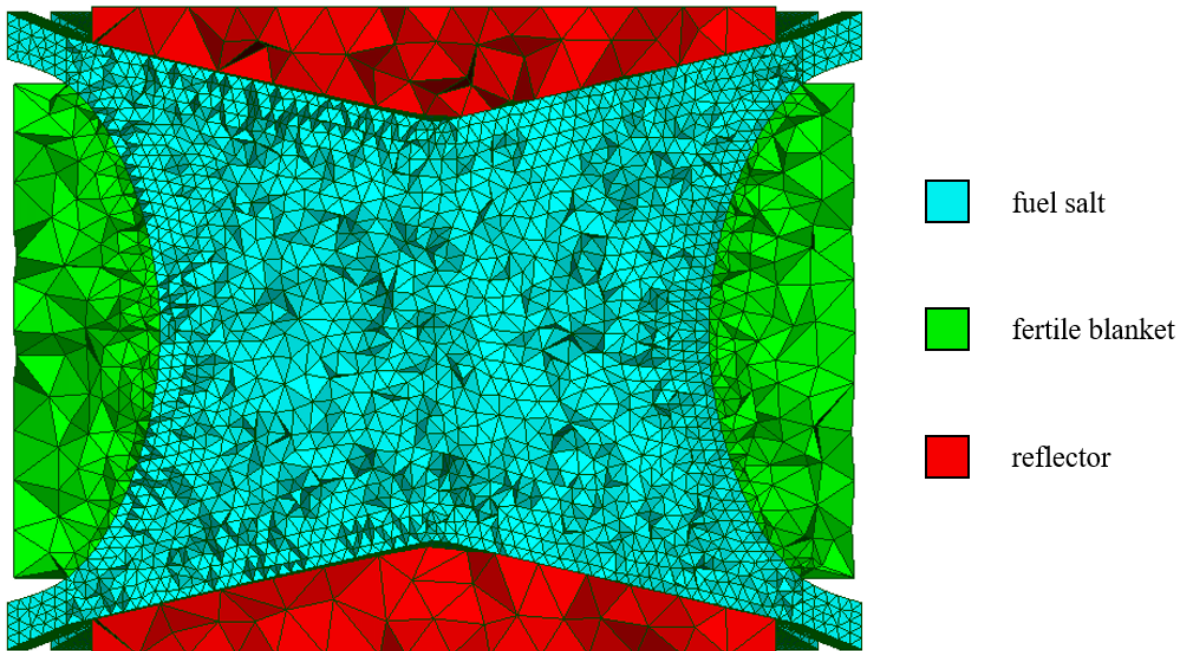


Figure IV.25: Mesh used for the MSFR core calculation (500 000 tetrahedras).

IV.6.c Neutronic simulation: power distribution

A pure neutronic calculation was performed with a uniform temperature (700 °C) and immobile precursors in order to compute the power distribution. The power density fields obtained is shown in Figure IV.26. The total power is set to 3GW.

The computed power distribution appears more centered than the correlation used in the thermal-hydraulics calculations (Figure IV.5). Compared equatorial and

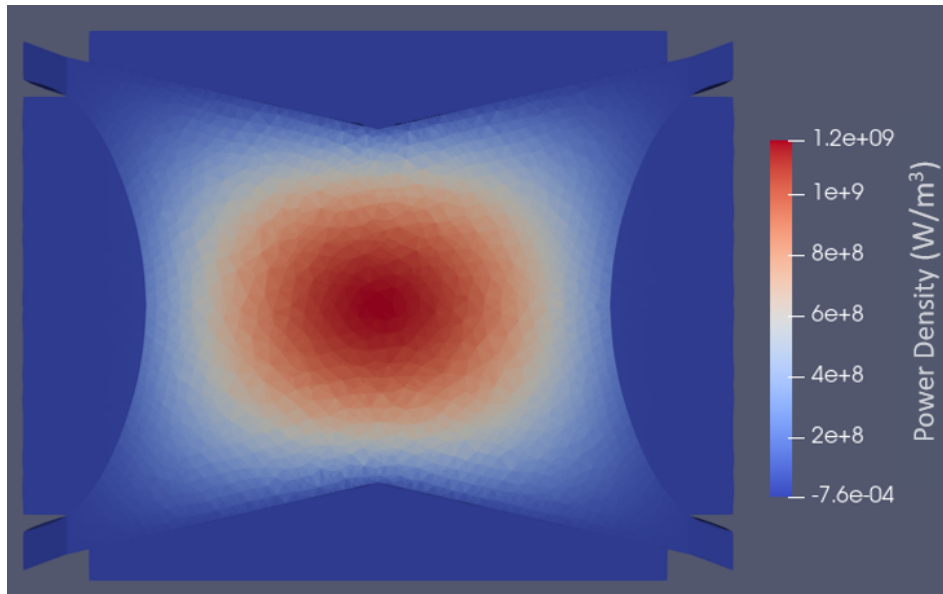


Figure IV.26: Power density field for a uniform 700 °C temperature.

vertical plots of both power distributions reveal differences up to 20% in the center of the core (see Figure IV.27).

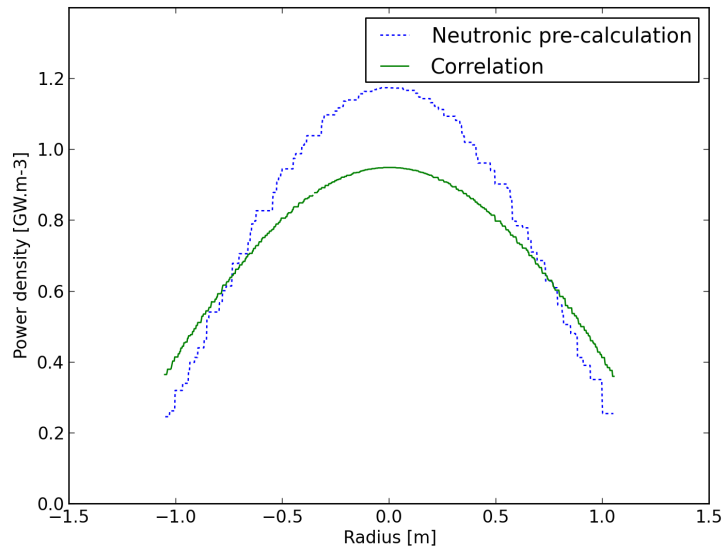
The next step is to couple both models and to run a coupled steady-state calculation, starting with the fields from the pre-calculations.

IV.7 Coupled simulations on the MSFR

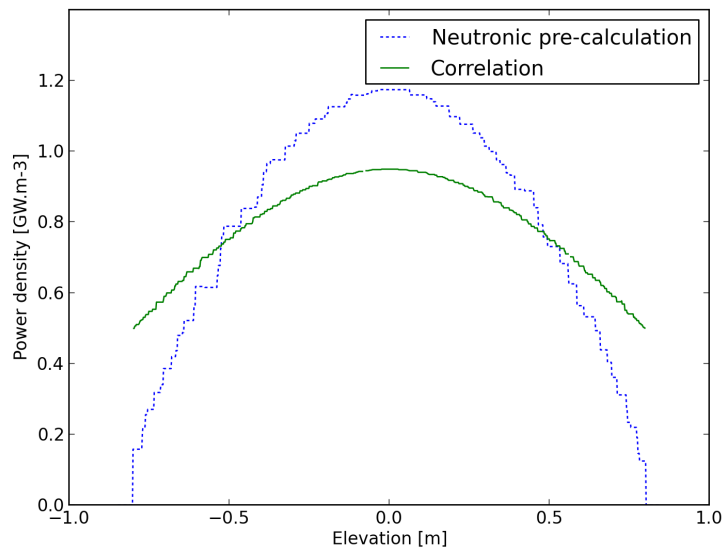
IV.7.a Delayed neutrons precursors modelling

For the coupled calculations, the precursor source fields should be computed by APOLL03[®] and sent to TrioCFD, which would compute and send back the precursor concentration fields — just like in the ARE case. For the MSFR case however, which has a much higher computation time than the ARE, this is not currently feasible. This is because the steady-state Boltzmann equation for MSRs (Equation I.39) has been implemented recently in APOLL03[®], and is not yet optimised. Solving the equation for the MSFR, starting from a uniform neutron flux and temperature field and null precursor concentration fields, takes about 10 days (with a parallelisation on the directions, so using 48 threads).

If the precursor transport is neglected, the standard steady-state Boltzmann equation (Equation I.10) can be computed instead, through optimised methods. For



(a) Equatorial power plots.



(b) Vertical power plots.

Figure IV.27: Compared equatorial (top) and vertical (bottom) plots of the power density between the neutronic pre-calculation and the correlation used for thermal-hydraulic calculation.

the MSFR, starting from the same initial state, the computation takes a few minutes on 48 threads, which represents a speedup of several thousands. For this reason, the

precursors were not modelled in our thermal-hydraulic model of the MSFR, and were assumed immobile in the neutronic calculation.

IV.7.b Coupled steady-state of the MSFR

A coupled steady-state simulation was performed on the full core geometry. In order to reduce the computation time of the thermal-hydraulic simulation, the thermal-hydraulic mesh was degraded — the reference size was set to 2.5 cm, like for the RANS mesh — and the heat exchangers simplified to canals with no enlargements, which reduced the number of cells by a factor 20. The initial thermal-hydraulic fields are the previously computed LES fields (see Section IV.5), projected on this degraded mesh. We are thus performing an under-resolved LES (also called Very Large Eddy Simulation, or VLES). Because of this degrading of the mesh, we cannot compare the thermal-hydraulic fields between the steady-state coupled calculation and the LES pre-calculation.

It should also be noted that since we are solving the steady-state Boltzmann equation in the neutronic calculation, the total power is set and cannot vary. Only variations of the power distribution can be observed. For these reasons, the results of the coupled steady-state simulation were very close to the independent neutronic pre-calculation. Compared equatorial and vertical plots of the power distribution between the coupled calculation and the neutronic pre-calculation are shown in Figure IV.28.

We can see there is almost no difference between the radial distributions. However, the vertical distribution of the coupled calculation is slightly offset: this is because compared to a uniform temperature field, the steady-state temperature field is hotter near the top of the core and cooler towards the bottom, which causes the power distribution to shift towards the bottom of the core through the temperature feedbacks.

Another interesting plot is the compared temperature fields between the thermal-hydraulic and the neutronic mesh (Figure IV.29): as the temperature field computed on the thermal-hydraulic mesh is projected on the coarser neutronic mesh, the smaller modes "disappear". Still, important local temperature gradients remain on the neutronic mesh, which will impact the transient behaviour of the neutron flux.

In order to observe the power turbulent fluctuations and their impact on the temperature field, a coupled transient calculation would be necessary.

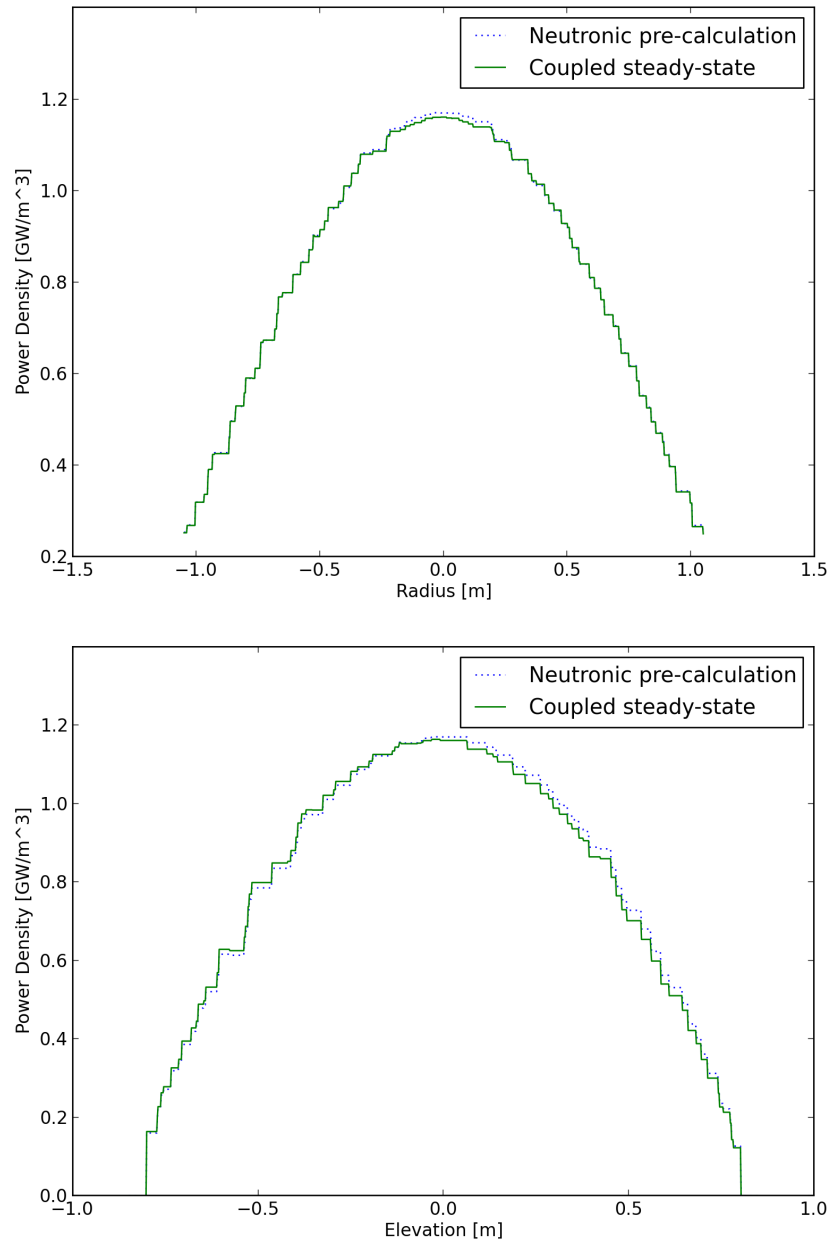


Figure IV.28: Compared equatorial (top) and vertical (bottom) plots of the power distribution between the neutronic pre-calculation (dotted blue line) and the coupled calculation (solid green line).

IV.7.c Coupled transient simulations on the MSFR

Starting from the coupled steady-state fields, and after having performed a critical calculation on the neutronic model to adjust the k_{eff} value (see Section II.1.e), a

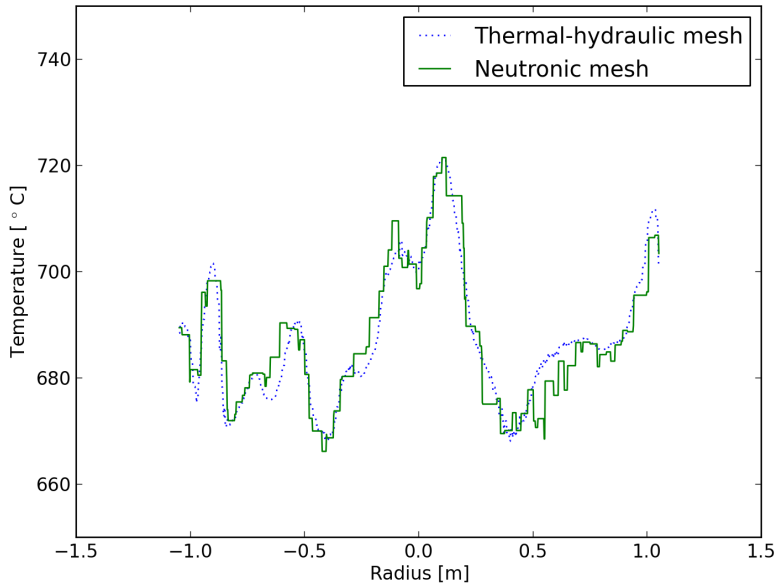


Figure IV.29: Compared equatorial plots of the temperature field, on the thermal-hydraulic mesh (dotted blue line) and the neutronic mesh (solid green mesh).

transient coupled calculation was performed with a timestep before exchange of 10^{-3} s — assuming immobile precursors. No perturbation was applied, the turbulent fluctuations of the temperature field would be sufficient to generate power fluctuations.

Unfortunately, even on a degraded thermal-hydraulic mesh, the computation takes too long to obtain meaningful results. Only 10^{-2} s of transient were computed within two days of computation.

Massive gains could be achieved by better parallelizing the problem however: currently, while the APOLL03[®] computation uses 48 threads (one for every direction of the S_6 angular discretisation) on the same core, TrioCFD also uses only one core with no domain decomposition to facilitate fields exchanges between both codes. This drastically slows down the thermal-hydraulic calculation: while one timestep in APOLL03[®] takes about 700 s to compute (on 48 threads), the same timestep in TrioCFD takes about 22 000 s on the degraded mesh. Using the domain decomposition in TrioCFD is thus necessary for transient simulations, but requires the development of a tool that handles exchanges between decomposed TrioCFD fields and non-decomposed APOLL03[®] fields. Such a tool — called a Data Exchange Channel, or DEC — has recently been developed in the C3PO coupling library, and should be implemented and tested on the MSFR case.

Once the problem is properly parallelized, if we want to use the non-degraded `TrioCFD` mesh for a well-resolved LES, a supercomputer should be used — the LES steady-state presented in Section IV.5 required about 1.5 MCPUh on 2000 threads. This would require some development, in order to install the different codes required for the simulation on the supercomputer, and probably a few MCPUh to compute a few seconds of coupled transient.

In order to compute coupled transient simulations for turbulent fluctuations assessment on a "smaller" environment than a supercomputer, we designed a simpler, faster-to-compute toy model that would partly reproduce the MSFR behaviour, with a non-degraded thermal-hydraulic model. Computations are still ongoing on this toy model, which is presented in Annex B.

In this chapter, we created a numerical model of the Molten Salt Fast Reactor (MSFR). Using `TrioCFD`, RANS simulations were performed in order to study the sensitivity of the model to different parameters, and to compare the `TrioCFD` results with other CFD codes. LES simulations were performed in order to assess the amplitude of the spatial and time fluctuations of the temperature field without any neutronic feedback. A neutronic simulation was performed in order to obtain the power distribution in the MSFR for a uniform temperature field. A coupled steady-state calculation on a degraded thermal-hydraulic mesh was performed, in order to prepare transient computations. These transient simulations were too computationally expensive to run on a sufficient duration. With some developments and the use of a supercomputer, coupled transient simulations on the MSFR should be performed shortly.

Conclusion and perspectives

Molten salt reactor projects are quickly developing, and the demand for numerical studies on MSR concepts is growing. Specific tools are being developed to model and reproduce the particular behaviour of MSR cores. In CEA, the APOLL03[®] – TrioCFD coupling has been adapted for precise simulations of MSR cores. This multi-physics code could model the coupled turbulent fluctuations of the power and temperature fields in an MSR core, a topic that has not been studied much yet — although it is the object of recent work [64, 71]. The objective of this thesis was to model the turbulent fluctuations in a reference MSR concept, the Molten Salt Fast Reactor, using the APOLL03[®] – TrioCFD code.

The first part of this work was to validate the APOLL03[®] – TrioCFD coupling on an experimental case. A numerical model of the Aircraft Reactor Experiment was thus developed. Despite the uncertainties regarding the exact materials' compositions and the simplifications made on our numerical model (the flows were treated as one-dimensional in open loops) the modelled ARE nominal state was very close to the actual ARE — the biggest difference being a 5 % difference for the liquid sodium temperature.

Measures of β_{eff} and its variation with the fuel flow rate also showed good agreement between the simulated and experimental data — the 7 % difference at null flow rate remains yet to be explained.

Two transient experiments were also reproduced (experiments H-8 and H-14), and once again the simulated results were close to the experimental ones. The main problem regarding the transient simulations was that all the simulations stopped between 50 and 60 s of simulated time, for reasons that remain to be explained and solved.

Solving this issue and performing longer transient simulations — as well as improving the modelled sodium flow — should improve even further our results. Still, the results obtained at this stage were satisfactory and contributed to the validation of

the APOLL03[®] – TrioCFD code.

The second and main part of this thesis was to model the MSFR. Many simulations were performed on the thermal-hydraulic model of the MSFR — as the turbulent fluctuations result from the turbulent velocity field in the core, which has to be precisely computed.

Different sensitivity studies were first performed, using a RANS approach to turbulence modelling. These sensitivity studies helped assessing the best parameters to use for RANS and LES simulations on the MSFR, and should also help making modelling choices for future MSRs studies. The results of these RANS simulations are also being compared with other CFD codes through a numerical benchmark, in collaboration with other partners [92].

LES simulations were then performed, with no neutronic coupling. Time and space fluctuations of the temperature field, caused by turbulence, were measured. Time fluctuations of the temperature in the center of the core was estimated at $\mp 3\%$, with no coupling.

A neutronic model of the MSFR was then realised, in order to compute the power distribution and to prepare the coupling. The precursor transport was neglected in this model, because the calculation with no precursor transport was several thousand times faster to converge than the full calculation.

Both models were then coupled for steady-state calculations. Computation time was a big issue for the coupled simulations, especially because the coupled calculation could not be as well parallelized as the pre-calculations. The thermal-hydraulic mesh was degraded, which prevented the comparison of the thermal-hydraulic fields between the coupled steady-state simulation and the LES pre-calculation. The neutronic fields however were compared, which revealed a slight shift of the power distribution towards the lower part of the core, where the temperature is cooler.

A coupled transient simulation (with no perturbations) was performed, but the very high computation time (about 2500 CPUh for 10^{-2} s of simulated time) prevented us from obtaining meaningful results.

Reducing the computation time of this calculation should be our priority for future studies. The first step would be to better parallelise our problem. A Data Exchange Channel (DEC) protocol has been recently implemented in C3PO, that would enable decomposed fields in TrioCFD to be exchanged with non-decomposed fields in APOLL03[®]. This protocol should be implemented and tested on the MSFR case, as

using domain decomposition in `TrioCFD` will greatly reduce the computation time of thermal-hydraulic timesteps, and thus of the whole calculation.

Currently, the neutronic timesteps are quite fast to compute, because the precursor transport is neglected. In order to perform coupled simulations with precursor transport, the neutronic calculation needs to be optimised. Such a large computation time difference between both calculations (with and without precursor transport) most likely result from optimisation issues with the recently-developed numerical methods for calculations with precursor transport. However, even after optimisation, the calculation with precursor transport should take a longer time than without, because there are more equations to solve. One way to further speed up the neutronic calculation, especially for big domains like the MSFR, would be to use domain decomposition in `APOLL03`[®]. While it is complicated with S_N angular discretisations, it is easier with P_N methods. In particular, the `NYM0` solver in `APOLL03`[®] uses a P_N angular discretisation and supports domain decomposition. Promising results with strong speedups were obtained for parallelized lattice calculations, but the solver still has to be implemented for core calculations [95].

In order to assess the thermal stress and neutron fluence exercised on the vessel, the turbulent fluctuations near the wall would need to be precisely modelled. This would require to perform LES simulations with no wall laws and very small cells near the wall. The biggest issue with small cells near the wall is the impact it has on the stable timestep for an explicit time scheme. Using an implicit scheme would solve this issue, but cause other likely issues of memory use for a domain as big as the MSFR core. A solution would then be to use an hybrid Implicit-Explicit (IMEX) time scheme, where an implicit time scheme would be used on the small cells near the walls in order to keep a large enough timestep, and an explicit time scheme on the larger cells in the volume, in order to limit the memory use [96]. However, such hybrid schemes are not currently available in `TrioCFD`, so some developments would be needed first.

In order to model turbulent fluctuations without using as many computational resources, we also developed a simple toy model of a periodic jet flow in a cylinder. Pre-calculations were performed on this toy model, and revealed turbulent fluctuation amplitudes (before coupling) in the same range as in the MSFR — both flows are nonetheless quite different. A steady-state coupled calculation was also performed, and transient coupled calculations on this toy model are currently being performed.

Appendices

A Nomenclature

We list here the notations used. We chose to keep as much as possible the usual notations, which means that some letters or symbols have two different meanings, because they have a different use in neutronics and thermal-hydraulics. For this reason we divide here the notations used between neutronics and thermal-hydraulics.

Table A.1: Neutronics nomenclature.

Symbol	Definition	Unit
Latin letters		
C_i	precursors concentration (group i)	m^{-3}
\mathcal{D}	delayed fissions operator	m^{-1}
\mathcal{F}	prompt fissions operator	m^{-1}
\mathcal{F}_∞	steady-state fission operator	m^{-1}
k_{eff}	effective neutron multiplication factor	—
$k_{p,eff}$	effective prompt neutron multiplication factor	—
\mathcal{L}	losses operator	m^{-1}
N	nuclei density	m^{-3}
pcm	per cent mille	—
\mathcal{S}	scattering operator	m^{-1}
S_{C_i}	source of precursor (group i)	$\text{m}^{-3}.\text{s}^{-1}$
\mathbf{v}	neutron velocity	$\text{m}.\text{s}^{-1}$

Greek letters		
β	total delayed neutron fraction	—
β_i	partial delayed neutron fraction (group i)	—
β_{eff}	total effective delayed neutron fraction	—
λ_i	decay constant (group i)	s^{-1}
ν	total neutron multiplicity	—
\mathcal{S}	scattering operator	m^{-1}
σ	microscopic cross section	m^2
σ_g	multigroup cross section	m^2
Σ	macroscopic cross section	m^{-1}
Σ_f	macroscopic fission cross section	m^{-1}
Σ_s	macroscopic scattering cross section	m^{-1}
Σ_t	macroscopic total cross section	m^{-1}
ρ	reactivity	—
ϕ	scalar neutron flux	$m^{-2}.s^{-1}$
χ	total neutron spectrum	—
χ_p	prompt neutron spectrum	—
$\chi_{d,i}$	delayed neutron spectrum (group i)	—
ψ	angular neutron flux	$m^{-2}.s^{-1}$
ψ^*	adjoint angular neutron flux	—

Table A.2: Thermal-hydraulics nomenclature.

Symbol	Definition	Unit
Latin letters		
C	concentration	mol.m^{-3}
c_p	heat capacity	$\text{J.K}^{-1}.\text{kg}$
d	length of a cell	m
D	hydraulic diameter	m
D_m	mass diffusivity	$\text{m}^2.\text{s}^{-1}$
E	partial turbulent energy	J
\mathbf{g}	body forces vector	m.s^{-2}
h	heat transfer coefficient	$\text{W.m}^{-2}.\text{K}^{-1}$
k	total turbulent energy	J
K_N	Knudsen number	—
L	typical flow length	m
p	modified pressure	Pa
P	pressure	Pa
P_R	Prandtl number	—
P_{Rt}	turbulent Prandtl number	—
Sc_t	turbulent Schmidt number	—
Re	Reynolds number	—

S_C	source of concentration	mol.s^{-1}
S_m	source of momentum	m.s^{-2}
S_{th}	thermal source	K.s^{-1}
T^+	dimensionless temperature	—
\mathbf{u}	velocity field	m.s^{-1}
$\bar{\mathbf{u}}$	mean velocity field	m.s^{-1}
\mathbf{u}^*	random velocity field	m.s^{-1}
$\tilde{\mathbf{u}}$	filtered velocity field	m.s^{-1}
\mathbf{u}'	residual velocity field	m.s^{-1}
U	typical flow velocity	m.s^{-1}
u^+	dimensionless velocity	—
u_η	Kolmogorov velocity scale	m.s^{-1}
y^+	dimensionless distance to the wall	—
Greek letters		
α	thermal diffusivity	$\text{m}^2.\text{s}^{-1}$
β_{th}	thermal expansion coefficient	—
ϵ	turbulent energy dissipation rate	$\text{J.kg}^{-1}.\text{s}^{-1}$
η	Kolmogorov length scale	m
κ	wavenumber	m^{-1}
κ^*	Von Karman constant	—
κ_{th}^*	thermal Von Karman constant	—
λ	thermal conductivity	$\text{W.m}^{-1}.\text{K}^{-1}$
Λ	Darcy friction factor	—

μ	dynamic viscosity	Pa.s
ν	kinematic viscosity	$\text{m}^2.\text{s}^{-1}$
ν_{SGS}	sub-grid-scale viscosity	$\text{m}^2.\text{s}^{-1}$
ν_t	turbulent viscosity	$\text{m}^2.\text{s}^{-1}$
ρ	density	$\text{kg}.\text{m}^{-3}$
σ	stress tensor	Pa
τ	Reynolds stress tensor	Pa
$\tilde{\tau}$	sub-grid-scale tensor	Pa
τ_η	Kolmogorov time scale	s
τ_w	shear stress at the wall	Pa
Ψ	conservative forces potential	J

Table A.3: Abbreviations used.

AMSTER	Actinides Molten Salt Transmuter
ANP	Aircraft Nuclear Propulsion project
ARE	Aircraft Nuclear Experiment
C3PO	Collaborative Code Coupling Platform
CAD	Computer-aided Design
CFD	Computational Fluid Dynamics
CFL	Courant-Friedrichs-Lewy condition
DNS	Direct Numerical Simulation
LES	Large Eddy Simulation
LES_IQ	Large Eddy Simulation Index Of Quality
LES-NWM	Large Eddy Simulation with Near-Wall Modelling
MCNP	Monte Carlo N-Particle transport code
MOSART	Molten Salt Actinide Recycler and Transmuter
MPO	Multi-Parameter Output
MSBR	Molten Salt Breeder Reactor
MSFR	Molten Salt Fast Reactor
MSR	Molten Salt Reactor
MSRE	Molten Salt Reactor Experiment
P_N	Spherical Harmonics angular discretisation

RANS	Reynolds-Averaged Navier-Stokes
S_N	Discrete Ordinates angular discretisation
SGS	Sub-Grid-Scale
SP_N	Simplified Spherical Harmonics angular discretisation
TASSE	Thorium Based Accelerator Driven System with Simplified Fuel Cycle
TFM	Transient Fission Matrices
TMSR	Thorium Molten Salt Reactor
V&V	Verification and Validation
VLES	Very Large Eddy Simulation
WALE	Wall-Adapting Local Eddy-Viscosity model

B Development of a toy model for turbulent fluctuations analysis

In order to model turbulent fluctuations without requiring large computational resources, we developed a simple toy model of a periodic turbulent jet flow in a cylinder.

B.1 Thermal-hydraulic model

B.1.a Resolved equations

Only the fuel salt is considered in the thermal-hydraulic model. The velocity field for the fuel is obtained by computing the Navier-Stokes equations (Equations I.29). The temperature field is obtained through the energy equation (Equation I.26). The precursor concentrations are not computed in this model.

B.1.a Physical properties

The fuel salt used in the toy model is the same as for the MSFR (see Section IV.2). Its properties are thus described in Table IV.1.

B.1.a Geometry and meshing

The geometry considered is a cylinder of 2 m in diameter by 2 m in height — approximately the size of the MSFR core. The mesh size is determined by the y^+ value for the surface mesh (it is below 300 everywhere), and the LES_IQ for the core mesh — the goal here is not to have a perfectly resolved LES, so the LES_IQ is a bit under 0.8 in some small regions of the core. The mesh and the assessment parameters are presented in Figures B.1 and B.2. The mesh is composed of 3 millions tetrahedra, 40 times fewer than for the MSFR.

B.1.a Boundary and initial conditions

The toy model consists of a periodic jet in a cylinder, surrounded by non-slip, adiabatic walls. The boundary conditions are presented in Figure B.3. The initial velocity is set to $2 \text{ m}\cdot\text{s}^{-1}$, in order to have a Reynolds number similar to the MSFR case. The initial temperature is set to $700 \text{ }^\circ\text{C}$. It should be noted that for such a cylinder

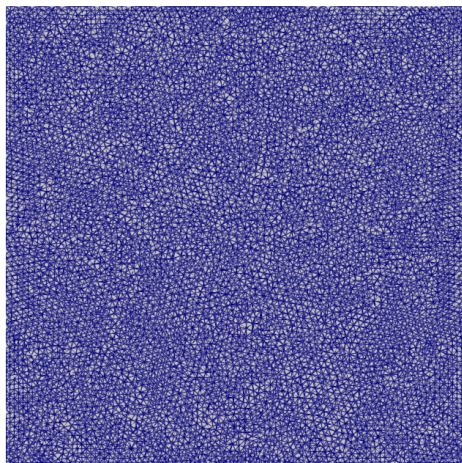


Figure B.1: Elevation section of the thermal-hydraulic mesh used for the toy model (3 millions tetrahedra).

height, the periodic boundary conditions will disturb the turbulent flow, like it did for the MSFR sector with symmetry boundary conditions — as the vortices near the outlet and inlet cannot develop without being disturbed by the boundary conditions imposed. For studying a periodic jet flow, extra length should be added at the inlet and the outlet [97]. Here however, the goal is not to have a well-resolved LES but to have a short computation time, so no extra height is added.

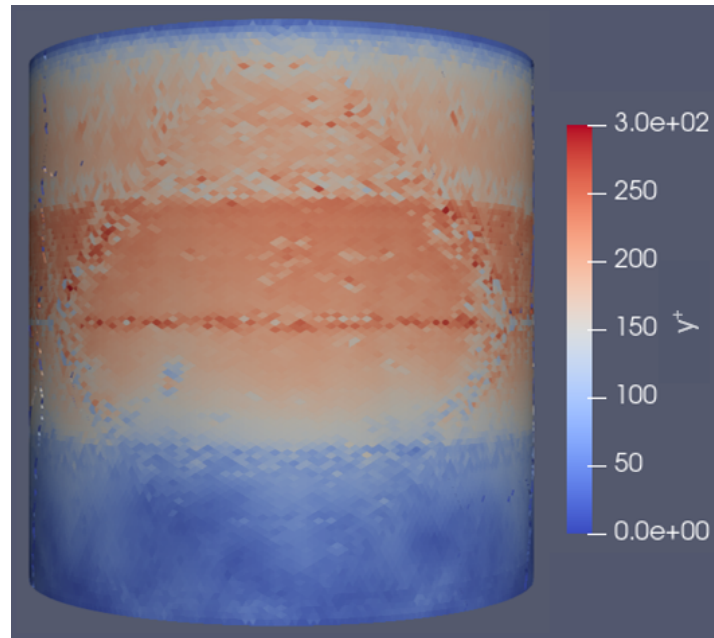
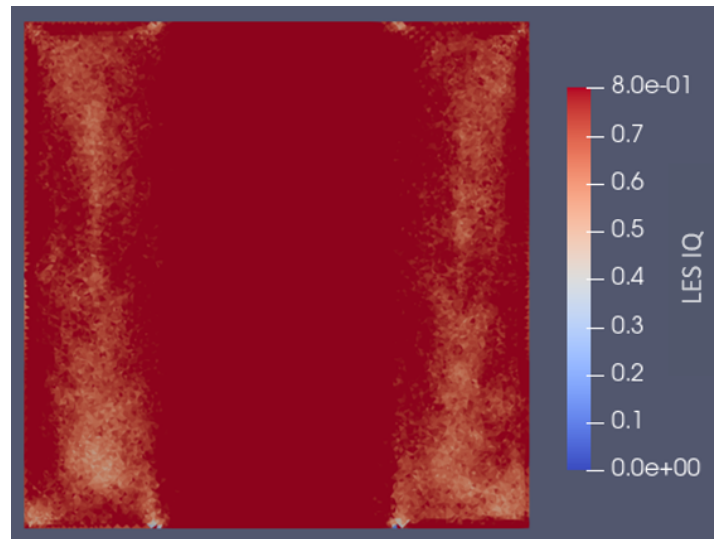
B.1.a Turbulence model

The same LES model as for the MSFR is used. The numerical scheme used is the one summarised in Table IV.3.

B.1.a Source terms

The cylinder being vertical, the gravity acceleration as well as the Boussinesq approximation for buoyancy forces are taken into account. There is no pump, the initial velocity conjugated with periodic boundary conditions ensure that the flow keeps flowing.

For the thermal-hydraulic pre-calculation, the same power distribution correlation as for the MSFR is taken (see Section IV.2.f). There is no heat exchanger, and with no heat removal and the periodic boundary conditions, the flow would heat up indefinitely. A convective heat transfer function is thus added on the whole domain, with an exterior temperature set to 600 °C and a transfer coefficient h set to

(a) y^+ value for the toy model.

(b) LES_IQ value for the toy model (max scale fixed at 0.8).

Figure B.2: Thermal-hydraulic mesh assessment parameters for the toy model.

$10^6 \text{ W.m}^{-2}.\text{K}^{-1}$. It would be simpler to impose the temperature at the inlet of the cylinder, but TrioCFD currently requires a periodic temperature boundary condition if the velocity boundary condition is periodic.

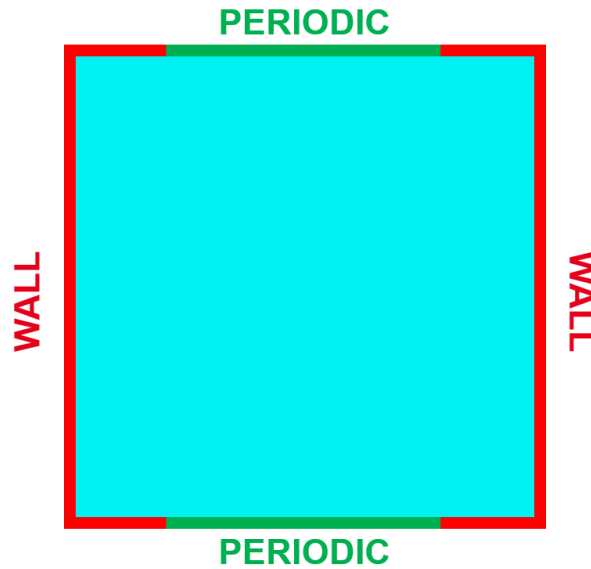


Figure B.3: Boundary conditions for the toy model.

B.1.a LES pre-calculation

A LES pre-calculation was performed, in order to start coupled calculations with an established flow. The temperature and velocity fields are presented in Figure B.4.

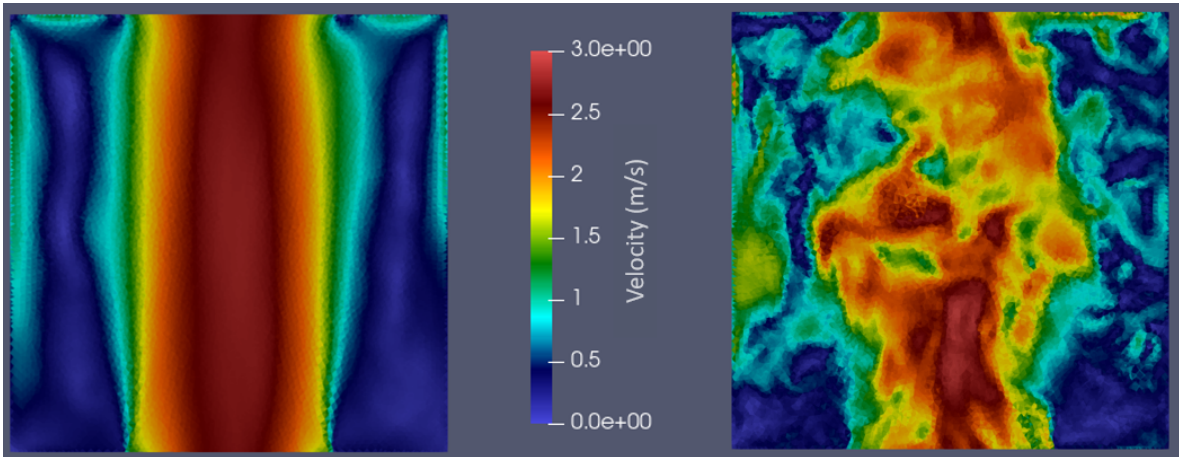
While the velocity field spans about the same range as in the MSFR core, the steady temperature field is about 100 °C higher than in the MSFR. This could probably be adjusted by setting a colder exterior temperature in the power extraction term.

In order to assess the amplitude of the turbulent fluctuations before coupling in the toy model, equatorial plots of the instantaneous velocity and temperature are presented in Figure B.5.

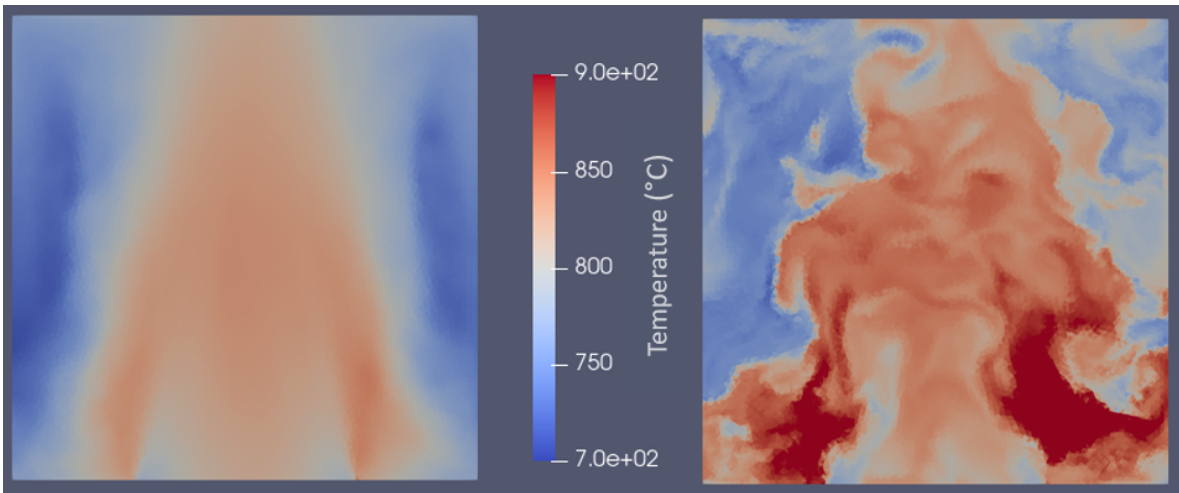
Local temperature gradients between 20 and 80°C per 10 cm can be seen in the center of the geometry, which is up to 4 times higher than in the MSFR core (Figure IV.20). However, the temperature near the wall seems very stable on a 20 cm width, which was not the case in the MSFR core.

In order to observe time fluctuations, temperature probes were set in the center of the geometry and near the wall. Results are presented in Figures B.6 and B.7. The flow takes about 10 s to develop, so times before 10 s are removed from the figures.

In the center of the geometry, temperature fluctuations of about $\mp 25^{\circ}\text{C}$, or $\mp 3\%$, can be measured, which is the same amplitude as in the MSFR. Near the wall, temperature fluctuations of about $\mp 15^{\circ}\text{C}$, or $\mp 2\%$, can be measured, with fewer high frequencies than in the center. Such fluctuations of the temperature should cause power



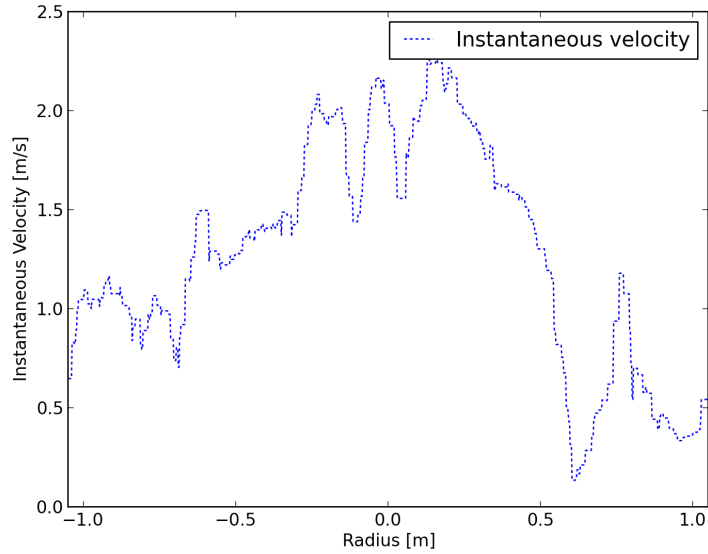
(a) Mean and instantaneous velocity fields.



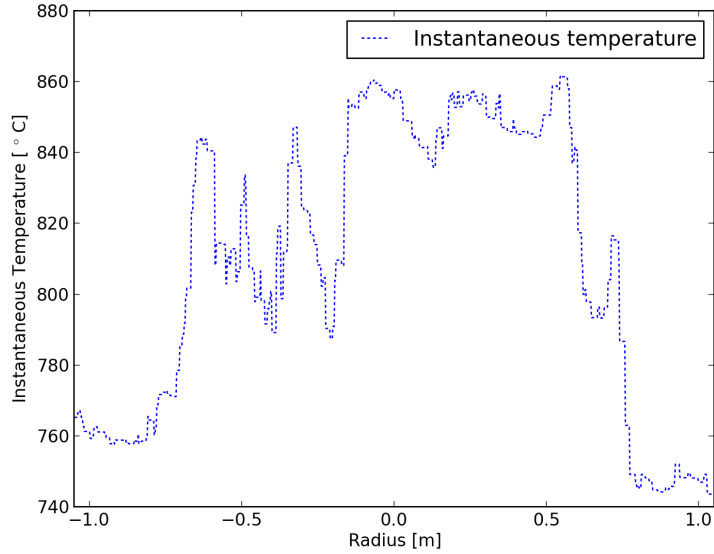
(b) Mean and instantaneous temperature fields.

Figure B.4: LES pre-calculation of the toy model: elevation sections of the mean and instantaneous fields.

fluctuations.



(a) Instantaneous velocity plot.



(b) Instantaneous temperature plot.

Figure B.5: Spatial fluctuations in the toy model: equatorial plots of the instantaneous fields.

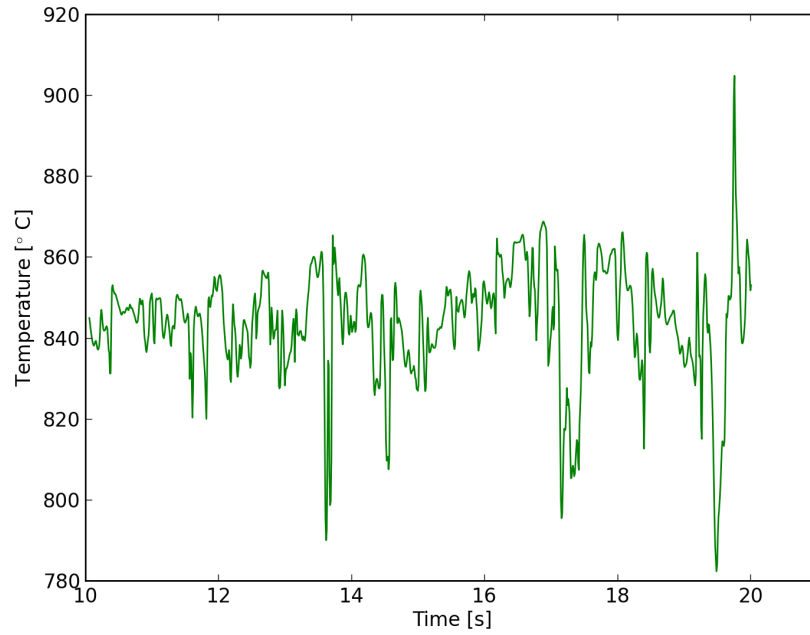


Figure B.6: Time fluctuations in the toy model: temperature evolution in the center of the core.

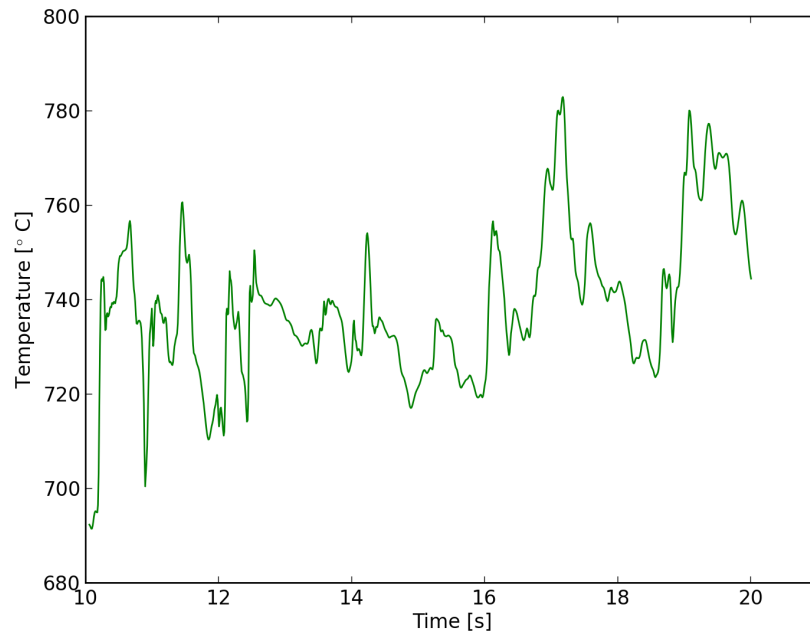


Figure B.7: Time fluctuations in the toy model: temperature evolution near the wall.

B.2 Neutronic model

B.2.b Lattice calculation

The MPO used for the toy model is the MPO computed for the MSFR (see Section IV.6.a). No additional lattice calculation was performed. The fertile blanket material was not used for the toy model however, because there is none.

B.2.b Core calculation

In the neutronic model, a reflector is added around the cylinder. The mesh size is set to 10 cm in the core, which is the typical mean free path of the fast neutrons. The mesh size for the reflector is coarser (50 cm). Vacuum boundary conditions are applied outside of the domain. The mesh is presented in Figure B.8. The mesh is composed of 70 000 tetrahedra, so about 7 times fewer than for the MSFR. The S_6 angular discretisation is used (48 different directions). The precursor transport is neglected, in order to use the optimised APOLL03[®] methods (see Section IV.7).

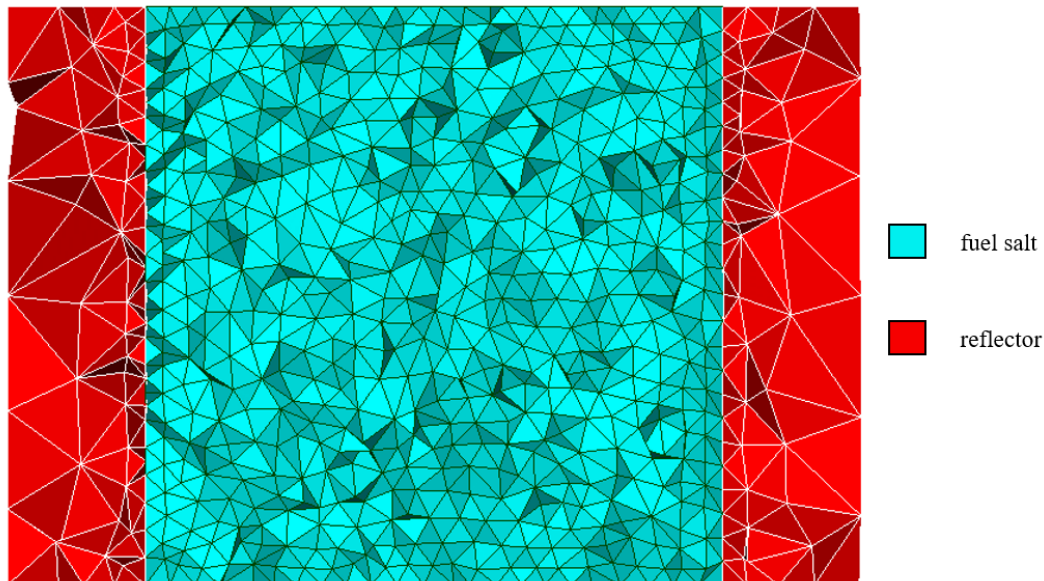


Figure B.8: Neutronic mesh used for the toy model.

B.2.b Neutronic pre-calculation

A neutronic pre-calculation was performed in order to compute the flux and the power distribution for a uniform 700 °C temperature. The power density field is shown

in Figure B.9.

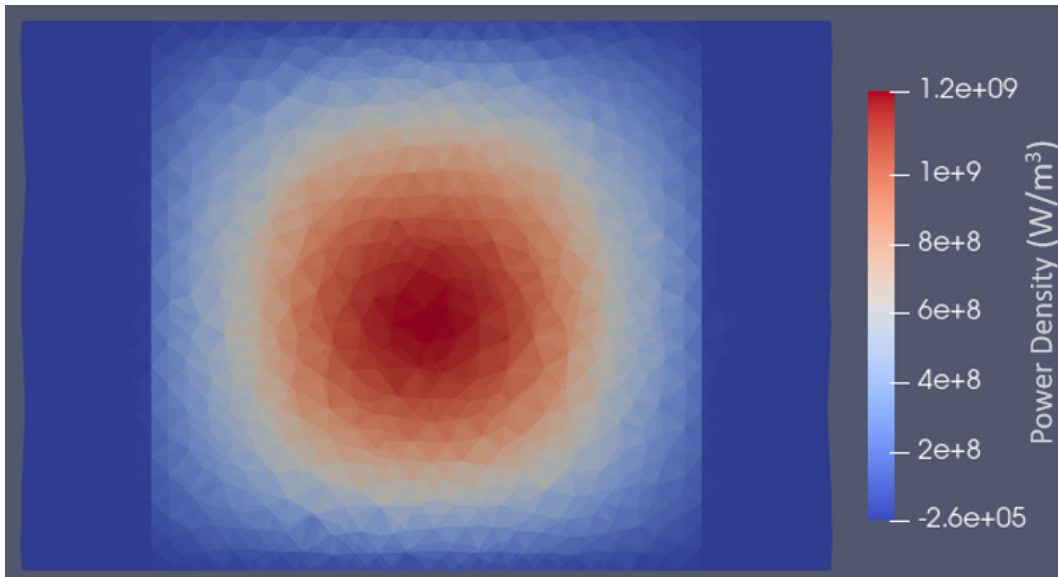


Figure B.9: Initial power density field of the toy model.

The next step is to couple both models and to run a coupled steady-state calculation, starting with the fields from the pre-calculations.

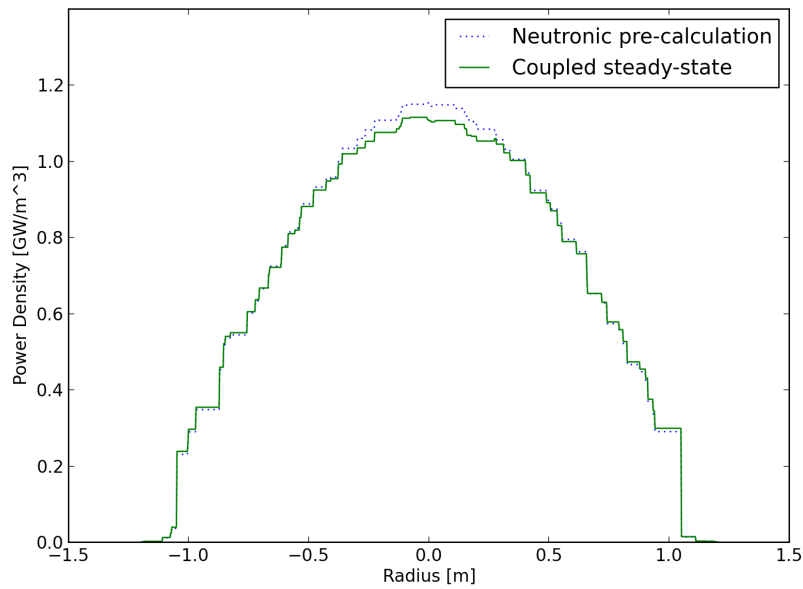
B.3 Coupled calculations

B.3.c Coupled steady-state calculation

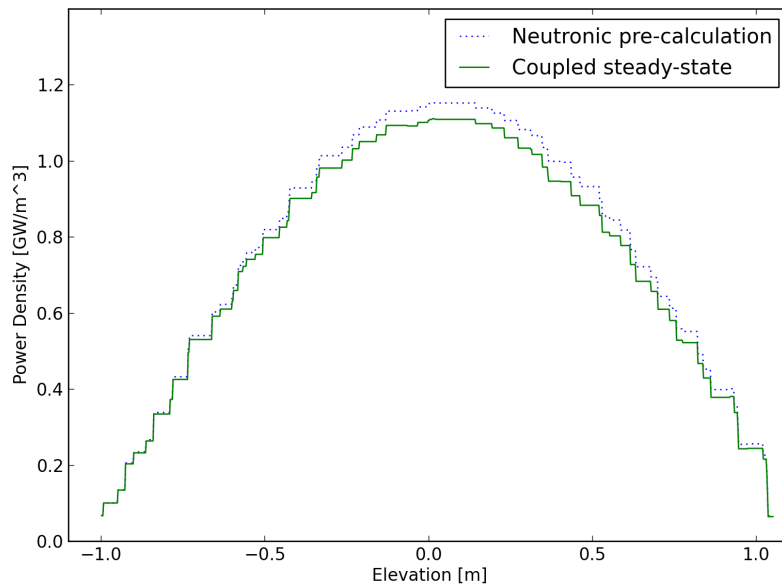
A coupled steady-state simulation was performed. Like for the MSFR case, since the precursor transport is not modelled and the total power is normalised during the APOLL03[®] steady-state calculation, the coupled fields are very similar to the fields computed during the independent pre-calculations. The power distribution is slightly modified, as shown in Figure B.10.

The shift of the power distribution towards the bottom is less visible than in the MSFR case, probably because of the large and hot recirculation zones around the jet flow that keeps hot the bottom of the geometry (see Figure B.4).

Power fluctuations could only be observed through transient calculations, which are currently performed on the toy model.



(a) Compared equatorial plots of the power distribution.



(b) Compared vertical plots of the power distribution.

Figure B.10: Compared equatorial (top) and vertical (bottom) plots of the power distribution between the neutronic pre-calculation (blues dashed lines) and the coupled calculation (solid green lines).

References

- [1] International Energy Agency, *Final Consumption and Electricity Generation*. www.iea.org. 2021.
- [2] *Gen. IV International Forum, Annual Report*. 2008.
- [3] R.C. Briant, W. B. Cottrell, and C. B. Ellis. *Aircraft Nuclear Propulsion Project Quarterly Progress Report*. ORNL-919. Feb. 26, 1951.
- [4] W. B. Cottrell, H. E. Hungerford, J. K. Leslie, and J. L. Meem. *Operation of The Aircraft Reactor Experiment*. ORNL-1845. 1955.
- [5] R. C. Robertson. *MSRE Design and Operation Report - Part I - Description of Reactor Design*. ORNL-TM-728. Jan. 1965.
- [6] D.O.E. *The Evaluation of the MSBR Project*. 1972.
- [7] M. Hery and A. Lecoq. “Results of and Prospects for Studies on Molten Salt Nuclear Reactors”. In: *International Symposium on Molten Salt Chemistry*. Kyoto, Japan, 1983.
- [8] V. Berthou and M. Salvatores. “The TASSE Concept : Thorium Based Accelerator Driven System with Simplified Fuel Cycle for Long Term Energy Production”. In: *Global 2001 international conference on: "back-end of the fuel cycle: from research to solutions"*. France, 2001.
- [9] Jean Vergnes and David Lecarpentier. “The AMSTER Concept (Actinides Molten Salt Transmuter)”. In: *Nuclear Engineering and Design* 216 (July 2002), pp. 43–67.
- [10] Alexandre Mourogov and Pavel Bokov. “Potentialities of the Fast Spectrum Molten Salt Reactor Concept: REBUS-3700”. In: *Energy Conversion and Management* 47 (Oct. 2006), pp. 2761–2771.

- [11] J. Serp et al. “The Molten Salt Reactor (MSR) in Generation IV: Overview and Perspectives”. In: *Progress in Nuclear Energy* 77 (2014), pp. 308–319.
- [12] *SAMOSAFER Project*. samosafer.eu. 2019.
- [13] Victor Ignatiev et al. “Progress in Development of Li,Be,Na/F Molten Salt Actinide Recycler & Transmuter Concept”. In: *ICAPP*. Nice, France, 2007.
- [14] Zhimin Dai. “17 - Thorium Molten Salt Reactor Nuclear Energy System (TMSR)”. In: *Molten Salt Reactors and Thorium Energy*. Woodhead Publishing, 2017, pp. 531–540.
- [15] *TerraPower*. www.terrapower.com.
- [16] *Kairos Power*. www.kairospower.com.
- [17] *Thorcon Power*. www.thorconpower.com.
- [18] *Terrestrial Energy*. www.terrestrialenergy.com.
- [19] *Seaborg Technologies*. www.seaborg.com.
- [20] *NAAREA*. www.naarea.fr.
- [21] Pietro Mosca. “APOLLO3[®]: Overview of the new Code Capabilities for Reactor Physics Analysis”. In: *M&C 2023*. Niagara Falls, Canada, 2023.
- [22] P.E. Angeli, U. Bieder, and G. Fauchet. “Overview of the TrioCFD code: Main features, V&V Procedures and Typical Applications to Engineering”. In: *NURETH-16*. Chicago, USA, 2015.
- [23] S. Marguet. *The Physics of Nuclear Reactors*. Springer International Publishing, 2017.
- [24] J. Planchard. *Méthodes Mathématiques en Neutronique*. EDF, 1995.
- [25] P. Reuss. *Précis de Neutronique*. EDP Sciences, 2003.
- [26] S. B. Pope. *Turbulent Flows*. Cambridge University Press, 2000.
- [27] J. M. Delhaye. *Thermohydraulique des Réacteurs*. EDP Sciences, 2013.
- [28] L. D. Landau and E. M. Lifshitz. *Fluid Mechanics*. Pergamon Press, 1959.
- [29] E. Rutherford. “The Scattering of α and β Particles by Matter and the Structure of the Atom”. In: *The London, Edinburgh, and Dublin Philosophical Magazine and Journal of Science* 21.125 (May 1911), pp. 669–688.

- [30] J. Chadwick. “Possible Existence of a Neutron”. In: *Nature* 129.3252 (Feb. 27, 1932), pp. 312–312.
- [31] O. Hahn and F Strassmann. “Über die Entstehung von Radiumisotopen aus Uran durch Bestrahlen mit schnellen und verlangsamten Neutronen”. In: *Naturwissenschaften* 26 (1938), pp. 755–756.
- [32] O. Hahn and F Strassmann. “Über den Nachweis und das Verhalten der bei der Bestrahlung des Urans mittels Neutronen entstehenden Erdalkalimetalle”. In: *Naturwissenschaften* 27 (1939), pp. 11–15.
- [33] L. Meitner and O. R. Frisch. “Disintegration of Uranium by Neutrons : a New Type of Nuclear Reaction”. In: *Nature* 3615 (Feb. 11, 1939), pp. 239–240.
- [34] H. Von Halban, F. Joliot, and L. Kowarski. “Liberation of Neutrons in the Nuclear Explosion of Uranium”. In: *Nature* 143 (Mar. 1939), pp. 470–471.
- [35] H. L. Anderson, E. Fermi, and Leo Szilard. “Neutron Production and Absorption in Uranium”. In: *Physical Review* 56 (Aug. 1, 1939), pp. 284–286.
- [36] A. J. M. Plompen and all. “The Joint Evaluated Fission and Fusion Nuclear Data Library, JEFF-3.3”. In: *The European Physical Journal A* 56.7 (July 14, 2020), p. 181.
- [37] *International Atomic Energy Agency - Nuclear Data Services*. www-nds.iaea.org.
- [38] Ju Kwangho and Kim Yonghee. “A Comparative Investigation of Doppler Broadening of Neutron Absorption and Photon-Induced Nuclear Resonance Fluorescence Reactions”. In: *Transactions of the Korean Nuclear Society*. Gyeongju, Korea, 2017.
- [39] *OpenMC Documentation*. docs.openmc.org/en/v0.12.2.
- [40] H. Bateman. “The Solution of a System of Differential Equations Occurring in the Theory of Radioactive Transformations”. In: *Proceedings of the Cambridge Philosophical Society* 15 (1910), pp. 423–427.
- [41] Zhaopeng Zhong, Alberto Talamo, and Yousry Gohar. “Monte Carlo and Deterministic Computational Methods for the Calculation of the Effective Delayed Neutron Fraction”. In: *Computer Physics Communications* 184 (2013), pp. 1660–1665.
- [42] L. F. Richardson. *Weather Prediction by Numerical Process*. Cambridge University Press, 1922.

- [43] A. N. Kolmogorov. “The Local Structure of Turbulence in Incompressible Viscous Fluid for Very Large Reynolds Numbers”. In: *Doklady Akademii Nauk SSSR* 30 (1941), pp. 299–303.
- [44] A. N. Kolmogorov. “On Degeneration of Isotropic Turbulence in an Incompressible Viscous Liquid”. In: *Doklady Akademii Nauk SSSR* 31 (1941), pp. 538–541.
- [45] A. N. Kolmogorov. “Dissipation of Energy in the Locally Isotropic Turbulence”. In: *Doklady Akademii Nauk SSSR* 32 (1941), pp. 19–21.
- [46] L. Prandtl. “Bericht über Untersuchungen zur ausgebildeten Turbulenz”. In: *Zeitschrift für Angewandte Mathematik und Mechanik* 5 (1925), pp. 136–139.
- [47] Th. Von Kármán. *Mechanische Ähnlichkeit und Turbulenz*. Gött. Nachr., 1930.
- [48] H. Reichardt. “Vollständige Darstellung der turbulenten Geschwindigkeitsverteilung in glatten Leitungen”. In: *Zeitschrift für Angewandte Mathematik und Mechanik* 31 (1951), pp. 208–219.
- [49] M. Tano, P. Rubiolo, and J. Ragusa. “Accuracy Analysis of Near Wall Thermal-Hydraulics Modeling of Molten Salt Reactors”. In: *NURETH-18*. Portland, USA, August 18-23 2019, 2020.
- [50] O. Hernandez. “Quelques Contributions vers la Simulation Parallèle de la Cinétique Neutronique et la Prise en Compte de Données Observées en Temps Réel”. PhD thesis. 2014.
- [51] W.P. Jones and B.E. Launder. “The Prediction of Laminarization with a Two-Equation Model of Turbulence”. In: *International Journal of Heat and Mass Transfer* 15 (1972), pp. 301–314.
- [52] J. Smagorinsky. “General Circulation Experiments with the Primitive Equations”. In: *Monthly Weather Review* 91 (1963), pp. 99–164.
- [53] F. Nicoud and F. Ducros. “Subgrid-Scale Stress Modelling Based on the Square of the Velocity Gradient Tensor”. In: *Flow, Turbulence and Combustion* 62 (1999), pp. 183–200.
- [54] I. B. Celik, Z. N. Cehreli, and I. Yazuv. “Index of Resolution Quality for Large Eddy Simulations”. In: *Journals of Fluids Engineering* 127 (2005), pp. 949–958.
- [55] Axel Laureau. “Développement de Modèles Neutroniques pour le Couplage Thermohydraulique du MSFR et le Calcul de Paramètres Cinétiques Effectifs”. PhD thesis. 2015.

- [56] *OpenFOAM code*. www.openfoam.com.
- [57] *MCNP code*. mcnp.lanl.gov.
- [58] A. Laureau et al. “Transient Fission Matrix: Kinetic Calculation and Kinetic Parameters β_{eff} and Λ_{eff} Calculation”. In: *Annals of Nuclear Energy* 85 (Nov. 2015), pp. 1035–1044.
- [59] Marco Tiberga et al. “Results from a Multi-Physics Numerical Benchmark for Codes Dedicated to Molten Salt Fast Reactors”. In: *Annals of Nuclear Energy* 142 (July 2020), pp. 107428–107446.
- [60] A. Laureau et al. “Coupled Neutronics and Thermal-Hydraulics Numerical Simulations of a Molten Salt Fast Reactor (MSFR)”. In: *SNA + MC 2013*. Paris, France, October, 2013.
- [61] A. Laureau et al. “Transient Coupled Calculations of the Molten Salt Fast Reactor using the Transient Fission Matrix Approach”. In: *Nuclear Engineering and Design* 316 (May 2017), pp. 112–124.
- [62] A. Laureau et al. “Spatial Analysis of Unprotected Transients in Heterogeneous Sodium Fast Reactors”. In: *Annals of Nuclear Energy* 115 (2018), pp. 554–564.
- [63] Philippe Spalart, W-H Jou, Michael Strelets, and Steven Allmaras. “Comments on the Feasibility of LES for Wings, and on a Hybrid RANS/LES Approach”. In: *Advances in DNS/LES*. Arlington, Texas, January, 1997.
- [64] A. Laureau et al. “Unmoderated Molten Salt Reactors Design Optimisation for Power Stability”. In: *Annals of Nuclear Energy* 177 (2022), pp. 109265–109273.
- [65] Carlo Fiorina, Ivor Clifford, Manuele Aufiero, and Konstantin Mikityuk. “GeN-Foam: a Novel OpenFOAM® Based Multi-Physics Solver for 2D/3D Transient Analysis of Nuclear Reactors”. In: *Nuclear Engineering and Design* 294 (Dec. 2015), pp. 24–37.
- [66] Eric Cervi, Stefano Lorenzi, Antonio Cammi, and Lelio Luzzi. “An Euler-Euler Multiphysics Solver for the Analysis of the Helium Bubbling System in the MSFR”. In: *26th International Conference Nuclear Energy For New Europe*. Bled, Slovenia, September, 2017.

- [67] Eric Cervi, Stefano Lorenzi, Antonio Cammi, and Lelio Luzzi. “Development of a Multiphysics Model for the Study of Fuel Compressibility Effects in the Molten Salt Fast Reactor”. In: *Chemical Engineering Science* 193 (Jan. 2019), pp. 379–393.
- [68] Eric Cervi, Stefano Lorenzi, Lelio Luzzi, and Antonio Cammi. “Multiphysics Analysis of the MSFR Helium Bubbling System: A Comparison Between Neutron Diffusion, SP3 Neutron Transport and Monte Carlo Approaches”. In: *Annals of Nuclear Energy* 132 (Oct. 2019), pp. 227–235.
- [69] M. Tibergera. “Development of a High-Fidelity Multi-Physics Simulation Tool for Liquid-Fuel Fast Nuclear Reactors”. PhD thesis. 2020.
- [70] Marco Tibergera, Danny Lathouwers, and Jan Leen Kloosterman. “A Discontinuous Galerkin FEM Multi-Physics Solver for the Molten Salt Fast Reactor”. In: *International Conference on Mathematics and Computational Methods Applied to Nuclear Science and Engineering*. 2019.
- [71] A.J Novak et al. “Multiphysics Coupling of OpenMC CAD-Based Transport to MOOSE using Cardinal and Aurora”. In: *The International Conference on Mathematics and Computational Methods Applied to Nuclear Science and Engineering (M&C 2023)*. Niagara Falls, Canada, August, 2023.
- [72] Jun Fang, Feng Bo, and Dillon Shaver. “CFD Simulations of Molten Salt Fast Reactor Core Flow”. In: *The 19th International Topical Meeting on Nuclear Reactor Thermal Hydraulics (NURETH-19)*. Brussels, Belgium, March, 2022.
- [73] Thibault Le Meute. “Modélisation d’un Scénario d’Insertion de Réactivité dans un Réacteur à Sel Fondu de Génération IV”. PhD thesis. 2022.
- [74] *C3PO Coupling Platform*. sourceforge.net/projects/cea-c3po. 2020.
- [75] *SALOME CAO, Meshing and Post-treatment Platform*. www.salome-platform.org. 2000.
- [76] Cyril Patricot. “Couplages Multi-Physiques: Évaluation des Impacts Méthodologiques lors de Simulations de Couplages Neutronique/Thermique/Mécanique.” PhD thesis. 2016.
- [77] Nathan Greiner et al. “A New Calculation Strategy for Molten Salt Reactor Neutronic-Thermalhydraulic Analysis Implemented with APOLL03[®] and TRUST/TrioCFD”. In: *Nuclear Science and Engineering* (2023).

- [78] François Martin et al. “Coupled Neutronics–Thermal-hydraulics Modelling of a Molten Salt Reactor: the Aircraft Reactor Experiment”. In: *M&C 2023*. Niagara Falls, Canada, 2023.
- [79] François Martin et al. “Coupled Neutronics–Thermal-hydraulics Modelling of a Molten Salt Reactor: the Aircraft Reactor Experiment”. In: *Soon to be published* (2024).
- [80] Y.D. Manly et al. *Aircraft Reactor Experiment - Metallurgical Aspects*. ORNL-2349. 1957.
- [81] B. Lubarsky and B. L. Greenstreet. *Thermodynamic and Heat Transfer Analysis of the Aircraft Reactor Experiment*. ORNL-1535. 1953.
- [82] E. Brun et al. “TRIPOLI-4[®], CEA, EDF and AREVA Reference Monte Carlo Code”. In: *Annals of Nuclear Energy* 82 (2015).
- [83] Ankit Rohatgi. *Webplotdigitizer: Version 4.6*. 2022. URL: automeris.io/WebPlotDigitizer.
- [84] François Martin et al. “CFD Simulations of the Molten Salt Fast Reactor”. In: *NURETH-20*. Washington D.C, U.S, 2023.
- [85] L. Mathieu. “Cycle Thorium et Réacteurs à Sel Fondus : Exploration du Champ des Paramètres et des Contraintes Définissant le Thorium Molten Salt Reactor”. PhD thesis. 2005.
- [86] H. Pitois et al. “A Closed Fuel Cycle Option using the MSFR Concept with Chloride Salts and the U/Pu Cycle”. In: *GLOBAL International Conference on Nuclear Fuel Cycle*. Reims, France, 2022.
- [87] H. Rouch et al. “Preliminary Thermal–hydraulic Core Design of the Molten Salt Fast Reactor (MSFR)”. In: *Annals of Nuclear Energy* 64 (2014), pp. 449–456.
- [88] E. Merle-Lucotte et al. “Minimizing the Fissile Inventory of the Molten Salt Fast Reactor”. In: *Advances in Nuclear Fuel Management IV*. Hilton Head Island, USA, April 12-15, 2009.
- [89] E. Merle-Lucotte et al. “Preliminary Design Assessment of the Molten Salt Fast Reactor”. In: *European Nuclear Conference*. Manchester, UK, 2012.
- [90] P. R. H. Blasius. “Das Aehnlichkeitsgesetz bei Reibungsvorgängen in Flüssigkeiten”. In: *Forschungsheft* 131 (1913), pp. 1–41.
- [91] Tsan-Hsing Shih et al. “A New K-Epsilon Model for High Reynolds Number Turbulent Flows”. In: *Computers Fluids* 24.3 (1995), pp. 227–238.

- [92] François Martin, Axel Laureau, Max Begue, and Thomas Sornay. “A Numerical Benchmark for RANS Simulations on the Molten Salt Fast Reactor”. In: *Soon to be published* (2024).
- [93] Pierre-Loïc Bacq, Antoine Gerschenfeld, and Michael Ndjinga. “PolyMAC: Staggered Finite Volume Methods on General Meshes for Incompressible Navier–Stokes Problems”. In: *International Conference on Finite Volumes for Complex Applications*. Strasbourg, France, 2023.
- [94] Jean-Baptiste-Joseph Fourier. *Théorie Analytique de la Chaleur*. Firmin Didot, père et fils, 1822.
- [95] Kenneth Assogba. “Étude d’un Schéma Numérique pour Résoudre l’Equation de Transport Neutronique Basé sur la Méthode PN et la Méthode des Eléments Finis Discontinus avec des Maillages 3D non Structurés et Curvilignes”. PhD thesis. 2023.
- [96] Per-Olof Persson. “High-Order LES Simulations Using Implicit-Explicit Runge-Kutta Schemes”. In: *49th AIAA Aerospace Sciences Meeting including the New Horizons Forum and Aerospace Exposition*. Orlando, Florida, 2011.
- [97] Michael Breuer. “Boundary Conditions for LES”. In: *LES for Acoustics*. Cambridge Univeristy Press, 2007. Chap. 5.2.

Summary - Résumé des travaux

Summary

Molten salt reactors (MSRs) are a type of 4th generation nuclear reactors. The number of molten salt reactor projects multiplied in the world since the 2010s. These reactors present some specificities: the delayed neutron precursors are transported by the fuel salt flow; the high density feedback coefficient strongly couples the neutronic and thermal-hydraulic equations; for certain designs, the fuel salt flows through a large, empty core cavity and is highly turbulent, causing large turbulent fluctuations of the temperature and power distributions in the core. Various calculation codes and multi-physics tools are being developed to model these reactors. In CEA, a reference code coupling the deterministic neutronic code APOLL03[®] and the CFD code TRUST/TrioCFD is used to study MSRs. The objective of this thesis is to study the turbulent fluctuations in an MSR core, using the APOLL03[®] – TrioCFD coupling.

First of all, we present the fundamental equations governing the neutronics and thermal-hydraulics of a nuclear reactor core: the Boltzmann equation for the evolution of the neutron flux, and the Navier-Stokes equations for the evolution of the velocity field. We then show how these equations are modified and coupled in the specific case of an MSR: the precursor evolution equation has an advection term, which modifies the nature of the steady-state Boltzmann equation; the temperature and precursor concentration fields, for a turbulent flow, present turbulent fluctuations which cause in turn fluctuations of the power field through feedback mechanisms (density and Doppler). The coupled neutronic–thermal-hydraulic problem is finally presented.

We then show how to solve this coupled problem numerically. We first present the classical methods for solving the (steady-state and time-dependent) Boltzmann equation, as well as the Navier-Stokes for laminar and turbulent regimes, using RANS

and LES approximations. We then present some multiphysics codes developed in France, Europe and the United States for MSRs studies. Finally, we present the APOLL03[®] – TrioCFD code, used in this thesis, as well as the coupling schemes for steady-state and transient simulations. The physics and modelling of MSRs having been presented, simulations can then be performed.

A first step contributing to validate the recently developed APOLL03[®] – TrioCFD coupling, is to model the very first MSR, the Aircraft Reactor Experiment (ARE), in order to compare simulations to experimental data. A numerical model of the ARE is built, based on the information contained in several operation reports.

Regarding the thermal-hydraulic model, several simplifications are made: the salt and liquid sodium flows are modelled as one-dimensional and laminar; the sodium layers above and below the core are not represented; the porosities in the beryllium oxide moderator are not treated, but replaced by a gap between the BeO blocks; the core is not cut to fit a cylinder, the hexagonal lattice is preserved and certain peripheral assemblies are removed completely; the secondary circuit and heat exchangers are not modelled, so boundary conditions for the velocity, temperature and concentration fields are imposed at the inlets instead; the outer edges of the moderator are treated as adiabatic.

The neutronic model also contains approximations and assumptions: because of the uncertainties regarding the moderator density and impurity concentrations in the inconel pipes and in the moderator, two different datasets giving the right critical fuel mass are created and compared based on the control rods reactivity values. A dataset with a low moderator density and low impurity concentrations is selected. The self-shielded macroscopic sections are not homogenised — with the exception of the inconel and beryllium oxide around the salt, which are treated as a single moderator material — and discretised over 20 (for steady-state simulations) and 6 (for transients) energy groups, as well as 3 temperature parameters and 2 rod concentration parameters. In the core geometry for the neutronic calculation, the salt bends are straightened, and the hexagonal lattice is kept (no cylindrical cut), with some peripheral assemblies removed completely. 8 precursor groups are considered; the angular discretisation is made over 80 (for steady-state simulations) and 48 (for transients) directions.

A first steady-state coupled simulation is performed, in order to reproduce the nominal state of the ARE. The total power, salt and sodium flow rates, as well as the inlet temperatures and concentrations are imposed. The average and outlet temper-

atures of the salt and the sodium are measured and compared with the experimental data. The simulated salt is slightly warmer (+0.3 %) and the sodium colder (-5 %), which can be explained by the simplified sodium modelling, which causes it to exit the core too quickly.

A series of coupled steady-state simulations is then performed in order to measure the variation of β_{eff} with the fuel salt flow rate (experiment L-7). The temperatures are fixed and the input salt flow rate changed at each simulation. The reactivity is then measured and compared with the experimental data. A slight over-reactivity in the simulations for intermediate flow rates can be explained by the one-dimensional modelling of the salt flow, which causes more precursors to be flushed out of the core. This does not explain the slight under-reactivity at zero flow however.

Transient simulations are performed. The first (experiment H-8) consists of a progressive reactivity insertion by withdrawing the regulating rod (+400 pcm in 37.5 s). If an initial simplified simulations (instantaneous insertion of +400 pcm of reactivity) causes too intense and rapid a transient, a second model that progressively dilute the rod provides more adequate results: the maximum simulated power is 2.5 % too low, and the simulated final power is 14 % too high — the latter difference can be explained by the inlet fuel salt temperature which is fixed in the simulation.

A second transient simulation is performed to reproduce a load-following experiment (experiment H-14). The power extracted at the exchanger is increased, which decreases the inlet salt temperature — the simulation directly imposes a decrease in the inlet salt temperature (-44 K in 1 min). Through feedback mechanisms, the power and outlet temperature increase before stabilising at the extracted power. The simulation stopped before convergence, for reasons that remain to be understood.

The results of the simulations, which can be improved but are satisfactory, contribute to the validation of the APOLL03[®] – TrioCFD coupling.

The APOLL03[®] – TrioCFD code is then used to model the Molten Salt Fast Reactor (MSFR), in order to study the turbulent fluctuations in its core.

The thermal-hydraulic model of the MSFR core is particularly studied. Firstly, RANS simulations are performed, without neutronic coupling — the power distribution in the core is fixed. Various sensitivity studies are performed: sensitivity to the calculation geometry (full core or only a sector with symmetric boundary conditions); sensitivity to the heat exchanger modelling; a mesh convergence study; impact of the order of the spatial discretisation schemes; impact of the RANS model used (classical

or realisable $k - \epsilon$). These different studies enable us to create a mesh adapted to LES simulations, as well as to define a numerical benchmark for comparing the results provided by `TrioCFD` to other CFD codes, using a RANS model on an MSFR sector (benchmark which is developed and carried out in collaboration with partners from CNRS, Orano and Framatome).

LES simulations are then performed (without neutronic coupling). A comparison between the results obtained on the full core and on a sector with symmetric boundary conditions shows that the imposed symmetry heavily disturbs the formation of eddies in the core and distorts the simulation results. The mean LES velocity and temperature fields are compared with the RANS fields. Finally, the space and time fluctuations of the temperature field are measured. Without coupling, the time fluctuations of the temperature in the centre of the core are estimated at $\mp 3\%$.

A neutronic model of the MSFR core is then developed. Three materials are considered: the fuel salt, the radial fertile blanket and the axial reflectors; the self-shielded macroscopic cross-sections are discretised over 6 energy groups and one temperature parameter (fuel salt). The heat exchangers are not represented in the neutronic geometry; the angular discretisation is made over 48 directions; the precursors are considered to be immobile, in order to greatly speed up the neutronic calculation time. An initial steady-state calculation with uniform temperatures is performed, in order to obtain a first neutron flux and power distribution.

A steady-state coupled calculation is performed. The total power is fixed in the neutronic calculation, only the power distribution can vary: a slight shift of the power distribution towards the bottom of the core (where the temperature is cooler) is observed. The thermal-hydraulic calculation runs on a degraded mesh to save computing time, which prevents a comparison with the fields obtained from the LES pre-calculation. A coupled transient calculation is launched, but the very long computation time prevent us from obtaining relevant results.

A better parallelization of the problem, as well as the use of HPC resources should enable the computation of coupled transients on the MSFR core. In order to facilitate the study of turbulent fluctuations on a smaller case, a toy model of a periodic turbulent flow in a cylinder is also being developed. Coupled simulations are currently being performed on this model.

Résumé des travaux

Les réacteurs à sels fondus (RSF) sont un type de réacteur nucléaire de 4ème génération. Les projets de réacteurs à sels fondus se multiplient dans le monde depuis les années 2010. Ces réacteurs possèdent une physique assez particulière : les précurseurs de neutrons retardés sont transportés par l'écoulement de sel combustible ; le fort coefficient de contre-réaction par densité couple fortement les équations neutroniques et thermohydrauliques ; pour certains designs, l'écoulement hautement turbulent du sel dans un gros volume libre cause d'importantes fluctuations turbulentes de température et de puissance. Différents codes de calcul et outils multiphysiques sont développés afin de modéliser cette physique particulière aux cœurs des RSFs. Au CEA, un code de référence couplant le code de neutronique déterministe APOLL03[®] et le code de CFD TRUST/TrioCFD est utilisé pour l'étude des RSFs. L'objectif de cette thèse est d'étudier les fluctuations turbulentes dans un cœur de RSF, en utilisant le couplage APOLL03[®] – TrioCFD.

Tout d'abord, nous exposons les équations fondamentales régissant le comportement neutronique et thermohydraulique d'un cœur de réacteur nucléaire : l'équation de Boltzmann pour l'évolution du flux neutronique, et les équations de Navier-Stokes pour l'évolution du champ de vitesse. Nous montrons ensuite comment sont modifiées et couplées ces équations dans le cas spécifique d'un RSF : l'équation d'évolution des précurseurs possède un terme d'advection, ce qui modifie la nature de l'équation de Boltzmann en régime stationnaire ; les champs de température et de concentration en précurseurs du fluide, pour un écoulement turbulent, présentent des fluctuations turbulentes, qui se répercutent sur le champ de puissance par les mécanismes de contre-réaction (densité et Doppler). Le problème couplé neutronique–thermohydraulique est finalement exposé.

Nous montrons ensuite comment résoudre numériquement ce problème couplé. Nous exposons tout d'abord les méthodes classiques de résolution numérique de l'équation de Boltzmann (en régime stationnaire et transitoire), ainsi que des équations de Navier-Stokes (en régime laminaire et turbulent, via les approximations RANS et LES). Nous évoquons ensuite différents codes multiphysiques, développés en France, en Europe et aux États-Unis pour l'étude des RSFs. Nous présentons finalement le couplage APOLL03[®] – TrioCFD, utilisé dans cette thèse, ainsi que les schémas de couplage pour des simulations en régime stationnaire et transitoire. La physique et la

modélisation des RSFs ainsi exposées, des simulations peuvent ensuite être réalisées.

Une première étape, servant de validation du couplage APOLL03[®] – TrioCFD, outil récemment développé, consiste à modéliser le tout premier réacteur à sels fondus, l’Aircraft Reactor Experiment (ARE), afin de réaliser des comparaisons calculs-mesures. Nous construisons un modèle numérique de l’ARE d’après les informations contenues dans les différents rapports d’opération du réacteur.

Concernant le modèle thermohydraulique, plusieurs approximations sont faites : les écoulements de sel et de sodium liquide sont modélisés comme unidimensionnels et laminaires ; les couches de sodium au-dessus et en-dessous du cœur ne sont pas représentées ; les porosités du modérateur en oxyde de béryllium ne sont pas traitées mais remplacées par un jeu inter-assemblages ; le cœur n’est pas découpé par un cylindre, le réseau hexagonal est conservé et certains assemblages en périphérie complètement retirés ; le circuit secondaire et les échangeurs de chaleurs ne sont pas modélisés, des conditions d’entrée pour les champs de vitesse, température et concentration sont imposées ; les bords extérieurs du modérateur sont traités comme adiabatiques.

Le modèle neutronique également contient des approximations : devant les incertitudes concernant la densité du modérateur et les taux d’impuretés dans les tuyaux en inconel ainsi que dans le modérateur, deux jeux de données respectant la bonne masse critique de sel sont créés, et comparés sur la pesée des barres de commande. Un jeu de données avec une faible densité de modérateur et un faible taux d’impuretés est ainsi sélectionné. Les sections macroscopiques auto-protégées ne sont pas homogénéisées — à l’exception de l’inconel et de l’oxyde de béryllium autour du sel qui sont traités comme un seul matériau modérateur — et discrétisées sur 20 (simulations stationnaires) et 6 (transitoires) groupes, ainsi que 3 paramètres de température et 2 de concentration des barres. Dans la géométrie du cœur pour le calcul neutronique, les coudes de sel sont traités comme droits, et le réseau hexagonal est conservé (pas de coupe cylindrique), certains assemblages en périphérie étant traités comme du vide ; 8 groupes de précurseurs sont considérés ; la discrétisation angulaire considère 80 (simulations stationnaires) et 48 (transitoires) directions.

Une première simulation couplée stationnaire est réalisée, afin de reproduire l’état nominal de l’ARE. La puissance totale, ainsi que les débits, températures et concentrations en entrée sont imposés. Les températures moyennes et de sortie du sel et du sodium sont mesurées et comparées aux données expérimentales. On relève un sel simulé légèrement plus chaud (+0.3 %) et un sodium plus froid (-5 %), qui peuvent

s'expliquer par la modélisation simplifiée du sodium qui le fait sortir trop rapidement du cœur.

Une série de simulations couplées stationnaire est ensuite effectuée, afin de mesurer la variation du β_{eff} avec le débit de sel (expérience L-7). Les températures des milieux sont fixes, mais le débit de sel en entrée est modifié à chaque simulation, et la réactivité mesurée et comparée aux données expérimentales. Une légère sur-réactivité des simulations sur les débits intermédiaires peut s'expliquer par la modélisation unidimensionnelle de l'écoulement de sel qui cause un mouvement plus intense des précurseurs, mais cela n'explique pas la légère sous-réactivité simulée à débit nul.

Des expériences transitoires sont ensuite réalisées. La première (expérience H-8) consiste en une insertion progressive de réactivité par retrait de la barre de régulation (+400 pcm en 37.5 s). Si une première modélisation simplifiée (insertion instantanée de +400 pcm de réactivité) cause un transitoire beaucoup trop intense et rapide, une deuxième modélisation par dilution progressive de la barre fournit des résultats plus probants : la puissance maximale simulée est 2.5 % trop faible, et la puissance finale simulée 14 % trop forte — ce dernier écart pouvant s'expliquer par la température du sel en entrée maintenue fixe dans la simulation.

Une deuxième expérience transitoire de suivi de charge est modélisée (expérience H-14). La puissance extraite à l'échangeur est augmentée, ce qui diminue la température de sel en entrée — la simulation impose directement une diminution de la température du sel en entrée (-44 K en 1 min). Par les mécanismes de contre-réaction, la puissance et la température en sortie du sel augmentent avant de se stabiliser à la puissance extraite. La simulation s'est en revanche arrêtée avant convergence, pour des raisons encore inexplicables.

Les résultats, améliorables mais satisfaisants, de ces comparaisons calculs-mesures sur l'ARE contribuent à la validation du couplage APOLL03[®] – TrioCFD.

Le code APOLL03[®] – TrioCFD est ensuite utilisé pour modéliser le Molten Salt Fast Reactor (MSFR) en vue d'analyser les fluctuations turbulentes en son cœur.

La modélisation thermohydraulique du cœur du MSFR est particulièrement étudiée. Tout d'abord, des simulations RANS sont effectuées, sans couplage neutronique — la distribution de puissance dans le cœur est fixe. Différentes études de sensibilité sont réalisées : sensibilité à la géométrie retenue (cœur complet ou un secteur avec conditions de symétrie), à la modélisation de l'échangeur de chaleur, convergence en maillage, impact de l'ordre des schémas de discrétisations spatiaux, et impact du mod-

èle RANS utilisé ($k - \epsilon$ classique ou réalisable). Ces différentes études permettent de créer un maillage fin adapté à des simulations LES, ainsi qu'à définir un benchmark numérique qui permet de comparer les résultats fournis par TrioCFD à d'autres codes de CFD sur un modèle RANS d'un secteur du MSFR (benchmark développé et réalisé en collaboration avec des partenaires du CNRS, d'Orano, et de Framatome).

Des simulations LES sont ensuite réalisées (sans couplage neutronique). La comparaison entre les résultats obtenus sur le cœur complet et sur un secteur avec conditions de symétrie montre que ces dernières perturbent fortement la formation des tourbillons dans le cœur et faussent la simulation. Les champs moyens LES de vitesse et de température sont comparés aux champs RANS. Enfin, les fluctuations spatiales et temporelles du champ de température sont mesurées. Sans couplage, les fluctuations temporelles de la température au centre du cœur sont estimées à $\mp 3\%$.

Un modèle neutronique du cœur du MSFR est ensuite réalisé : trois matériaux sont considérés, le sel combustible, la couverture fertile radiale et les réflecteurs axiaux ; les sections macroscopiques auto-protégées sont discrétisées sur 6 groupes d'énergie, et un paramètre de température (sel combustible). Les échangeurs ne sont pas représentés dans la géométrie neutronique ; la discrétisation angulaire se fait sur 48 directions ; les précurseurs sont considérés immobiles afin d'accélérer grandement le temps de calcul neutronique. Un premier calcul stationnaire à température uniforme est réalisé, afin d'obtenir un flux et une distribution de puissance.

Un calcul couplé stationnaire est effectué. La puissance totale est fixée dans le calcul neutronique, seule la distribution de puissance peut varier, un léger décalage de la nappe vers le bas du cœur (où la température est plus froide) est observé. Le calcul thermohydraulique tourne sur un maillage dégradé pour gagner en temps de calcul, ce qui empêche une comparaison avec les champs issus du calcul LES. Un calcul transitoire couplé sans perturbation est lancé, mais les très longs temps de calcul empêchent l'obtention de résultats utilisables.

Une meilleure parallélisation du problème ainsi que l'utilisation de ressources HPC devraient permettre de calculer un transitoire couplé sur le cœur du MSFR. Afin de faciliter l'étude des fluctuations turbulentes sur un cas plus rapidement calculable, un "toy model" d'écoulement turbulent périodique dans un cylindre est également développé ; des simulations couplées sont en cours sur ce modèle.